© 2023. Published by The Company of Biologists Ltd | Journal of Cell Science (2023) 136, jcs261511. doi:10.1242/jcs.261511

RESEARCH ARTICLE

Structure and dynamics of the contractile vacuole complex in *Tetrahymena thermophila*

Chao-Yin Cheng[1], Daniel P. Romero[2], Martin Zoltner[3], Meng-Chao Yao[4] and Aaron P. Turkewitz[1,*]

ABSTRACT

The contractile vacuole complex (CVC) is a dynamic and morphologically complex membrane organelle, comprising a large vesicle (bladder) linked with a tubular reticulum (spongiome). CVCs provide key osmoregulatory roles across diverse eukaryotic lineages, but probing the mechanisms underlying their structure and function is hampered by the limited tools available for *in vivo* analysis. In the experimentally tractable ciliate *Tetrahymena thermophila*, we describe four proteins that, as endogenously tagged constructs, localize specifically to distinct CVC zones. The DOPEY homolog Dop1p and the CORVET subunit Vps8Dp localize both to the bladder and spongiome but with different local distributions that are sensitive to osmotic perturbation, whereas the lipid scramblase Scr7p colocalizes with Vps8Dp. The H^+-ATPase subunit Vma4 is spongiome specific. The live imaging permitted by these probes revealed dynamics at multiple scales including rapid exchange of CVC-localized and soluble protein pools versus lateral diffusion in the spongiome, spongiome extension and branching, and CVC formation during mitosis. Although the association with *DOP1* and *VPS8D* implicate the CVC in endosomal trafficking, both the bladder and spongiome might be isolated from bulk endocytic input.

KEY WORDS: *Tetrahymena*, Contractile vacuole complex, Organelle dynamics, Organelle biogenesis, Osmotic regulation

INTRODUCTION

Although essential for life, water also endangers any cell that cannot offset diffusional water uptake across its plasma membrane. Inward water diffusion occurs whenever the tonicity of the cell cytoplasm exceeds that of the extracellular fluid, and this can result in catastrophic swelling for cells that lack a rigid cell wall (Ritter et al., 2021). This challenge existed during the evolution of many unicellular protists adapting to fresh-water environments, and is today reflected in the phylogenetically widespread presence of osmoregulatory organelles called contractile vacuole (CV) complexes (CVCs) (Allen, 2000; Jimenez et al., 2022; Patterson, 1980). The CVC consists of one or more large vesicles, sometimes called cisternae or bladders (a name we will use), which are connected to membrane tubules that extend as a network (spongiome) into the cytoplasm (Allen and Naitoh, 2002). In current models, water absorbed into the spongiome from the cytoplasm fills the expanding CV, which subsequently contracts during the phase when its contents are expelled through a transient opening in the plasma membrane (Plattner, 2015). As befits an osmoregulatory organelle, the periodicity of the contractile cycle is sensitive to the extracellular tonicity (Allen, 2000; Docampo et al., 2013; Heuser et al., 1993; Gabriel et al., 1999).

CVCs were first recognized as prominent cellular features more than two centuries ago, but our current understanding of mechanisms underlying cyclic expansion and contraction is still fragmentary, including of the mechanics of contraction itself (Tani et al., 2001, 2000, 2002; Naitoh et al., 1997; Spallanzani, 1776). The most detailed molecular studies have been pursued in *Dictyostelium discoideum*, *Paramecium* (species *multimicronucleatum* and *tetraurelia*), and the trypanosomid *Trypanosoma cruzi*, which represent three highly unrelated lineages (Amoebozoa, Alveolata and Rhizaria, respectively). In all three, water transfer from the cytosol into the CVC lumen involves the activity of proton-pumping vacuolar (V-)ATPases in the organellar membrane (Fok et al., 1995; Gronlien et al., 2002; Temesvari et al., 1996). However, because the CVC lumen is not detectibly acidified (Stock et al., 2002a), it is believed that the proton gradients produced by these pumps are harnessed to produce coupled gradients of other ions, which are more directly involved in transport of water (Jimenez and Docampo, 2015) and other small molecules (Stock et al., 2001, 2002a,b; Heuser et al., 1993). Bladders can also undergo fusion with cytoplasmic organelles called acidocalcisomes that independently accumulate water-drawing ions (Rohloff et al., 2004; Marchesini et al., 2002; Montalvetti et al., 2004). However, the details are unclear and might differ between organisms, between which there are also notable morphological differences (Allen and Naitoh, 2002). For example, in trypanosomes, the bladder is localized by attachment via an electron-dense structure to the flagellar pocket, in which transient pores are posited to form during bladder emptying (Girard-Dias et al., 2012). A similar arrangement exists in *Paramecium*, except that the bladder localization is via linkage to stable plasma membrane pores via dedicated cytoskeletal connections (Allen and Naitoh, 2002). In contrast, in *Dictyostelium*, both the number and the position of bladders is variable, and their emptying appears to involve kiss-and-run fusion at contingent sites on the plasma membrane (Becker et al., 1999; Essid et al., 2012; Heuser, 2006).

Similarly, the anatomy of the tubular network surrounding the bladder, the spongiome, as well as the connections between the bladder and spongiome, display significant differences between these organisms (Allen and Naitoh, 2002). In *Dictyostelium*, both the bladder and spongiome are rich in V-ATPase, and the two structures might interconvert during contractile cycles (Gerisch et al., 2002). In *T. cruzi* the V-ATPase appears to be concentrated in the bladder (Ulrich et al., 2011), whereas the *Paramecium* V-ATPase is strictly concentrated in a subdomain of the spongiome,

[1]Department of Molecular Genetics and Cell Biology, University of Chicago, Chicago, IL 60637, USA. [2]Department of Pharmacology, University of Minnesota, Minneapolis, MN 55455, USA. [3]Biotechnology Biomedicine Centre of the Academy of Sciences, České Budějovice, 370 05, Czech Republic. [4]Institute of Molecular Biology, Academia Sinica, Taipei 115, Taiwan.

*Author for correspondence (apturkew@uchicago.edu)

C.-Y.C., 0000-0002-9530-524X; M.Z., 0000-0002-0214-285X; A.P.T., 0000-0003-3531-5806

Handling Editor: Jennifer Lippincott-Schwartz
Received 25 July 2023; Accepted 23 October 2023

Journal of Cell Science (2023) 136, jcs261511. doi:10.1242/jcs.261511

called 'decorated' (Fok et al., 1995). The *Paramecium* CVC, which altogether appears to be more highly structured than in *Dictyostelium* or trypanosomes, also includes a third distinct zone comprising undecorated tubular arms that link the bladder and decorated spongiome (Ishida et al., 1996; McKanna, 1976). The arms appear to become cyclically isolated from the bladder in a way that limits fluid backflow during contraction (Tominaga et al., 1998b; Gronlien et al., 2002; Tani et al., 2002). A similar dynamic arrangement has been described in Trypanosomatids (Linder and Staehelin, 1979).

CV-associated proteins have been identified in *Dictyostelium*, trypanosomes and *Paramecium*, but only a small subset of these appeared uniquely localized to the CVC (Plattner, 2013; Bush et al., 1994; Du et al., 2008; Manna et al., 2023; Plattner, 2015; Schonemann et al., 2013; Ulrich et al., 2011; Gerald et al., 2002; Gabriel et al., 1999). This subset has provided key tools both for live imaging of CVC dynamics in the form of fluorescently tagged transgenes, as well as for advancing informative candidates for functional studies (Becker et al., 1999; Du et al., 2008; Gabriel et al., 1999; Gerisch et al., 2002; Harris et al., 2001). In a prior study, we identified such a candidate in the ciliate *Tetrahymena thermophila*, as part of a survey of CORVET complexes in this organism (Sparvoli et al., 2020). *Tetrahymena*, like *Paramecium*, belongs to the Oligohymenophorean subgroup of ciliates, but the two genera diverged from one another hundreds of millions of years ago (Warren et al., 2017). VPS8D encodes one subunit of a hetero-hexameric CORVET complex whose homologs in other organisms are involved in vesicle fusion in the endolysosomal pathway (van der Beek et al., 2019). In *Tetrahymena*, one of six such complexes appeared to localize to the CVC (Sparvoli et al., 2020). Although the CVC in *Tetrahymena* species was historically the subject of both physiological and ultrastructural studies (Elliott and Bak, 1964), Vps8Dp (the protein product of the *VPS8D* gene), together with a small set of Rab GTPases (Bright et al., 2010), were the first potential protein markers specific to this compartment. Recently, other potential candidates were advanced in genetic studies that uncovered two genes, *DOP1* and *VMA4*, that were linked with CVC-related phenotypes (Cheng et al., 2016). *DOP1* belonged to the conserved DOPEY family, of which members in yeast and animals were associated with membrane trafficking (Moliere et al., 2022). *VMA4* encoded the E-subunit of a V-ATPase complex (Collins and Forgac, 2020).

In this manuscript, we provide evidence that Vps8Dp, Dop1p and Vma4p, together with a novel predicted lipid scramblase Scr7p, are bona fide CVC proteins in *T. thermophila*. Vps8D and Dop1p also have large dispersed cytoplasmic pools, which undergo exchange with the CVC-localized cohort. By exploiting fluorescently tagged copies of these proteins for live-cell imaging, we developed models for both the anatomy and the contractile cycle of the CVC in this organism. Cells expressing the tagged proteins also provided new insights into the response of the CVC to osmotic stress, and CVC duplication during cell division. Notably, although all four proteins localize to the CVC, they occupy different zones. Dop1p and Vps8Dp both localize to the bladder periphery, but Vps8D is shifted distally. This difference between localization of Vps8Dp and Dop1p becomes more pronounced under hypo-osmotic stress, supporting the idea that the proteins occupy two functionally distinct regions. In addition, Vps8Dp and Dop1p localize to the spongiome, likewise each displaying a distinct distribution. Instead, the two appear locally concentrated within distinct but overlapping zones. Scr7p localization coincides with that of Vps8Dp, whereas Vma4p is strictly localized to the spongiome but not the bladder.

RESULTS

Dop1p, a protein in the DOPEY family, localizes to the CVC bladder and spongiome

T. thermophila contains a prominent CVC, whose structure, based on past studies, consists of a central bladder that is bridged with the plasma membrane via pores, generally two in number. The bladder is surrounded by a tubulovesicular spongiome. This structure is shown in Fig. 1A. By standard light microscopy, only the bladder is visible, as a round structure in the cell posterior. The bladder goes through cycles of collapse and expansion on a time scale of tens of seconds (Fig. 1B, top row). As previously reported, cells lacking the *DOP1* gene instead develop an enormously enlarged bladder, which grows at least in part by undergoing fusion with other large vesicular structures, and only undergoes cyclic collapse on a time scale of minutes (Fig. 1B, bottom row; Cheng et al., 2016). To ask whether the protein product of *DOP1* is directly associated with the CV, we targeted the macronuclear *DOP1* locus to endogenously tag the Dop1p C-terminus with mNeon. (The micronuclear germline *DOP1* locus, which was not modified by our approach, is silent in vegetative cells; Cassidy-Hanley et al., 1997.) Cells expressing Dop1p–mNeon showed bright fluorescence in the cell posterior. In cross sectional views, the bright fluorescent signal was tightly localized to the periphery of the CV bladder, from which it extended both anteriorly and posteriorly as a stripe tracing the cell cortex (Fig. 1C). In cells that are rotated 90° around their long axis, relative to the perspective in Fig. 1C, the Dop1p signal is again most concentrated at the CV bladder and extends in an irregular reticulum that radiates in all directions (Fig. 1D). In near-tangential views, the fluorescent signal appeared as two (or sometimes three) rings whose diameters were smaller than that of the bladder, and whose positions suggested their potential association with the pores bridging to the plasma membrane through which the bladder empties (Fig. 1E). To investigate this further, we took advantage of the fact that bundles of microtubules are known to emanate from the pore junctional zone linking the bladder and plasma membranes (Gaertig et al., 1995; Frankel, 2000), and thus the structures can be stained using anti-α-tubulin antibodies. In cells where we visualized both Dop1p and α-tubulin, the rings formed by the two proteins were concentric but not significantly overlapping (Fig. 1F,G). These images suggest that the junctional pore membrane might have a different composition from the bladder, and that Dop1p localizes preferentially to the latter. In addition to this concentrated fluorescence at the bladder and surrounding spongiome, Dop1p puncta were also lightly dispersed throughout the cell cytoplasm. These puncta showed minor overlap with endocytosed FM4-64 and therefore appear primarily to be associated with non-endosomal compartments (Fig. S1).

The availability of Dop1p as a bright and relatively compartment-specific marker for the CVC offered a new addition to the cell biology reagents available for ciliates, and it allowed us to monitor aspects of the contractile cycle in live cells. In optical sections corresponding roughly to the midpoint of an expanded bladder, one sector of the circumference of the expanded bladder is apposed to the cell periphery. That sector appears to be relatively stable when the CV contracts, while the rest of the bladder apparently collapses down upon it. This results in a brightly fluorescent crescent, which in three dimensions would appear as a lens. That is, the replacement of a CV sphere by a lens can be most easily explained by directional collapse of the bladder so that the cortex-distal zone draws close to the cortex-proximal zone (Fig. 1H). This model suggests that the plasma membrane-adjacent zone of the bladder is selectively stabilized, which might involve the aforementioned microtubules that emanate from the CV–plasma membrane junctions (Fig. 1G).

Journal of Cell Science (2023) 136, jcs261511. doi:10.1242/jcs.261511

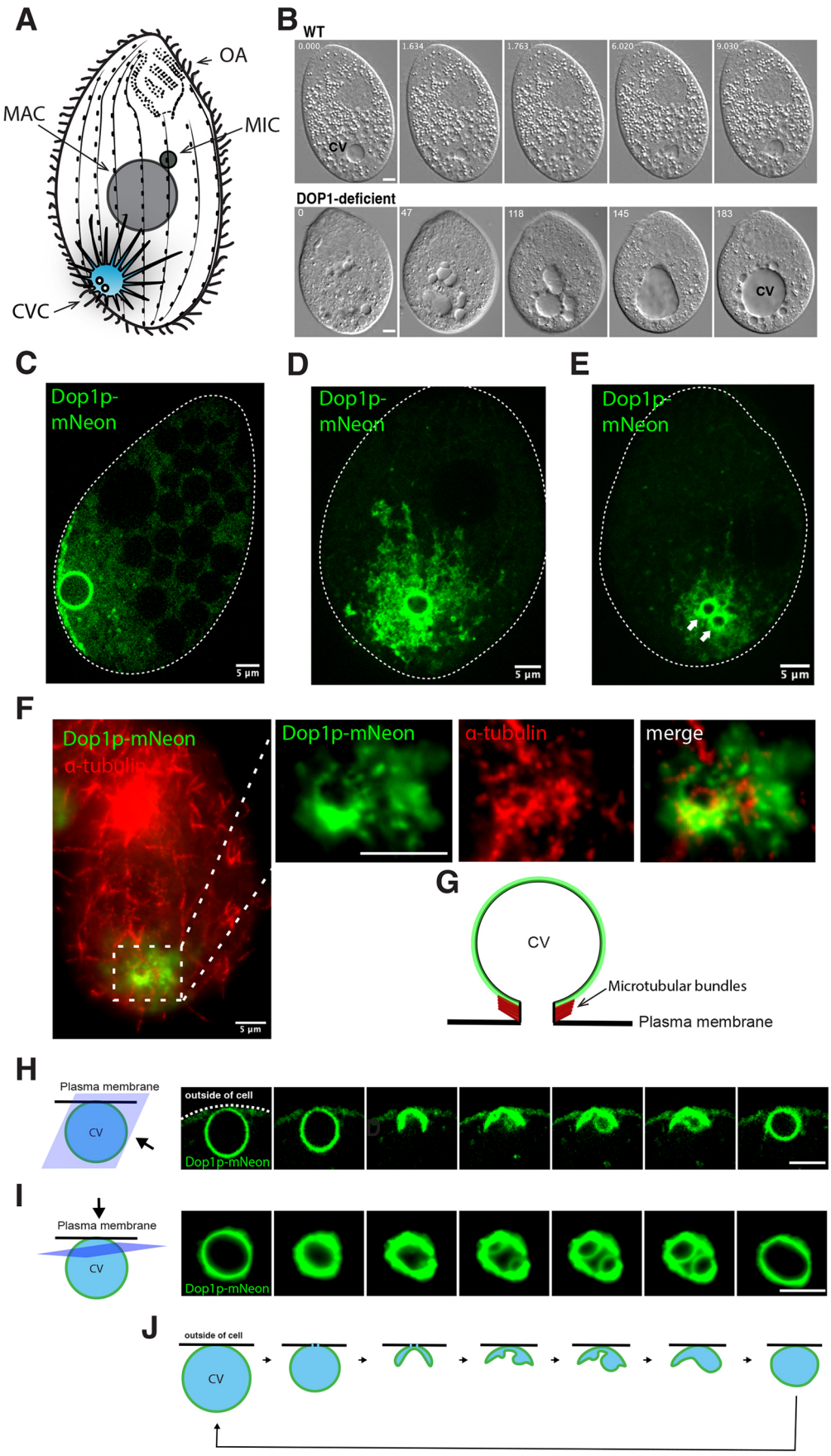

Fig. 1. See next page for legend.

Journal of Cell Science

Journal of Cell Science (2023) 136, jcs261511. doi:10.1242/jcs.261511

Fig. 1. Dop1p is a live-cell marker for the Tetrahymena CVC. (A) CVC anatomy in *Tetrahymena*. A cartoon showing previously established features of the *Tetrahymena* CVC including one central bladder near the cell posterior, the surrounding tubulo-vesicular network, and two pores connecting the bladder to the plasma membrane. Also shown are the oral apparatus (OA) in the anterior end of cell, and both the micronucleus (MIC) and macronucleus (MAC) near the cell middle. The vertical rows represent the cytoskeletal tracks called primary meridians, along which the ciliary basal bodies are spaced. For clarity, the cilia themselves are only shown at the cell edges. (B) As previously reported (Cheng et al., 2016), cells deficient in *DOP1* show pronounced changes in the structure and dynamics of the CV. Shown are five sequential differential interference contrast (DIC) images [individual frames for imaging are at *t*=0 s, 1.634 s, 1.763 s, 6.02 s and 9.03 s for wild-type (WT) images and for *t*=0 s, 47 s, 118 s, 145 s and 183 s for DOP1-deficient cells as labeled in left-upper comers in the images from video footage of WT and DOP1-deficient cells], demonstrating profound differences in the appearance and cycling time of the CV bladder in the mutant cells. Whereas the WT cell CV bladder shown goes through a contractile cycle in ∼10 s, the mutant cell CV bladder did not undergo a contraction over the 3 min interval shown but instead continued to expand. (C–E) Expression of Dop1p endogenously tagged with mNeon. Cells from proliferating cultures were immobilized for imaging using CyGEL, as described in the Materials and Methods. Videos were captured using a Marianas spinning disc confocal microscope with the fastest speed model. (C) The tagged protein localizes primarily at the bladder and along structures that extend from the bladder beneath the plasma membrane. Shown is one frame from a time-lapse video with 0.1 s frame intervals, focused near the cell mid-section (Movie 1). (D) Imaging of a cell, rotated along its long axis compared to that in C, so that the CVC is near the top surface of the cell. In this orientation, the structures underlying the plasma membrane are seen to constitute a reticular network. Shown is one frame from a time-lapse video with 0.51 s frame intervals (Movie 2). (E) Imaging of a cell oriented as in D, but with the focal plane very near the plasma membrane. In this tangential focal plane, Dop1p localizes to the circular area which might be related to the two pores (arrows). Shown is one frame from a time-lapse video with 0.51 s frame intervals (Movie 3). Dashed lines in C–E highlight the cell edge. (F) Imaging of a fixed cell expressing Dop1p–mNeon with immunofluorescent staining of α-tubulin, in a focal plane very near the cell surface. The area within the dotted white line, containing the two CV pores, is shown enlarged in the right panels with both the individual and the merged images. Dop1p is not colocalized with the microtubular bundles of the pores. Images were taken with a Zeiss Axio Observer 7 system. (G) Cartoon showing the known position of microtubules that emanate from the sides of the CV pore. (H) Live imaging of the CVC in a Dop1p–mNeon-expressing cell. The focal plane is roughly at the midpoint of the expanded bladder, viewed from the angle shown by the arrow. The seven images were extracted from a video capturing a contractile cycle (Movie 4). Cells from proliferating cultures were immobilized for imaging using CyGEL, as described in Materials and Methods. Videos were captured using a Marianas spinning disc confocal microscope with the fastest speed model. (I) Live imaging of the CVC in a Dop1p–mNeon-expressing cell. Here, the focal plane is tangential to the expanded bladder, close to the edge where it contacts the plasma membrane, as viewed from the angle shown by the arrow. The seven successive images were extracted from a video capturing a contractile cycle (Movie 5). Cells were immobilized by applying slight pressure to the cover slip (as described in the Materials and Methods) and imaged using a Zeiss Axio Observer 7 system with the fastest speed model to capture each frame among multiple exposures. (J) A model for the contractile cycle of the bladder. The model to illustrate the polarized collapse and refilling of the bladder is based on live images as exemplified in panels H and I. Images in this figure are representative of five experimental repeats. Scale bars: 5 µm.

The lens serves as a platform for the refilling of the bladder. As seen in cross section, refilling involves the emergence from the crescent of what appear as blebs, which subsequently expand (Fig. 1H).

The same cycle could also be viewed tangentially in living cells, in optical sections just below the surface that are roughly co-planar with the plasma membrane in the region of its junction with the CV (see cartoon in Fig. 1I). From this perspective, the ring corresponding to the bladder periphery fluctuates in fluorescence intensity over the contractile cycle but shows only minor fluctuations in size (Fig. 1I). These images are consistent with the idea that the crescent seen in the 3rd and 4th panels of Fig. 1H is a cross-section of a lens-shaped compartment that results from collapse of the originally spherical bladder (Fig. 1I). From the same tangential perspective, the blebbing seen in the orthogonal view (Fig. 1H, 4th panel) manifests as twin circles (Fig. 1I, 4th panel), suggesting that this phase of membrane expansion might be structured by the pores. A model for the contractile cycle of the bladder based on these complementary perspectives is shown in Fig. 1J.

Using Dop1p as a live marker allows visualization of CV duplication

During cell division, a subset of structures present in a cell must be duplicated and/or partitioned so that they are inherited by both daughters. In *T. thermophila* cell division (Fig. 2A), key features of the cell are duplicated along an anterior–posterior axis prior to cytokinesis (Cole and Gaertig, 2022). These include the CV pores, in which a new anterior pair appears at a stage when the micronucleus (MIC), but not macronucleus (MAC), has undergone mitosis. The pre-existing CV remains in the posterior while a second CV forms in the anterior and at the same relative position on the cell cortex (Ng, 1977; Ng and Frankel, 1977; Frankel, 1992, 2000).

We followed this process in cells expressing Dop1p–mNeon. In particular, because previous studies had focused exclusively on the pores themselves as prominent cortical landmarks in fixed cells, the availability of a CV marker allowed us to visualize other compartments and in live cells. At an early stage in the process when only the MIC had undergone mitosis, the Dop1p signal extended anteriorly from the maternal CV beyond the elongating cell midline, to two circular structures located at the cortical position that will be occupied by the newly forming CV (Fig. 2B). These circular structures might be related to the pores but their diameter (2–3 µm) is too large to correspond to mature pores. We favor the idea that the Dop1p-labeled structures instead reflect the beginning of bladder formation, an idea more consistent with the bladder localization data in Fig. 1G. To get better time resolution for when this bladder formation occurs, we simultaneously imaged bladder formation with either newly forming pores, using antibodies against acetyl-α-tubulin (Fig. 2C), or with the newly forming oral apparatus, using antibodies against centrin (Fig. 2D) (Jiang et al., 2020). Surveying a large number of dividing cells, we found that all cells showing newly forming bladders also had new pores (Fig. 2C; Fig. S2) and a fully developed new oral apparatus (Fig. 2D; Fig. S2).

Many of the Dop1p-labeled puncta and Vma4p-labeled reticulum seen in dividing cells are aligned along the cytoskeletal ‘ribs’, called meridians, that underlie the *Tetrahymena* cortex (Fig. 2B,C and Fig. S3) (Frankel, 2000). Interestingly, DOPEY family members in other organisms can recruit kinesin, a cytoskeletal-based motor protein (Mahajan et al., 2019). We therefore wondered whether *T. thermophila* Dop1p might associate with the cytoskeleton by a similar mechanism. A pilot immuno-isolation of epitope-tagged *DOP1*, expressed at the endogenous locus, was analyzed by liquid chromatography coupled to tandem mass spectrometry (LC-MS/MS) to identify potential interacting proteins. We detected two histidine triad motif (HIT)-domain-containing proteins, with corresponding peptide intensities and sequence coverage suggestive of stochiometric complex formation (Fig. S4A–D,

Journal of Cell Science (2023) 136, jcs261511. doi:10.1242/jcs.261511

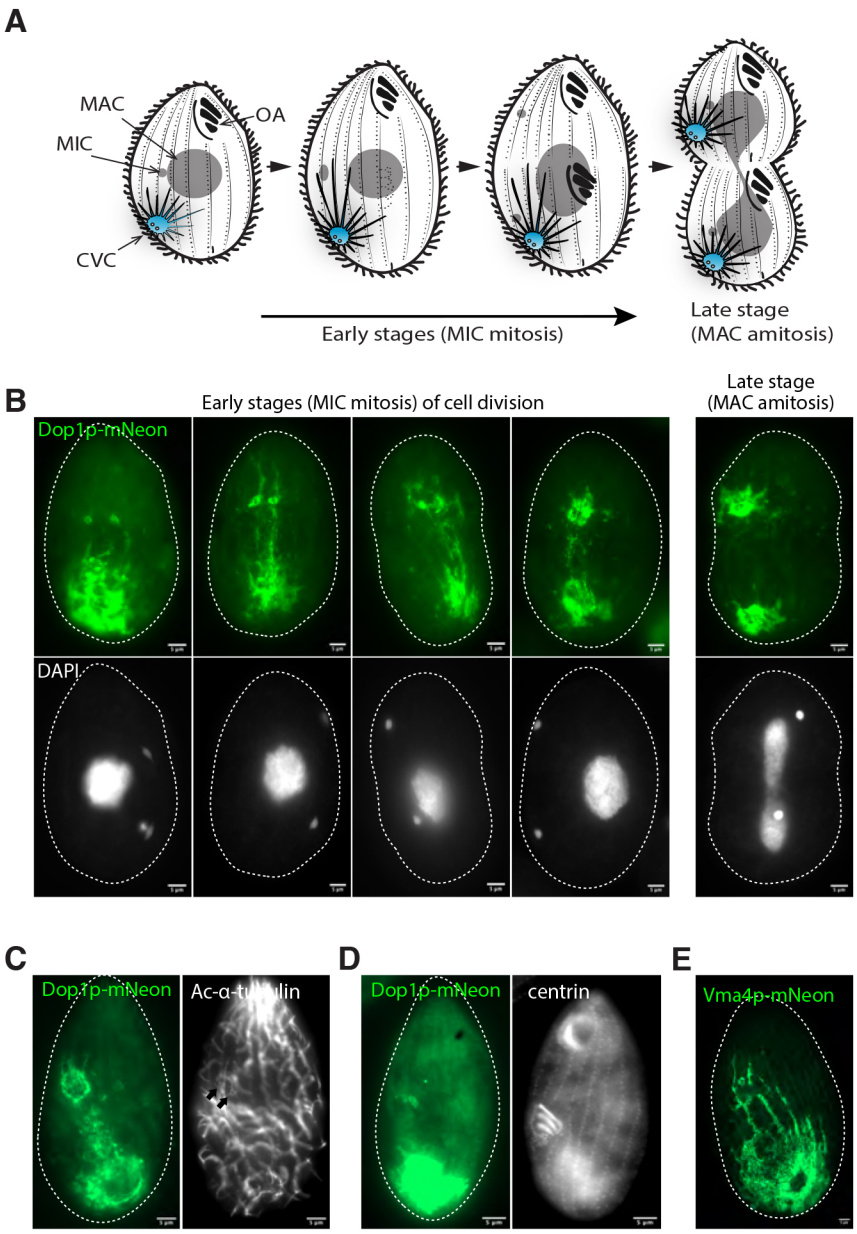

Fig. 2. Dop1p-based imaging of CVC duplication. (A) Cell division in *T. thermophila*. Micronuclear (MIC) mitotic division is followed by macronuclear (MAC) elongation and amitotic division. Unique cellular features, including the CVC and oral apparatus (OA), are generated as second copies in the anterior half of the elongating cell, which will become the daughter upon cytokinesis. (B) Imaging of the CVC in Dop1p–mNeon-expressing dividing cells, that were fixed and stained with DAPI. The first four images are of cells at early stages in cell division, as judged based on nuclear morphology, while the fifth image captures a later stage. The newly forming CVC in the anterior is first visible as two Dop1p-labeled circular structures that might represent incipient bladders. Dop1p also appears to be selectively concentrated along a subset of cytoskeletal meridians that extend from the parental to the new CVC. Proliferating cells were fixed and stained as described in Materials and Methods. Images were taken with a Zeiss Axio Observer 7. (C) Imaging of the new CVC in Dop1p–mNeon-expressing dividing cells with immunofluorescent staining of acetyl-K40-α-tubulin, in a focal plane very near the cell surface to show the two new CV pores (arrows). (D) Imaging of the new CVC in Dop1p–mNeon-expressing dividing cells with immunofluorescent staining of centrin, in a focal plane near the cell surface to show the cortical rows of basal bodies and the new oral apparatus. (E) Imaging of a fixed Vma4p–mNeon-expressing dividing cell. The newly forming CVC in the anterior appears connected to Vma4p-labeled tubules that extend from the parental CVC along a subset of cytoskeletal meridians. Proliferating cells were fixed as described in Materials and Methods. Images were taken with a Zeiss Axio Observer 7. Dashed lines highlight the cell edge. Images in this figure are representative of ten experimental repeats. Scale bars: 5 µm.

Tables S4, S5). HIT domain proteins are phosphatases with a broad substrate range and the two candidate interactors exhibit a domain composition consistent with a predicted role in scavenger mRNA decapping. A further potential interactor, a predicted polytopic transmembrane protein, was detected with much lower confidence. (Fig. S4A–D, Tables S4, S5). Based on a conserved domain search (NCBI), this membrane protein might contain a PHM7_cyt superfamily domain, which is a characteristic of ion transporters including osmosensitive and mechanosensitive ion channels (Wang et al., 2023). To ask whether this protein associates with Dop1p at the CV bladder, we endogenously tagged it with mNeon. At steady state, the tagged protein was not visible at the CVC but instead appeared localized to peripheral structures that are likely to be the Golgi, as well as heterogeneous mobile compartments deeper in the cytoplasm (Fig. S4E; Movie 17). Given this lack of localization to the CV, together with the lack of an obvious connection to RNA metabolism, we did not further pursue these pulldown-defined candidates.

Vps8Dp, a CORVET complex subunit, shows punctate localization to the CVC

CORVET is a widely conserved hetero-hexameric complex, characterized most extensively in yeast and animals, that facilitates vesicle-vesicle tethering and fusion in endosomal trafficking (Balderhaar and Ungermann, 2013). We previously established that *T. thermophila* expresses six distinct CORVET complexes, called A through F, and we found that the D complex was likely to associate with CVs by localizing its Vps8 subunit (Vps8Dp) (Sparvoli et al., 2020). To ask how Vps8Dp localization compared with that of Dop1p, we analyzed cells expressing *VPS8D* endogenously tagged with mNeon. Consistent with previous results, Vps8Dp–mNeon appeared to localize both around the CV bladder and to the spongiome (Fig. 3A,B), and like Dop1p, also revealed the twin connections between the bladder and plasma membrane pores (Fig. 3B, third panel). However, whereas in live-cell imaging the Dop1p fluorescent signal over the bladder and reticulum surfaces appeared relatively continuous, Vps8Dp labeling was distinctly

Journal of Cell Science (2023) 136, jcs261511. doi:10.1242/jcs.261511

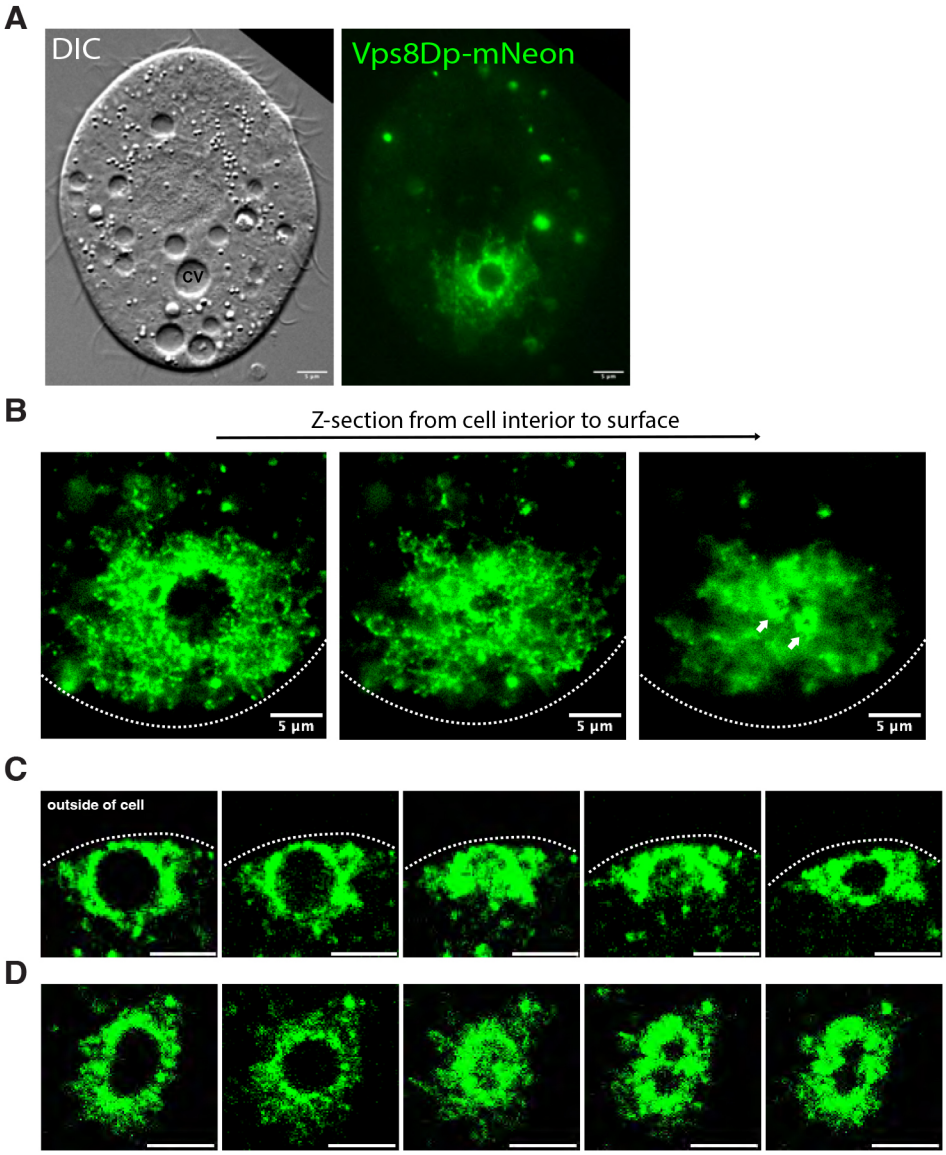

Fig. 3. Vps8Dp, a subunit of CORVET, shows punctate localization throughout the CVC. (A–D) Live imaging of the CVC in Vps8Dp–mNeon-expressing cells. (A) Left panel, differential interference contrast (DIC) image of *Tetrahymena*; the CV bladder is labeled. Right panel, corresponding fluorescent image. The frame shown is from a time-lapse video with 2.73 s frame interval (Movies 6A and 6B). (B) Successive sections in a *Z*-stack. The first section corresponds roughly to the midpoint of the expanded bladder, and second and third sections are progressively closer to the bladder periphery and cell surface, where two pores are outlined. The time-lapse video (0.15 s frame interval) from which these were taken is Movie 7. Both A and B were captured using a Axio Observer 7 system. (C) Cross-sectional view of contractile cycle (perspective equivalent to Fig. 1H). The video from which these five successive images were extracted is Movie 8. (D) Tangential view of contractile cycle (perspective equivalent to Fig. 1I). The video from which these five successive images were extracted is Movie 9. For both C and D, cells from proliferating cultures were immobilized using CyGEL and imaged using a Marianas spinning disc confocal microscope with the fastest speed model to capture each frame among multiple exposures. Dashed lines highlight the cell edge. Images in this figure are representative of ten experimental repeats. Scale bars: 5 µm.

punctate on all structures (Fig. 3B–D). In addition, heterogeneous puncta of Vps8Dp–mNeon were conspicuous throughout the cytoplasm.

As with cells expressing tagged Dop1p, the contractile cycle could be visualized in Vps8Dp–mNeon cells. Analysis of these videos confirmed that contraction is asymmetrical, with the bladder collapsing toward the plasma membrane (Fig. 3C). The images are consistent with the crescent/lens intermediate discussed above, but this structure appears less well-defined because although Dop1p tightly traces the contour of the bladder membrane, Vps8Dp puncta are irregularly distributed near the bladder membrane (Fig. 3B, middle panel). When the contractile cycle is viewed along the axis of the pores, and just beneath the plasma membrane, the bladder is deformed but without undergoing dramatic contraction, consistent with imaging in Dop1p–mNeon cells (Figs 3C,D and 1).

VMA4 localizes to the CVC reticulum but not to the bladder

Although the CV bladder and spongiome both contain Dop1p and Vps8Dp, these two compartments are likely to serve non-identical functions and therefore differ in their molecular composition. V-ATPases have been shown to localize to a spongiome in both the amoebozoan *Dictyostelium discoideum* and the ciliate *Paramecium tetraurelia* (Fok et al., 1995; Heuser et al., 1993; Fok et al., 1993; Nolta et al., 1993). In *T. thermophila*, the V-ATPase E-subunit-encoding gene, *VMA4*, is a potential CVC determinant (Cheng et al., 2016). To test this, we disrupted all macronuclear copies of *VMA4*. The resulting Δ*vma4* cells showed greatly slowed cycles of CV contraction (Fig. 4A). To ask whether Vma4p localizes to the CVC, we integrated the mNeon tag at the endogenous *VMA4* locus. The fluorescent signal was visible only at the CVC and exclusively within the spongiome. That is, unlike Vps8Dp or Dop1p, Vma4p was not concentrated at the bladder periphery (Fig. 4B,C). Imaging of the edges of the spongiome in live cells revealed that Vma4p-labeled tubules show dynamic extension, retraction and branching (Fig. 4D). The localization of Vma4p to the spongiome but not the bladder underscores the functional difference between those compartments.

The Vma4p–mNeon signal appeared to be evenly distributed along spongiome tubules, which is different to what is seen with either Vps8Dp or Dop1p. To ask whether the same tubules contain Vma4p, Dop1p and Vps8Dp, we expressed Vps8Dp–mCherry in pairwise combination with either Vma4p–mNeon or

Journal of Cell Science (2023) 136, jcs261511. doi:10.1242/jcs.261511

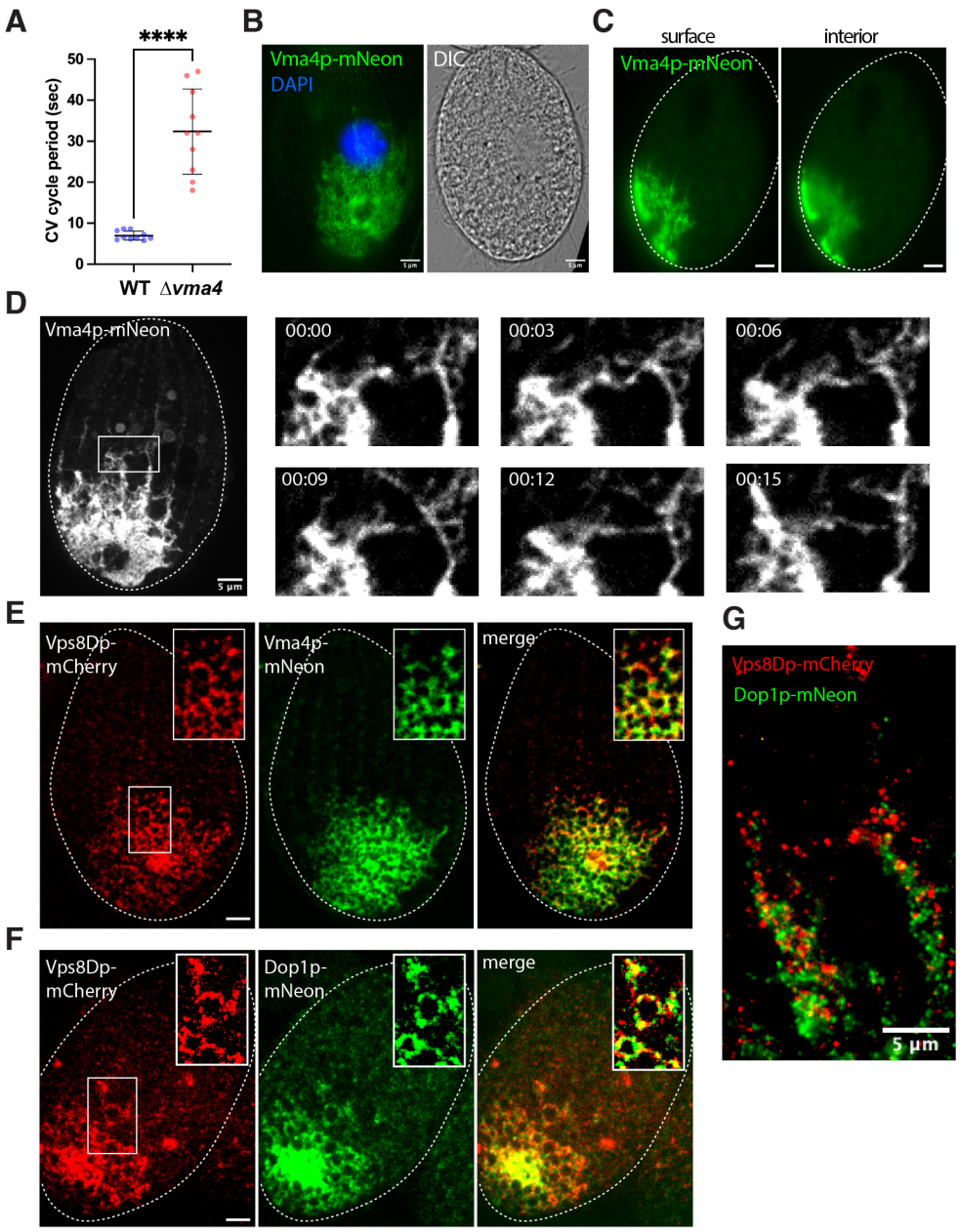

Fig. 4. Vma4p is a CVC protein that localizes exclusively to the tubules. (A) The period of the contractile cycle was measured for cells from proliferating cultures of wild-type (WT) or Δ*vma4* (complete knockout of *VMA4*) (n=10 for each culture). The mutant cells showed a ∼3-fold lengthening of the contractile cycle. The data were plotted using GraphPad Software Prism; individual data points and the mean±s.d. is shown. ****P<0.0001 (unpaired two-tailed t-test). (B) Vma4p localizes to the spongiome surrounding the bladder, but not the bladder itself. Proliferating cells expressing Vma4p–mNeon were fixed, and the nuclei stained with DAPI. A single cell is shown in the fluorescence (left) and DIC (right) channels. The Vma4p-labeled reticulum extends 10–20 µm from the bladder periphery. Images were taken with a Zeiss Axio Observer 7 system. (C) Vma4p-labeled tubules are concentrated near the plasma membrane, as shown in this side view of the CVC. The two panels are extracted from a Z-stack captured during live imaging (Movie 10), and show surface (left) and cell interior (right) sections. Images were taken with a Zeiss Axio Observer 7 system. (D) Vma4p-labeled tubules show dynamic extending and branching. Left panel, live imaging of Vma4p-labeled tubules. Right panels, magnified view of the boxed area in the left panel, showing six consecutive images (each individual image was selected with the 3 s interval, respectively labeled in left-upper corners in each image, extracted from a video (Movie 11). Images were taken using a Marianas spinning disc confocal microscope. (E) Analysis of cells expressing Vps8Dp–mCherry and Vma4p–mNeon. Vps8Dp (left panel) and Vma4p (center panel) show extensive overlap over the entire reticulum (right panel, merge). The two proteins might have different local distributions along tubules (magnified insert in the three panels). Proliferating cells co-expressing Vps8Dp–mCherry and Vma4p–mNeon were fixed at low temperature to optimize reticulum preservation (as described in the Materials and Methods). (F) Analysis of cells expressing Vps8Dp–mCherry and Dop1p–mNeon. Vps8Dp (left panel) and Dop1p (center panel) show extensive overlap over the bladder and reticulum (right panel, merge). The two proteins might have different local distributions (magnified insert in the three panels). Proliferating cells co-expressing Vps8Dp–mCherry and Dop1p–mNeon were fixed at low temperature to optimize reticulum preservation (as described in the Materials and Methods). Images of E and F were taken with a Marianas spinning disc confocal microscope. (G) Expansion microscopy analysis of cells expressing Vps8Dp–mCherry and Dop1p–mNeon. A merged image shows the two proteins have different local distribution along the tubules. Proliferating cells co-expressing Vps8Dp–mCherry and Dop1p–mNeon were fixed at low temperature to optimize reticulum preservation and processed to expand the cell ∼10-fold, as described in the Materials and Methods. Image was taken with a Zeiss Axio Observer 7 system. Dashed lines highlight the cell edge. Images in this figure are representative of ten experimental repeats. Scale bars: 5 µm.

Journal of Cell Science (2023) 136, jcs261511. doi:10.1242/jcs.261511

Dop1p–mNeon (Fig. 4E,F). In both cases, the images are consistent with the idea that all proteins are present and show overlapping distributions throughout the spongiome, but that there are local differences in their intensities (Fig. 4E,F), potentially reflecting membrane domains. These conclusions were consistent with expansion microscopy images of cells co-expressing Vps8Dp–mCherry and Dop1p–mNeon (Fig. 4G).

Proteins at the bladder periphery occupy subtly different zones

Given that distinct CVC proteins appear to be differentially distributed within the spongiome, we wondered whether the same might be true of the bladder membrane. To investigate this possibility, we asked whether Dop1p and Vps8Dp differed in their distributions at the bladder periphery. We co-expressed Dop1p–mNeon and Vps8Dp–mCherry from their endogenous loci, and then traced the intensity of each signal along a vector drawn outward from the center of the bladder (Fig. 5A). This analysis revealed that the peak of Dop1p was proximal to that of Vps8Dp (Fig. 5B,C). This could be explained if Dop1p is bound at the bladder membrane, whereas Vps8Dp is associated with a peripheral compartment. The Vps8Dp compartment appears to be less spatially restricted than the Dop1p compartment, given that the intensity profile of Dop1p showed a narrow peak relative to that of Vps8Dp (Fig. 5B). We did the same pairwise comparison between Vps8Dp and Vma4p, the latter shown above to be associated with the spongiome, and as expected we found that Vma4p in such radial plots is yet further spaced from the center (Fig. 5D–F).

Our results suggest that the bladder periphery can be conceived of as several concentric zones, for which Dop1p, Vps8Dp and Vma4p are markers that can be used to map the distributions of additional proteins. For example, we recently identified TTHERM_00999060, which we named *SCR7* (Scramblase 7; not published, D.P.R.), as a novel predicted lipid scramblase that localizes in part to the CVC (Fig. S5, Movies 19 and 20). When we co-expressed Scr7p–mNeon with Vps8D–mCherry, the two proteins showed near-complete colocalization (Fig. 5G,H; Fig. S5). Thus, Scr7p appears to localize to the same CVC zone as Vps8Dp. This finding also provides evidence that the distinct localizations seen for other pairs of proteins does not reflect a technical artifact (e.g. homophilic clustering induced by fluorescent protein tags).

Distinct compartments of the CVC respond differentially to osmotic stress

Many observations of ciliates by simple light microscopy have revealed that osmotic stressors result in morphological and dynamic changes to the CV bladder (Allen and Naitoh, 2002). The proteins we have identified in *Tetrahymena* allowed us to extend these observations in live cells by visualizing the spongiome, as well as distinguish the Vps8Dp- and Dop1p-defined zones of the bladder. We exposed the dual-labeled cells described above to mild osmotic stress for a brief period, as described in Materials and Methods, and then measured the same radial plots for the pairs of CV proteins. Interestingly, the distance between the peak intensities of Dop1p and Vps8Dp increased upon osmotic stress (Fig. 5I,J) whereas that between Vps8Dp and Vma4p decreased (Fig. 5K,L). The change in the distribution of Vma4p upon osmotic shock is driven primarily by a striking response to the osmotic stress, namely what appears to be the contraction or collapse of the spongiome (Fig. 5K, right panel). As a result of this contraction, Vma4p signal becomes much more heavily concentrated near the bladder periphery. A composite model including the distributions of Dop1p, Vps8Dp and Vma4p within the CVC is shown in Fig. 5M.

CVC-localized Vps8Dp and Dop1p exchange with large cytosolic pools

That the CVC is a highly dynamic structure is apparent both from its periodic contraction as well as the tubule extension and branching visualized above. Numerous Rabs and SNAREs localize to the CVC in ciliates, suggesting that the mechanisms underlying CVC dynamics involve active vesicle budding and fusion (Plattner, 2013, 2010; Bright et al., 2010; Turkewitz and Bright, 2011; Schonemann et al., 2013). Similarly, Vps8Dp, as part of CORVET, is likely to be directly involved in vesicle trafficking.

We asked whether Vps8Dp, together with other CVC proteins identified in this study, are dynamically associated with CVC membranes. We performed fluorescence recovery after photobleaching (FRAP) by briefly bleaching a defined sector of the CVC in immobilized cells and measuring the time of fluorescence recovery, which depends on exchange with fluorescent proteins from outside of the bleached area. A limitation of these experiments is that we although we could be certain of bleaching the entire CV this was not possible for the spongiome, given the expanse of the latter. These experiments were done using a confocal microscope, so the appearance of the fluorescent signals differs for some tagged proteins compared to the epifluorescence imaging shown in earlier figures.

Fig. 6A–F shows FRAP results for Dop1p and Vps8Dp, both of which are peripheral membrane proteins. The data reveal that both proteins dynamically exchange with pools in the non-bleached area, but that exchange of Vps8Dp appears more rapid than that of Dop1p (Fig. 6B,E; Fig. S6A–C). The extent of the recovery of each protein after bleaching might be limited by the relative sizes of the CV-associated versus non-CV pools. To gain some insight into this, we used these images to estimate the relative amounts of each protein pool at steady state that is localized to the CV versus non-CV area, subject to the limitation regarding defining the precise spongiome borders. This analysis suggests that both Dop1p and Vps8D include significant pools of cytosolic protein, but that this fraction is higher for Vps8Dp (Fig. 6C,F; Fig. S6D–F).

To ask more directly whether the cytosolic pool of Vps8Dp exchanges with the CVC pool, we used fluorescence loss in photobleaching (FLIP). We repeatedly bleached the CVC of immobilized cells expressing Vps8Dp–mNeon over a period of minutes, while monitoring the Vps8Dp–mNeon fluorescence at a distant site in the cell anterior (Fig. 6G). The results are consistent with exchange between cytoplasmic and CV-localized pools, given that Vps8D fluorescence in the cell anterior decreases upon bleaching of the CV pool (Fig. 6H,I).

Vma4p and Dop1p undergo exchange via different mechanisms

Vma4p, unlike Dop1p and Vps8Dp, is a subunit of an integral membrane protein complex. In addition, unlike Dop1p and Vps8Dp, the entire pool of detectible Vma4p is localized to the CVC. We used FRAP to ask whether Vma4p is mobile within the spongiome membrane (Fig. 7A,B; Fig. S6G,H). After bleaching a subsection of the spongiome, we observed that Vma4p–mNeon fluorescence initially begins to recover at one edge and then progressively spreads (Fig. 7C). This is consistent with the idea that Vma4p is mobile within the plane of the membrane, and that

Journal of Cell Science (2023) 136, jcs261511. doi:10.1242/jcs.261511

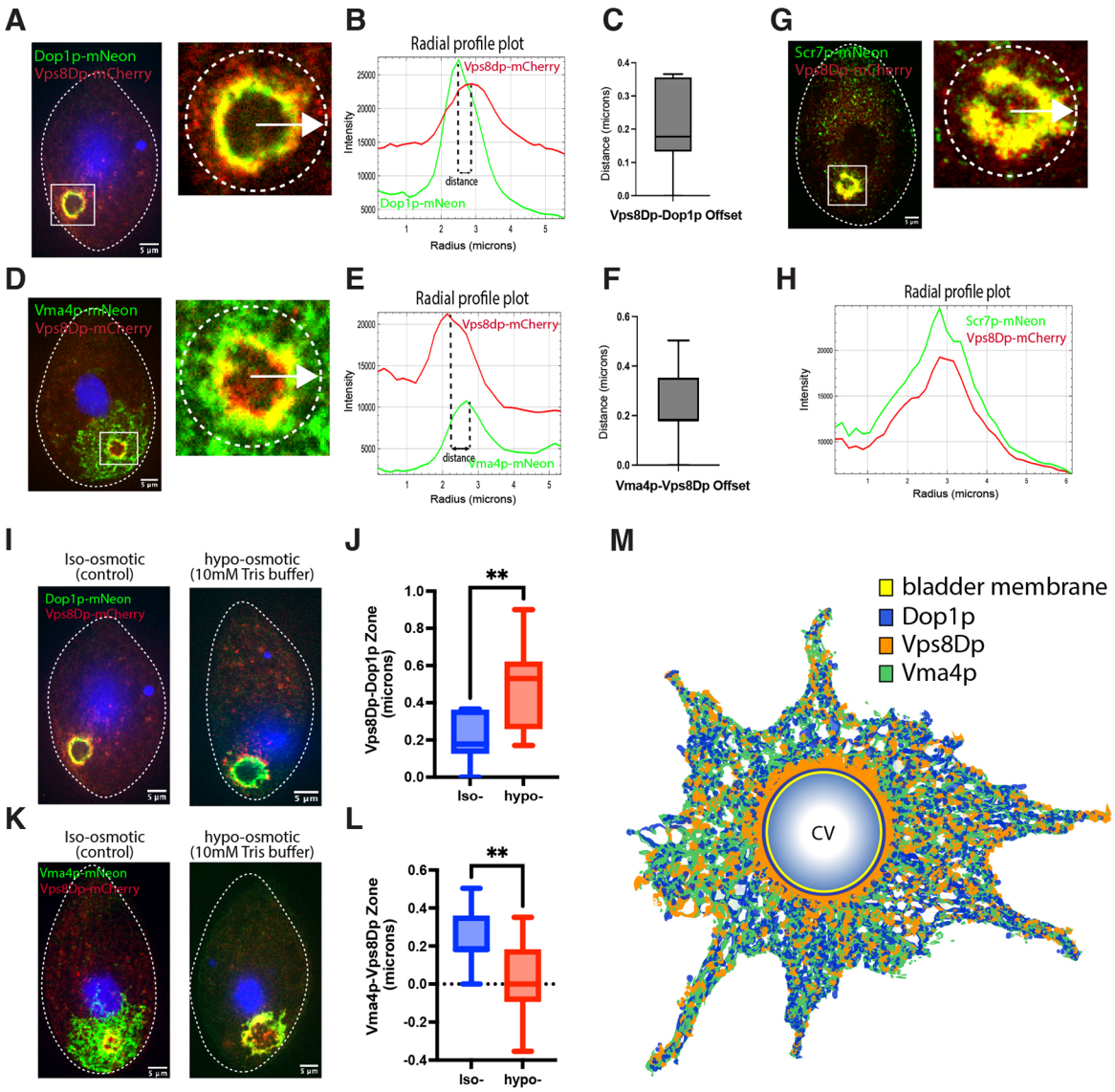

Fig. 5. Finer mapping reveals distinct protein distributions at the bladder periphery and these distributions are sensitive to osmotic challenge. (A–C) Vps8D is radially shifted with respect to Dop1p at the CV periphery. (A) Left panel, proliferating cell co-expressing Dop1p–mNeon and Vps8Dp–mCherry. The boxed area, which includes the CV bladder, is enlarged in the right panel. The fluorescent intensity profiles of the two fluorophores along the radial arrow shown were determined using the FIJI image Radial Profile plugin. Images were taken with a Marianas spinning disc confocal microscope. (B) The peak intensity of Vps8Dp is distal to that of Dop1p. The fluorescent intensity of Dop1–mNeon and Vps8Dp–mCherry was plotted along the vector in A, drawn outward from the center of the CV bladder to the periphery. The distance between the peaks of Dop1p and Vps8Dp signals is shown. (C) The zone distance between Vps8Dp and Dop1p. Fourteen additional images were analyzed as in A and B. The combined data were plotted as a box-and-whiskers plot by GraphPad Software Prism (the boxes display median and interquartile range, and the whiskers represent the minimum to maximum data values). (D–F) Vma4p is radially shifted with respect to Vps8D at the CV periphery. Left panel, proliferating cell co-expressing Vma4p–mNeon and Vps8Dp–mCherry. (E) The peak intensity of Vma4p is distal to that of Vps8Dp. (F) The zone distance between Vma4p and Vps8Dp. The experimental procedures and analytical methods used in D–F are identical to those used in A–C, respectively. (G,H) Scr7p colocalizes with Vps8Dp at the CV periphery. (G) Left panel, proliferating cell co-expressing Scr7p–mNeon and Vps8Dp–mCherry. Right panel, magnified image of boxed area containing the CV bladder. (H) Scr7p and Vps8Dp show similar intensity profiles along a radial vector. The experimental procedures and analytical methods used in G and H are identical to those used in A and B, respectively. (I) Proliferating cells expressing Dop1p–mNeon and Vps8Dp–mCherry were kept in culture medium (left panel) or incubated for 10 min in 10 mM Tris buffer (hypo-osmotic, right panel), as described in the Materials and Methods. Fixed and DAPI-stained cells were imaged with a Marianas spinning disc confocal microscope. (J) The zone distance between Dop1p and Vps8dp increases under hypo-osmotic challenge. Fourteen images from control cells and 13 images from the hypo-osmotic sample were used to measure the zone distance between Dop1p and Vps8Dp. The data are shown as a box-and-whiskers plot with median and interquartile range, and the whiskers representing the minimum to maximum value of data. $^{**}P<0.01$ for the increase in the spacing of the Vps8Dp and Dop1p peaks upon hypo-osmotic treatment (unpaired two-tailed *t*-test). (K) Cells expressing Vma4p–mNeon and Vps8Dp–mCherry. The experimental procedures and analytical methods are identical to those in I. (L) The zone distance between Vma4p and Vps8Dp decreases under hypo-osmotic challenge. Fourteen images from control cells and nine images from the hypo-osmotic sample were used to measure the zone distance between Vma4p and Vps8Dp. The plotting methods and statistical analysis are identical to those in J. $^{**}P<0.01$ for the decrease in the spacing of the Vma4p and Vps8Dp peaks upon hypo-osmotic treatment (unpaired two-tailed *t*-test). (M) A model for the distribution of Dop1p, Vps8Dp and Vma4p in the CVC. Dop1p associates tightly with the bladder membrane. Vps8Dp associates with a broader zone, and is more distal. Vma4p primarily localizes in the spongiome and partially overlaps with Dop1p and Vps8Dp. All three proteins localize throughout the spongiome, but might have non-identical distributions. Dashed lines highlight the cell edge, except in the right sides of panels A, D and G where the dashed lines highlight the CVC. Scale bars: 5 µm.

Journal of Cell Science (2023) 136, jcs261511. doi:10.1242/jcs.261511

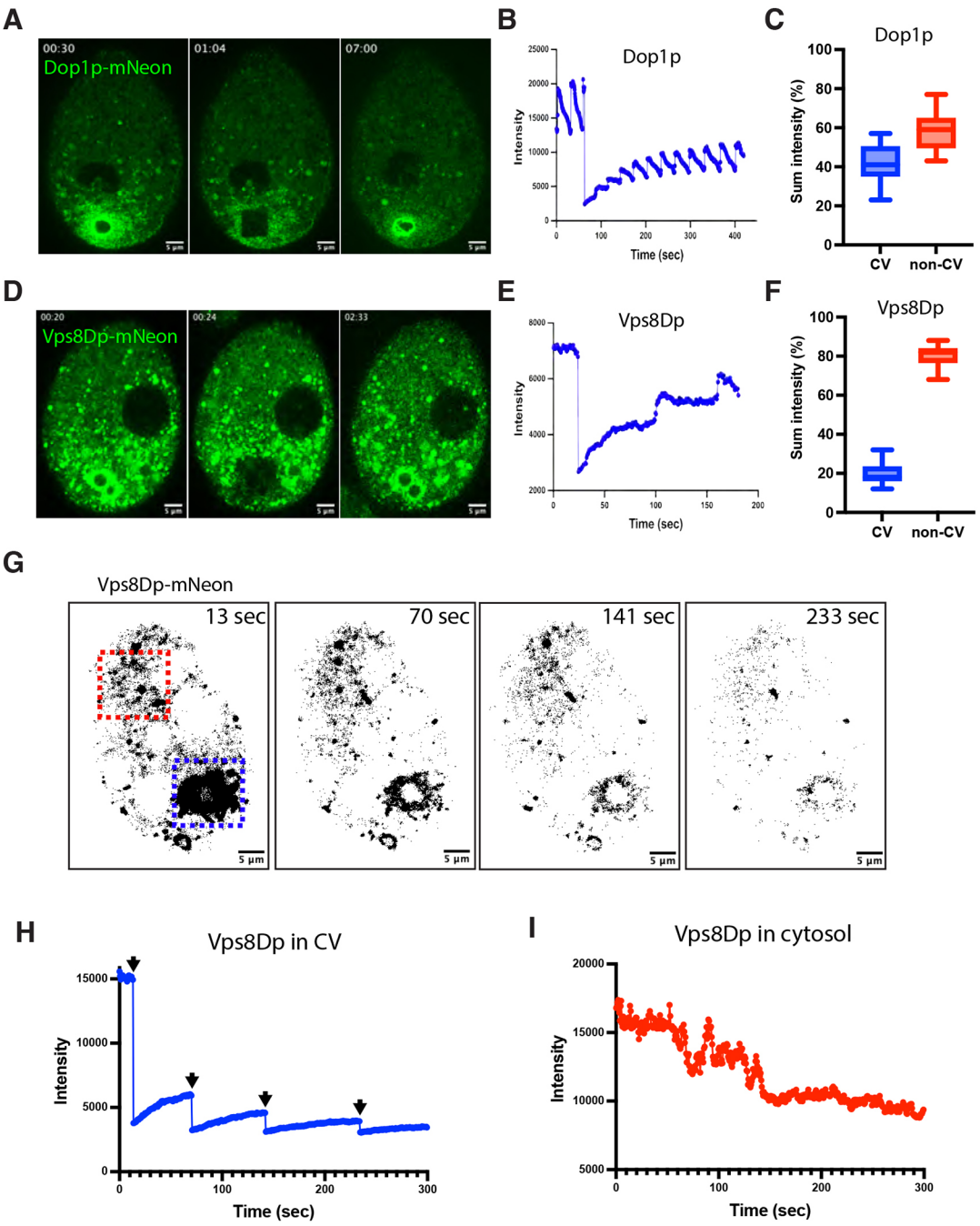

Fig. 6. CV-localized Dop1p and Vps8Dp differentially exchange with large cytoplasmic pools. (A) Cell expressing Dop1p–mNeon analyzed by FRAP. Proliferating cells were immobilized and live imaged with a Marianas spinning disc confocal microscope with a FRAP tool. Three images were extracted from a video (Movie 12) showing a photobleaching event and recovery. Left panel, cell before photobleaching at 30 s. Middle panel, cell immediately after photobleaching a region containing the CV and periphery at *t*=1:04. The bleached area appears as a dark square. Right panel, cell at *t*=7:00. (B) The recovery after photobleaching data were analyzed by FIJI image process software (see details in the Materials and Methods). The fluorescence intensity in the photobleached area was plotted using GraphPad Software Prism. The spikiness of the trace is due to periodic contraction of the CV. (C) The percentage of Dop1p in the CV and non-CV areas. The borders of the areas for quantification in 17 independent images (Fig. S8A) were determined by using FIJI software and the sum intensities of the designated areas were measured, as described in the Materials and Methods. The combined data were plotted as a box-and-whiskers plot by GraphPad Software Prism (the boxes display median and interquartile range, and the whiskers represent the minimum to maximum data values). (D) Cell expressing Vps8Dp–mNeon analyzed by FRAP. Three images were extracted from a video (Movie 13) showing a photobleaching event and recovery, with panels as in Fig. 8A but with the bleaching event at *t*=0.24 and recovery at *t*=2:33. (E) Recovery after photobleaching. (F) The percentage of Vps8Dp in the CV versus non-CV areas. Images and data are shown in Fig. S8B and Table S3. The experimental procedures and analytical methods used in D–F are identical to those used in A–C, respectively. (G) Cell expressing Vps8Dp–mNeon analyzed by FLIP. Four images were extracted from a video (Movie 14) in which the CV (bottom right, dotted blue square) was bleached four times successively at *t*=13 s, 70 s, 141 s and 233 s. The fluorescence intensity was measured both in the dotted blue square and in an anterior zone of the cytoplasm (dotted red square). The fluorescence intensities in both zones were analyzed by FIJI image process software. (H) The fluorescent signal of CV-localized Vps8Dp–mNeon (in the dotted blue square) decreased and recovered repeatedly after bleaching. Arrows indicate the four photobleaching events. (I) The anterior cytoplasmic Vps8dp–mNeon signal (in the red dotted square) decreased after photobleaching the CV. Images in G–I are representative of three experimental repeats. Scale bars: 5 µm.

Journal of Cell Science (2023) 136, jcs261511. doi:10.1242/jcs.261511

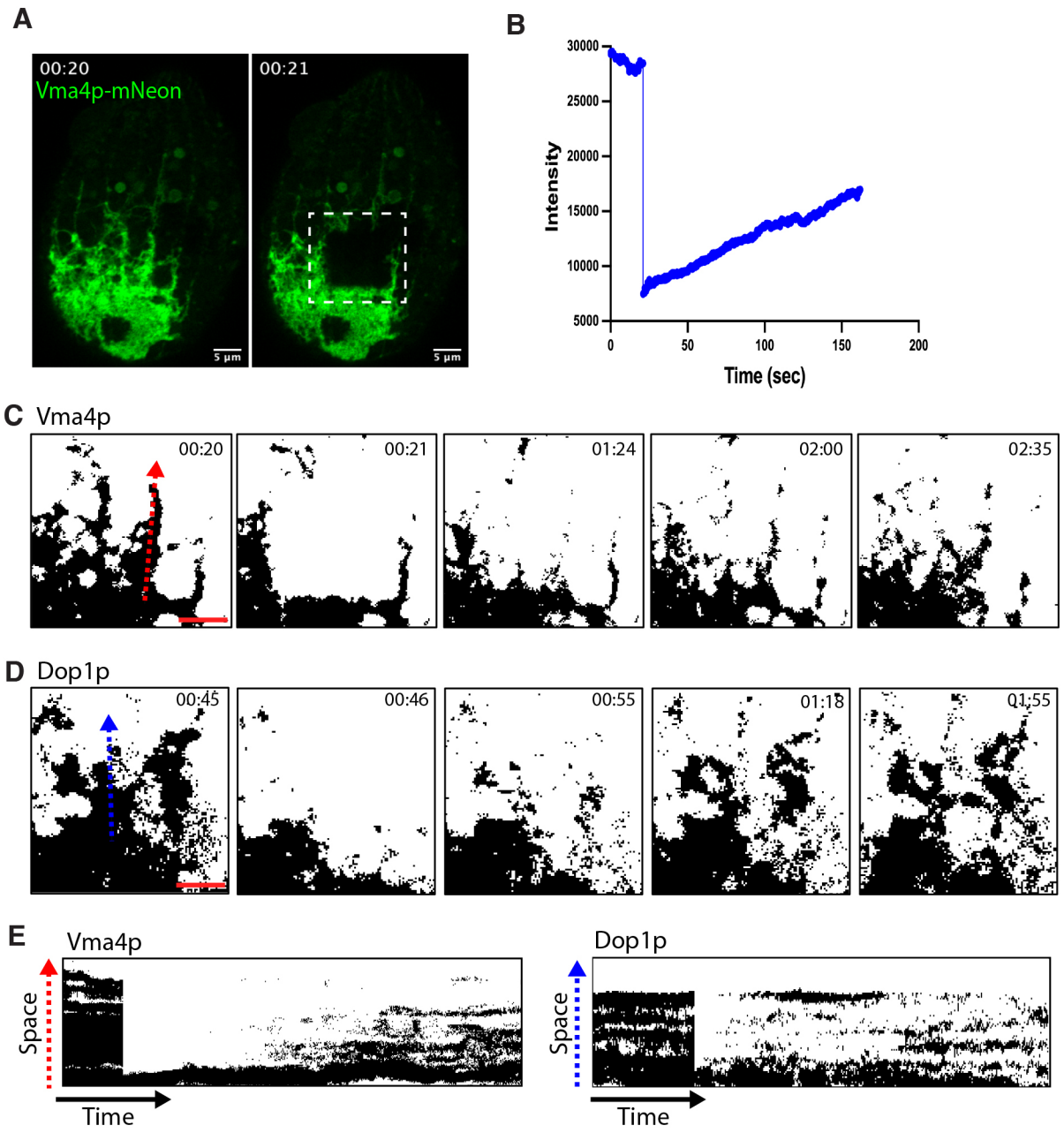

Fig. 7. Vma4p and Dop1p exchange via different mechanisms. (A) Cell expressing Vma4p–mNeon analyzed by FRAP. Two images were extracted from a video (Movie 15) to demonstrate a FRAP experiment in which a sector of the reticulum was bleached. Left panel, cell before photobleaching at *t*=20 s. Right panel, bleaching event at *t*=21 s, resulting in a dark square. Proliferating cells were immobilized and live imaged with a Marianas spinning disc confocal microscope with FRAP tool. The data were analyzed by FIJI image process software. (B) Recovery after photobleaching. The fluorescent intensity in the indicated area before and after photobleaching was plotted using GraphPad Software Prism. (C–E) Vma4p recovery after photobleaching includes diffusion within the tubule membranes, whereas Dop1p exchanges with a soluble pool. (C) Magnified image of region indicated in A right panel. Five images were extracted from a video (Movie 15) to illustrate that the recovery of Vma4p–mNeon fluorescence is directional and proceeds from the bottom of the field. This is also shown in the kymograph (E), based on tracking signal intensity and time along the red arrow shown in C. To illustrate the recovery process of Dop1p in the tubules, five images (D) and a kymograph (E) from CVC tubule-localized Dop1p FRAP video footage (Fig. S6A and Movie 16) are shown. The red and blue dotted arrows indicate the space (10 µm total) over which intensities were measured over time, as denoted in C and D, for kymograph analysis by FIJI image process software. Images in this figure are representative of three experimental repeats. Scale bars: 5 µm.

exchange is primarily due to diffusion along the tubules. In contrast, when the same analysis was performed on cells expressing Dop1p–mNeon, the fluorescence recovery was not directional but instead occurred in patches throughout the bleached area (Fig. 7D). This result is consistent with the idea that Dop1p exchange occurs via a cytosolic pool, which could be either soluble or vesicle associated. This difference between the spatial patterns of fluorescence recovery of Vma4p and Dop1p could also be seen in kymographs plotting the recovery of fluorescence (Fig. 7E).

The CVC is not labeled by the endocytic tracer FM4-64

Organelles in the endomembrane network are maintained by a balance of inward and outward membrane traffic. The relevant trafficking pathways for the CVC are poorly understood in any

Journal of Cell Science (2023) 136, jcs261511. doi:10.1242/jcs.261511

organism. Recent analysis in *Dictyostelium* points to the involvement of endosomal fusion machinery, although the specific roles are as yet unexplored (Manna et al., 2023). Similarly, an important role for endosomal trafficking to the ciliate CVC is consistent with the markers we have established above, given that CORVET in other organisms functions as an endosomal or endolysosomal tether–fusion complex, and the DOPEY family proteins are similarly endosome associated. Both V-ATPases and lipid scramblases function in many compartments, including endosomes (Marshansky and Futai, 2008; Hankins et al., 2015).

In *Tetrahymena*, as in many other cells, fluorescent styryl dyes can intercalate into the outer leaflet of the plasma membrane and be taken up into endocytic vesicles. Such dyes can therefore be used to trace endocytic trafficking (Betz and Bewick, 1992; Betz et al., 1996; Elde et al., 2005). One would also expect that FM dye in the cell medium could diffuse into the CV through the open pore during bladder emptying, and this has been documented in *Dictyostelium* (Nishihara et al., 2007). We confirmed those results, detecting clear CVC labeling after a 5 min incubation of *Dictyostelium* with red fluorescent FM4-64 (Fig. S7A). We then similarly incubated *Tetrahymena*, expressing tagged CVC markers, with FM4-64, and then looked for overlap between the FM dye and either Dop1p (Fig. 8A) or Vma4p (Fig. 8B). Strikingly, although a large range of cytoplasmic vesicles were labeled, there was no detectible overlap with the CVC markers after either 15 or 30 min of FM update, with the same result obtained after an overnight incubation (Fig. S7B, Movies 18A,B). Thus, the CVC in *Tetrahymena* appears to be isolated from bulk endocytic traffic, and in addition, some barrier appears to exist to free diffusion through the pore. Our data could also be explained if an unusual lipid composition in the luminal leaflet of the CVC bilayer resists intercalation of FM dyes.

DISCUSSION

Although the CV has been recognized by biologists for more than three centuries, the structure, and particularly the mechanisms underlying periodic contraction, are still incompletely understood. This lack of knowledge is partly attributable to the fact that although CVs are widely distributed among eukaryotes, they are not present in fungi, animals or plants, where most cell biology has been pursued. A corollary hurdle is that many of the organisms that do bear CVs have been inaccessible to many genetic and molecular approaches that are crucial for the analysis of such complex cell biological structures. CVs are prominent in both marine and fresh-water ciliates, and experiments and observations in *Paramecium* spp. have been important in generating our current understanding of the CV (McKanna, 1976; Kitching, 1939). Among the ciliates, the species with the best developed toolbox is *T. thermophila* (Ruehle et al., 2016). In this article, we establish a set of live markers for the CV in this organism. Whereas some CV-associated proteins have previously been identified in both *Tetrahymena* and *Paramecium*, the uniqueness of the localization has rarely been established, and/or other limitations precluded their use as live markers. We previously reported a set of Rab GTPases which, as over-expressed GFP-tagged proteins, appeared to be highly concentrated at the CV (Bright et al., 2010). However, these tagged proteins might not be readily visible when expressed at endogenous levels, a problem we have encountered with many Rabs in this organism (A.P.T., unpublished observations).

As shown in this manuscript, four proteins, two of which are peripherally associated with the membrane and two of which are membrane embedded or subunits of integral membrane complexes, could be tagged and used to visualize CVC dynamics when expressed at endogenous levels. These results significantly expand our ability to analyze the CVC in ciliates. Although the bladder could already be visualized even in the 18th century by light microscopy, our ability to capture videos of fluorescent bladders has revealed new details of the contractile cycle. The observation that Dop1p localized to a subtly different position at the bladder periphery compared to Vps8Dp and Scr7p, and that these zones show differential responses to osmotic challenge, should allow the mapping of subdomains in this complex organelle. In *Paramecium*, where the CVC is morphologically more complex than in *Tetrahymena*, there is a notable substructure within the spongiome where distal versus peripheral tubules show differential occupancy by V-ATPase as well as an aquaporin (Ishida et al., 2021).

Fluorescently tagged proteins that label the CVC structures also permitted us to recognize novel features of CVC duplication in mitotic cells, including the discovery that newly forming Dop1p-labeled bladders appear as two rings intermediate in size between pores and mature bladders. Previous studies of CVC duplication have relied on the pores, visible using silver staining, which appeared in relatively late stages of cell division (Frankel, 1992, 2000; Cole and Gaertig, 2022). We found that all dividing cells showing newly forming bladders also have new CV pores and a fully developed new oral apparatus. The identification of CVC-specific genes and proteins now presents opportunities for exploring developmental regulation, extending recent studies on cortical determinants for position-specific organelle biogenesis in ciliates. These studies have highlighted the crucial role of conserved signaling proteins in defining cortical pattern formation during cell division (Jiang et al., 2017, 2019a,b, 2020). One open question is whether CVC-specific proteins interact with the newly identified morphogens to influence the positioning and assembly of the new CVC. The precise positioning of new CV pores has been proposed to be regulated by their positioning relative to other organelles, rather than being fixed to a specific cortical pattern (Ng, 1977; Ng and Frankel, 1977). Intriguingly, we found that tubules labeled with Dop1p puncta as well as Vma4p, extend along meridians during cell division and potentially establish a connection between the pre-existing and new CVCs, so that the latter might derive in part from the former either informationally and/or compositionally.

The mechanisms underlying bladder contraction are still under investigation (Velle et al., 2023). CV bladders that were micro-surgically excised from *Paramecium* briefly continue to undergo periodic contraction, suggesting that remodeling might not depend on an organized cytoskeleton (Tominaga et al., 1998a; Tani et al., 2000, 2002). Ultrastructural studies have revealed what could be an unusual packing of CV membranes during contraction, with possible similarity to lipid cubic phases (McKanna, 1976; Tominaga et al., 1999; Allen, 2000). A distinct lipid composition of the *Paramecium* bladder has been proposed to directly drive contractile cycles in a model that could involve flipping across the membrane bilayer (Tani et al., 2002), but as yet this model is untested. Our finding that the predicted lipid scramblase Scr7p is strongly concentrated at the CVC corroborates that lipid transfer plays a role in this organelle, which we hope to elucidate in the future. We found that Scr7p closely colocalizes with Vps8Dp, distal to the localization of Dop1p at the bladder periphery, but higher resolution imaging will be needed to understand precisely what structures are involved.

The homologs of *DOP1* and *VPS8D* in other organisms are endosomal proteins (Balderhaar and Ungermann, 2013; Moliere

Journal of Cell Science (2023) 136, jcs261511. doi:10.1242/jcs.261511

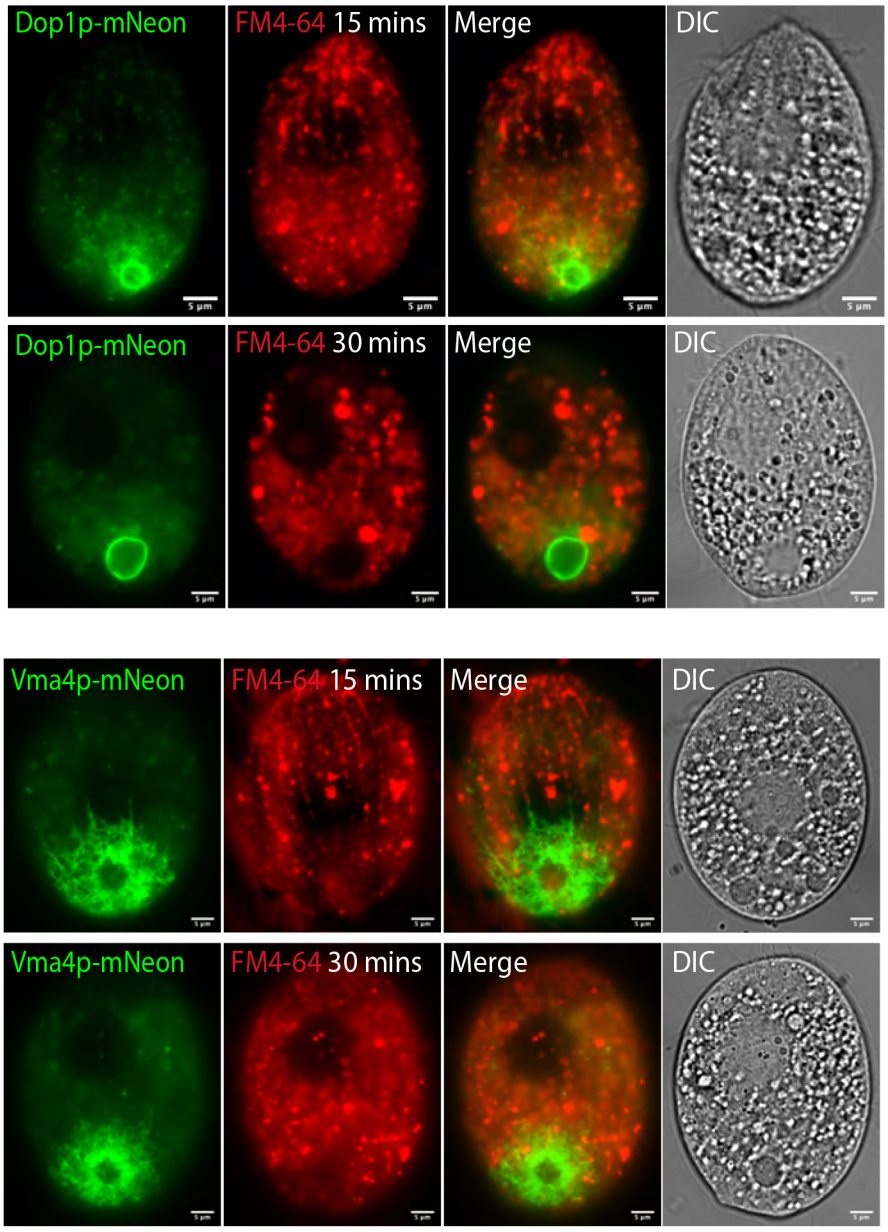

Fig. 8. The CVC is not labeled by an endocytic tracer. (A) Cells expressing Dop1p–mNeon were incubated with the red fluorescent endocytic tracer FM4-64 for 15 min (top panel) or 30 min (bottom panel). (B) Cells expressing Vma4p–mNeon were incubated with FM4-64 for 15 min (top panel) or 30 min (bottom panel). There was no significant overlap between FM4-64 labeling and either of the CVC protein markers. Proliferating cells were incubated with FM4-64 as described in the Materials and Methods, immobilized and live imaged with a Zeiss Axio Observer 7 system. Images in this figure are representative of ten experimental repeats. Scale bars: 5 µm.

et al., 2022; van der Beek et al., 2019). An inference, consistent with the implications from work in other organisms, is that the CVC is a specialized endosomal compartment. However, the CVC in *Tetrahymena* does not appear to directly receive traffic from endocytic vesicles, judging from our results with the endocytic tracer FM4-64. Our results also suggest that there is little or no inward diffusion of FM dye through the CV pore. However, the absence of FM staining of the CVC could alternatively be explained if an unusual lipid composition in the luminal leaflet of that organellar bilayer resists intercalation of FM dyes. A better understanding of ways in which the CVC is integrated into the endomembrane network will be facilitated by identifying and analyzing additional CVC-specific proteins in experimentally tractable organisms. In parallel, developing tools to manipulate a wider phylogenetic range of eukaryotes should make it possible to determine whether CVs in diverse organisms depend on evolutionarily shared mechanisms, and therefore to shed insight into the origins of this organelle (Manna et al., 2023).

MATERIALS AND METHODS

Cell strains and culture conditions

Tetrahymena thermophila strains used in this work are listed in Table S1 with culture conditions as previously described (Gorovsky et al., 1975). Cells were grown in SPP medium [2% proteose peptone (Gibco, 211684), 0.1% yeast extract (BD, 212750), 0.2% dextrose (ACROS, 41095-5000) and 0.003% EDTA, ferric-sodium salt (Sigma)] supplemented with 100 µg ml^{-1} Normocin™ (InvivoGen), an antimicrobial reagent. Cells were grown at 30°C with agitation at 100 rpm. Cell densities were measured using a spectrophotometer (Thermo Spectronic Unicam), where the optical density at 500 nm (OD_{550})=1 corresponds to ∼10^6 cells ml^{-1} (Spector et al., 1998) or a Z1 Coulter Counter (Beckman Coulter Inc., Indianapolis, Indiana). Cultures were generally used during the log phase of cell growth (cell density $2×10^5$–$4×10^5$ cells ml^{-1}).

Biolistic transformation

50 ml *Tetrahymena* cultures were grown to 500,000 cells ml^{-1} and starved for 10–16 h in 10 mM Tris-HCl buffer, pH 7.4, at 30°C with agitation. Biolistic transformations were performed as described previously (Sparvoli et al., 2018; Cassidy-Hanley et al., 1997). Transformants were identified after 3 days selection in paromomycin sulfate (120 µg ml^{-1} with 1 µg ml^{-1} of $CdCl_2$), and then serially passaged five times per week for ∼4 weeks in decreasing concentrations of $CdCl_2$ and increasing concentrations of paromomycin sulfate. Reagents were from Sigma-Aldrich unless otherwise noted.

Generation of *VMA4*-knockout strains

The macronuclear open reading frame (ORF) of the *VMA4* gene (TTHERM_00193660) was replaced with the paromomycin (Neo4) drug resistance cassette (Mochizuki, 2008) via homologous recombination with the linearized vectors pVMA4KO-Neo4. PCR was used to amplify the fragments of the genomic regions upstream (5′UTR), 1248 bp and downstream (3′UTR), 1481 bp of the ORF. The amplified fragments were subsequently cloned into restriction sites generated by NotI/PstI for the upstream fragment and BamHI/XhoI for the downstream fragment, flanking the Neo4 cassette of the pNeo4 vector, by Quick Ligation (New England, Biolabs Inc.). The primers used to create these constructs are listed in Table S2. The construct was linearized by digestion with SacI and KpnI and transformed into CU428.1 cells by biolistic transformation. Restriction enzyme reagents were from New England BioLabs.

Endogenous expression of the CVC-related genes with mNeon fluorescent tags

The p2mNeon-6myc-Neo4 vector (Sparvoli et al., 2018) was designed to integrate two mNeonGreen fluorescent tags at the C-terminus of a targeted macronuclear target gene. For each target gene, we used PCR with a proofreading Taq polymerase (Roche, Expand Long Template PCR System) to amplify the C-terminal region (∼0.5–1 kb, but not including the stop codon) as a 5′-flanking fragment, and the 3′UTR as a 3′-flanking fragment. The PCR products were verified by agarose gel electrophoresis and the purified DNA fragments were cloned into p2mNeon-6myc-Neo4 vector at the Xbal site for 5′-flanking fragments and the Xhol site for 3′-flanking fragments, respectively, by using NEBuilder HiFi DNA assembly. The final construct was verified by restriction mapping, and constructs were isolated from 50 ml bacterial cultures using a plasmid DNA extraction kit (Takara Bio USA, Inc. NucleoSpin Plasmid). DNA concentrations were measured by a NanoDrop spectrophotometer. 20 µg of each construct was linearized with PvuII and then purified for each biolistic transformation. The primers used are listed in Table S2. DNA constructs are available in the *Tetrahymena* stock center (https://tetrahymena.vet.cornell.edu).

Dual endogenous gene tagging

pVPS8D-3xmCherry-2HA-CHX was previously constructed to endogenously express mCherry-tagged Vps8Dp (Sparvoli et al., 2020). We modified the construct to replace the cycloheximide (CHX) selection cassette (bounded by PstI and XhoI sites) with a cassette conferring resistance to puromycin, which we obtained by amplifying the selectable Pur4 marker by PCR from the pPur4-opt vector (Iwamoto et al., 2014). Assembly was using the NEBuilder HiFi DNA Assembly method. The pVPS8D-3xmCherry-2HA-PUR4 was biolistically transformed into cells already expressing Dop1p–mNeon or Vma4p–mNeon.

Cell immobilization for live imaging

We used two methods for cell immobilization for live-cell imaging. For both methods, we prepared a single slide at a time and viewed it immediately. The first method relied on the pressure exerted on small volume samples under a cover slip. Cells were first concentrated by centrifugation (1000 ***g*** for 1 min) to 2×10^6–5×10^6 cells ml^{-1}. 6 µl of sample was applied to the slide, and immediately overlayed with a 22×22-1 cover slip. The resulting pressure frequently results in cell immobilization, which could be verified by monitoring ciliary beating on the cell surface at the same time that cell viability could be monitored by observing the periodic contraction of the CV, both in the DIC channel. For the second method, cells were pelleted (1000 ***g*** for 1 min) and resuspended in a thermoreversible gel on ice, whose viscosity increases when it is warmed to room temperature. Cells at the same high density were mixed well with CyGEL™ (ab109204, Abcam) (the mix ratio was optimized for each experiment) and immediately mounted with a coverslip. This approach results in many cells being effectively immobilized in the thin gel. For both methods, we carefully watched for proliferation of large cytosolic vesicles. Proliferating cells have large food vacuoles derived from the oral apparatus. No new food vacuoles form in immobilized cells, so any substantial increase in the number of such vesicles is likely to represent autophagosome formation as part of a stress response. We rejected any cells showing such an increase.

Cell fixation for imaging

Cells were fixed in a final concentration of 4% paraformaldehyde (stock: 16% paraformaldehyde solution in distilled water, EM grade, 15710, Electron Microscopy Science) for 10–30 min at room temperature. They were then washed repeatedly in PBS to reduce the background autofluorescence, before staining with DAPI at final concentration of 50 ng ml^{-1} for 10 min for nuclear staining, and/or staining with antibodies for immunofluorescence. To improve preservation of the tubular structure of the spongiome, we fixed cells with 3% paraformaldehyde for 10 min on ice. Images were captured by using a Carl Zeiss Microscope stand Axio Observer 7 system or Marianas Yokogawa-type spinning disc inverted confocal microscope.

FRAP

Cells were immobilized as described above. FRAP experiments were performed using a Marianas Yokogawa-type spinning disc inverted confocal microscope with a 100×/NA1.45 oil (Alpha Plan-Fluar) objective. The system featured fast shutter speeds and channel switching for high-speed imaging and a vector high-speed point scanner for bleaching, controlled using Slidebook software. For each experiment, we first identified a well-immobilized cell and verified the fluorescence signal with a ∼100–500 ms exposure. We then used the time-lapse mode to capture images with the fastest camera speed for a pre-photobleaching record and then used the screen selection tool and real-time imaging to draw a region of interest (ROI) for photobleaching.

Image analysis

The image processing package FIJI was used for image processing and analysis (Schindelin et al., 2012). Processing of raw images included: image cropping and rotation, bleach correction, background subtraction, adjustment of brightness/contrast, color switching, selection of images from z-stacks, intensity threshold adjustments, and measurements of parameters including areas, mean gray values and integrated densities. The Radial Profile plugin (https://imagej.net/ij/plugins/radial-profile.html) was used to measure and plot the intensity of fluorescence signal along specified radii. An ROI corresponding to the CV bladder was created as a circle whose center corresponded with the apparent bladder center and whose circumference included the entire visible CV periphery. The normalized integrated intensity of the tagged fluorescent protein was calculated along many radii, and the average intensity at each radial position was plotted as a function of distance from the circle center.

To quantify fluorescence intensities in the CV versus cytosol, all images were captured using the same microscopy settings. The raw images were used to adjust the threshold signal intensity for segmenting the whole cell area from extracellular background, and for segmenting the CV area from the cytosol, both using Binary selection with Fill Holes. The sum fluorescence intensities of the whole cell and the CV area were then measured. For FRAP analysis, the time-lapse images were separately adjusted by bleach correction for the pre-photobleaching series and after-photobleaching series. The intensity thresholds were adjusted for background subtraction, and intensity changes over time were measured in ROIs. Intensities were plotted using GraphPad Software Prism.

Osmotic challenge

Cells expressing tagged proteins were grown to log growth phase in SPP medium. For hypo-osmotic treatment, cells were pelleted by centrifugation at

1000 ***g*** for 1 min and resuspended gently in 10 mM Tris-HCl buffer, pH 7.4 for 1 min. This process was repeated, and the cells were then incubated in the same buffer, at room temperature, for 10 min before being fixed for imaging.

Immunofluorescence analysis

Cells (2×10^5) were fixed with 4% paraformaldehyde for 30 min at room temperature, and immunolabeled as previously described (Briguglio et al., 2013; Bowman and Turkewitz, 2001). Briefly, cells were first incubated for blocking with 5% bovine serum albumin (BSA, BP1600-1 Thermo Fisher Scientific) in PBT [PBS with 0.3% Triton X-100 (ACROS) in PBS] for 1 h at room temperature and then incubated with the primary antibodies in the same blocking buffer. Anti-α-Tubulin antibody (clone DM1A ZooMAb® Mouse Monoclonal, Sigma ZMS1039) was used at 1:2000, anti-acetyl-lysine 40-α-tubulin antibody (monoclonal 6-11 B-1, Sigma) and anti-centrin antibody (monoclonal 20H5, EMD Millipore) at 1:500 (Jiang et al., 2020) overnight at 4°C, followed by three washes in PBT. The secondary antibodies were Texas Red-conjugated anti-mouse-IgG, incubated for 1 h at room temperature (1:1000, Texas Red Goat anti-Mouse IgG, Invitrogen T2767), and similarly washed. Cell nuclei were stained with DAPI (50 ng ml^{-1}).

Expansion microscopy

The method was adapted from Damstra et al. (2022). Growing cells were fixed with 4% PFA for 10 min at room temperature. Fixed cells were incubated with 0.1 mg ml-1 acryloyl X-SE (AcX, 2541676, Invitrogen) for a minimum of 3 h in a dark humidified chamber. For gelation, 194 µl (for two samples) of the monomer solution (sodium acrylate 1.1 M; acrylamide 2 M; N,N′-methylenebisacrylamide 0.009% in PBS) was prepared and kept on ice. Tetramethylethylendiamine (TEMED, 11042F, Gibco BRL, 3 µl of 10% stock in water) and ammonium persulfate (A3678, Sigma, 3 µl of 10% stock in water) were added and quickly mixed on ice, and 97 µl of gelation solution was mixed on the slide with 3 µl of concentrated fixed cells. The slides were incubated in the dark at 37°C for 1 h, after which proteinase K (42-700, Apex Bioresearch) was added (final concentration 7.5 units ml^{-1}) for at least 2 h in the dark at 37°C. Afterward, the gels were gently removed and transferred to a 15 cm Petri dish with three successive water washes water for promotion of expansion. The extent of anisotropic expansion was estimated by measuring the diameter of the gels in two orthogonal directions. For imaging, small pieces were cut from the gel and mounted (cells facing down) on the coverslip (glass bottom microwell dishes, part no. P35G-1.5-10-C), which had been pre-coated by adding ∼70 µl of 20% poly-L solution and dried for 30–60 min on a 37°C heat block. Finally, 20 µl of water was added and the sample covered with a second cover slip.

Endogenous expression of FLAG-tagged Dop1p, cryomilled cell powder preparation and FLAG immunoprecipitations

p-FLAG-ZZ-Neo4 was used to construct and generate a strain expressing endogenous Dop1p with a FLAG epitope at the C-terminus of the *DOP1* genomic locus. The initial Dop1p–FLAG-expressing transformants were serially passaged at least 20 times, while increasing the concentration of paromomycin from 120 µg/ml to 1000 µg/ml and decreasing the inducer concentration of $CdCl_2$ from 1 µg/ml to 0.05 µg/ml. Cryomilling was based on previous procedures (Obado et al., 2016; Sparvoli et al., 2020). 10 l cultures of Dop1p–FLAG-expressing CU428 cells were grown to 2×10^5 – 5×10^5 cells/ml, washed once with 10 mM Tris-HCl pH 7.4 and re-pelleted (1000 ***g*** for 10 min). Supernatants were rapidly aspirated to leave a dense cell slurry. The slurries were dripped from a volumetric pipette into liquid nitrogen, and the frozen beads collected and milled to powders using a Cryogenic Grinder 6875 freezer mill, and stored at −75°C.

Pulldowns were as performed described previously (Sparvoli et al., 2020); 10 g of cryomilled cell powder was weighted and immediately suspended in 50 ml dissolving buffer containing 20 mM HEPES pH 7.4 and 250 mM NaCitrate on ice, supplemented with protease inhibitor cocktail tablets (Roche), gently mixed by inversion for 1 h at 4°C, and then on ice until no solid matter was visible. The solutes were then centrifuged at 140,000 ***g*** (Beckman Instruments type 45 Ti rotor) for 1.5 h at 4°C, and the supernatants transferred to new tubes, for incubation at 4°C for 2 h with anti-FLAG beads (EZ view Red Anti-FLAG M2 affinity Gel, Sigma) which had been pre-washed with lysis buffer for 2 h at 4°C. The beads were then washed five times with 20 mM Tris-HCl pH 7.4, 1 mM EDTA, 500 mM NaCl, 0.1% NP-40, 1 mM DTT and 10% glycerol supplemented with protease inhibitor cocktail (Roche) and eluted with 60 µl of 4× LDS sample buffer (988 mM Tris, 2.04 mM EDTA, 8% lithium dodecyl sulfate, 40% Glycerol, 0.88% Commassie Brilliant Blue G250, 0.7 mM Phenol red) plus 40 mM DTT for further SDS-PAGE electrophoresis. Protein samples were electrophoresed on a 4–20% gel SDS-PAGE gel to verify pulldown efficiency by Coomassie Blue staining and western blotting using anti-FLAG antibody as below. The eluted sample (total in 60 µl sample buffer) was used to run an SDS-PAGE, with the dye front allowed to electrophorese ∼1 cm into the gel. The gel was then stained with Coomassie Blue R-250 solution (0.1% w/v Coomassie, 10% acetic acid and 50% methanol) to visualize the lane. A single 1 cm gel slice was excised and prepared for protein identification via mass spectrometry.

Mass spectrometry

The protein containing gel slice was destained, and then subjected to tryptic digest and reductive alkylation using standard procedures. LC-MS/MS was performed by the OMICS Proteomics Facility at Biocev on a Ultimate3000 nano rapid separation LC system (Dionex) coupled to a Orbitrap Fusion mass spectrometer (Thermo Fisher Scientific). Mass spectra were processed using the intensity-based label-free quantification (LFQ) method of MaxQuant version 1.6.6.0 (Cox and Mann, 2008; Cox et al., 2014) searching the *T. thermophila* annotated protein database from https://ciliates.org/ (Eisen et al., 2006; Stover et al., 2006). The minimum peptide length was set at seven amino acids and false discovery rates (FDR) of 0.01 were calculated at the levels of peptides, proteins and modification sites based on the number of hits against the reversed sequence database. If the identified peptide sequence set of one protein contained the peptide set of another protein, these two proteins were assigned to the same protein group. Potential interactors were ranked by enrichment ratios comparing to a control sample and respective LFQ intensities. Proteomics data have been deposited to the ProteomeXchange Consortium via the PRIDE partner repository (Perez-Riverol et al., 2019) with the dataset identifier PXD043302.

Western blotting

Total cell protein extract and immunoprecipitated samples were analyzed by western blotting as previously described (Sparvoli et al., 2018). Proteins were resolved with the Novex NuPAGE Gel system (8% or 4–20% Tris-Glycine gels, Invitrogen), and transferred to 0.2 µm PVDF membranes (Thermo Scientific). Blots were incubated with anti-FLAG (1:2000 dilution, F1804, Sigma) antibodies for overnight at 4°C after pre-blocking with 3% BSA in TBST (1× Tris-buffered saline with 0.1% Tween 20). Secondary antibody conjugated to ECL Horseradish Peroxidase (NA931) (GE Healthcare Life Sciences, Little Chalfont, UK) was diluted 1:20,000 for incubation with the blots, and signal was visualized by SuperSignal West Femto Maximum Sensitivity Substrate (Thermo Fisher Scientific).

FM4-64 staining of Vps8Dp-mNeon expressing cells

Proliferating Vps8Dp–mNeon-expressing cells were incubated with 5 µM FM4-64 (Invitrogen) and then washed twice with S-medium. After 30 min, cells were mounted and immobilized on slides for live imaging in a Zeiss Axio Observer 7 microscope.

Colocalization analysis

To estimate the extent of colocalization, the Fiji-JACoP plugin was used to calculate Manders' coefficients M1 and M2 (Bolte and Cordelières, 2006) between two images captured in different channels. M1 is defined as the fraction of the channel A image overlapping the channel B image, and M2 is defined conversely.

Dictyostelium cells, growth conditions and FM4-64 staining

Dictyostelium discoideum wild-type strain AX2 cells (a kind gift of Andrew Maselli, Chicago State University, USA) were cultivated in HL5 medium (Ashworth and Watts, 1970) on tissue culture-treated plastic 150 mm plates (Fisherbrand Tissue Culture Dish) at 21°C. For FM4-64 staining,

proliferating cells were scraped from the plate and suspended in a tube of fresh HL5 medium with 5 µM FM4-64 for 5 min. The cells were mounted on slides for live imaging in a Zeiss Axio Observer 7 microscope.

Acknowledgements
We thank Daniela Sparvoli for the Vps8D–mCherry construct and advice on expansion microscopy, and Masaaki Iwamoto (Nihon University) for the puromycin drug selection plasmid. At the University of Chicago, we thank Vytas Bindokas and Christine Labno for help at the Integrated Light Microscopy Core Facility. In the Turkewitz laboratory, we thank Patrick Jiang, Maya Waarts and Josefina Hernandez for helpful discussions.

Competing interests
The authors declare no competing or financial interests.

Author contributions
Conceptualization: C.-Y.C., A.P.T.; Methodology: C.-Y.C., M.Z., M.-C.Y., A.P.T.; Investigation: C.-Y.C., D.P.R., M.Z.; Resources: D.P.R., M.Z., M.-C.Y., A.P.T.; Writing - original draft: C.-Y.C., A.P.T.; Writing - review & editing: C.-Y.C., D.P.R., M.Z., M.-C.Y., A.P.T.; Supervision: M-C.Y., A.P.T.; Project administration: M.-C.Y., A.P.T.; Funding acquisition: M.-C.Y., A.P.T.

Funding
Work in A.P.T.'s laboratory was supported by the National Institutes of Health (NIH) (GM105783) and the National Science Foundation (MCB 1937326). Work in M.-C.Y's laboratory was supported by the Ministry of Science and Technology of Taiwan (MOST 105-2311-B-001-057-MY2), and the Institute of Molecular Biology, Academia Sinica of Taiwan. Deposited in PMC for release after 12 months.

Data availability
Proteomics data have been deposited to the ProteomeXchange Consortium via the PRIDE partner repository (Perez-Riverol et al., 2019) with the dataset identifier PXD043302.

Peer review history
The peer review history is available online at https://journals.biologists.com/jcs/lookup/doi/10.1242/jcs.261511.reviewer-comments.pdf

References
Allen, R. D. (2000). The contractile vacuole and its membrane dynamics. *BioEssays* **22**, 1035-1042. doi:10.1002/1521-1878(200011)22:11<1035::AID-BIES10>3.0.CO;2-A

Allen, R. D. and Naitoh, Y. (2002). Osmoregulation and contractile vacuoles of protozoa. *Int. Rev. Cytol.* **215**, 351-394. doi:10.1016/S0074-7696(02)15015-7

Ashworth, J. M. and Watts, D. J. (1970). Metabolism of the cellular slime mould Dictyostelium discoideum grown in axenic culture. *Biochem. J.* **119**, 175-182. doi:10.1042/bj1190175

Balderhaar, H. J. and Ungermann, C. (2013). CORVET and HOPS tethering complexes - coordinators of endosome and lysosome fusion. *J. Cell Sci.* **126**, 1307-1316. doi:10.1242/jcs.107805

Becker, M., Matzner, M. and Gerisch, G. (1999). Drainin required for membrane fusion of the contractile vacuole in Dictyostelium is the prototype of a protein family also represented in man. *EMBO J.* **18**, 3305-3316. doi:10.1093/emboj/18.12.3305

Betz, W. J. and Bewick, G. S. (1992). Optical analysis of synaptic vesicle recycling at the frog neuromuscular junction. *Science* **255**, 200-203. doi:10.1126/science.1553547

Betz, W. J., Mao, F. and Smith, C. B. (1996). Imaging exocytosis and endocytosis. *Curr. Opin. Neurobiol.* **6**, 365-371. doi:10.1016/S0959-4388(96)80121-8

Bolte, S. and Cordelières, F. P. (2006). A guided tour into subcellular colocalization analysis in light microscopy. *J. Microsc.* **224**, 213-232. doi:10.1111/j.1365-2818.2006.01706.x

Bowman, G. R. and Turkewitz, A. P. (2001). Analysis of a mutant exhibiting conditional sorting to dense core secretory granules in Tetrahymena thermophila. *Genetics* **159**, 1605-1616. doi:10.1093/genetics/159.4.1605

Bright, L. J., Kambesis, N., Nelson, S. B., Jeong, B. and Turkewitz, A. P. (2010). Comprehensive analysis reveals dynamic and evolutionary plasticity of Rab GTPases and membrane traffic in Tetrahymena thermophila. *PLoS Genet.* **6**, e1001155. doi:10.1371/journal.pgen.1001155

Briguglio, J. S., Kumar, S. and Turkewitz, A. P. (2013). Lysosomal sorting receptors are essential for secretory granule biogenesis in Tetrahymena. *J. Cell Biol.* **203**, 537-550. doi:10.1083/jcb.201305086

Bush, J., Nolta, K., Rodriguez-Paris, J., Kaufmann, N., O'halloran, T., Ruscetti, T., Temesvari, L., Steck, T. and Cardelli, J. (1994). A Rab4-like GTPase in Dictyostelium discoideum colocalizes with V-H(+)-ATPases in reticular membranes of the contractile vacuole complex and in lysosomes. *J. Cell Sci.* **107**, 2801-2812. doi:10.1242/jcs.107.10.2801

Cassidy-Hanley, D., Bowen, J., Lee, J. H., Cole, E., Verplank, L. A., Gaertig, J., Gorovsky, M. A. and Bruns, P. J. (1997). Germline and somatic transformation of mating Tetrahymena thermophila by particle bombardment. *Genetics* **146**, 135-147. doi:10.1093/genetics/146.1.135

Cheng, C. Y., Young, J. M., Lin, C. G., Chao, J. L., Malik, H. S. and Yao, M. C. (2016). The piggyBac transposon-derived genes TPB1 and TPB6 mediate essential transposon-like excision during the developmental rearrangement of key genes in Tetrahymena thermophila. *Genes Dev.* **30**, 2724-2736. doi:10.1101/gad.290460.116

Cole, E. and Gaertig, J. (2022). Anterior-posterior pattern formation in ciliates. *J. Eukaryot. Microbiol.* **69**, e12890. doi:10.1111/jeu.12890

Collins, M. P. and Forgac, M. (2020). Regulation and function of V-ATPases in physiology and disease. *Biochim. Biophys. Acta Biomembr.***1862**, 183341. doi:10.1016/j.bbamem.2020.183341

Cox, J. and Mann, M. (2008). MaxQuant enables high peptide identification rates, individualized p.p.b.-range mass accuracies and proteome-wide protein quantification. *Nat. Biotechnol.* **26**, 1367-1372. doi:10.1038/nbt.1511

Cox, J., Hein, M. Y., Luber, C. A., Paron, I., Nagaraj, N. and Mann, M. (2014). Accurate proteome-wide label-free quantification by delayed normalization and maximal peptide ratio extraction, termed MaxLFQ. *Mol. Cell. Proteomics* **13**, 2513-2526. doi:10.1074/mcp.M113.031591

Damstra, H. G. J., Mohar, B., Eddison, M., Akhmanova, A., Kapitein, L. C. and Tillberg, P. W. (2022). Visualizing cellular and tissue ultrastructure using Ten-fold Robust Expansion Microscopy (TREx). *Elife* **11**, e73775. doi:10.7554/eLife.73775

Docampo, R., Jimenez, V., Lander, N., Li, Z. H. and Niyogi, S. (2013). New insights into roles of acidocalcisomes and contractile vacuole complex in osmoregulation in protists. *Int. Rev. Cell Mol. Biol.* **305**, 69-113. doi:10.1016/B978-0-12-407695-2.00002-0

Du, F., Edwards, K., Shen, Z., Sun, B., De Lozanne, A., Briggs, S. and Firtel, R. A. (2008). Regulation of contractile vacuole formation and activity in Dictyostelium. *EMBO J.* **27**, 2064-2076. doi:10.1038/emboj.2008.131

Eisen, J. A., Coyne, R. S., Wu, M., Wu, D., Thiagarajan, M., Wortman, J. R., Badger, J. H., Ren, Q., Amedeo, P., Jones, K. M. et al. (2006). Macronuclear genome sequence of the ciliate Tetrahymena thermophila, a model eukaryote. *PLoS Biol.* **4**, e286. doi:10.1371/journal.pbio.0040286

Elde, N. C., Morgan, G., Winey, M., Sperling, L. and Turkewitz, A. P. (2005). Elucidation of clathrin-mediated endocytosis in tetrahymena reveals an evolutionarily convergent recruitment of dynamin. *PLoS Genet.* **1**, e52. doi:10.1371/journal.pgen.0010052

Elliott, A. M. and Bak, I. J. (1964). Contractile vacuole+related structures in tetrahymena pyriformis. *J. Protozool.* **11**, 250-261. doi:10.1111/j.1550-7408.1964.tb01752.x

Essid, M., Gopaldass, N., Yoshida, K., Merrifield, C. and Soldati, T. (2012). Rab8a regulates the exocyst-mediated kiss-and-run discharge of the Dictyostelium contractile vacuole. *Mol. Biol. Cell* **23**, 1267-1282. doi:10.1091/mbc.e11-06-0576

Fok, A. K., Clarke, M., Ma, L. and Allen, R. D. (1993). Vacuolar H(+)-ATPase of Dictyostelium discoideum. A monoclonal antibody study. *J. Cell Sci.* **106**, 1103-1113. doi:10.1242/jcs.106.4.1103

Fok, A. K., Aihara, M. S., Ishida, M., Nolta, K. V., Steck, T. L. and Allen, R. D. (1995). The pegs on the decorated tubules of the contractile vacuole complex of Paramecium are proton pumps. *J. Cell Sci.* **108**, 3163-3170. doi:10.1242/jcs.108.10.3163

Frankel, J. (1992). Positional information in cells and organisms. *Trends Cell Biol.* **2**, 256-260. doi:10.1016/0962-8924(92)90191-O

Frankel, J. (2000). Cell biology of Tetrahymena thermophila. *Methods Cell Biol.* **62**, 27-125. doi:10.1016/S0091-679X(08)61528-9

Gabriel, D., Hacker, U., Kohler, J., Muller-Taubenberger, A., Schwartz, J. M., Westphal, M. and Gerisch, G. (1999). The contractile vacuole network of Dictyostelium as a distinct organelle: its dynamics visualized by a GFP marker protein. *J. Cell Sci.* **112**, 3995-4005. doi:10.1242/jcs.112.22.3995

Gaertig, J., Cruz, M. A., Bowen, J., Gu, L., Pennock, D. G. and Gorovsky, M. A. (1995). Acetylation of lysine 40 in alpha-tubulin is not essential in Tetrahymena thermophila. *J. Cell Biol.* **129**, 1301-1310. doi:10.1083/jcb.129.5.1301

Gerald, N. J., Siano, M. and De Lozanne, A. (2002). The Dictyostelium LvsA protein is localized on the contractile vacuole and is required for osmoregulation. *Traffic* **3**, 50-60. doi:10.1034/j.1600-0854.2002.30107.x

Gerisch, G., Heuser, J. and Clarke, M. (2002). Tubular-vesicular transformation in the contractile vacuole system of Dictyostelium. *Cell Biol. Int.* **26**, 845-852. doi:10.1006/cbir.2002.0938

Girard-Dias, W., Alcantara, C. L., Cunha-E-Silva, N., De Souza, W. and Miranda, K. (2012). On the ultrastructural organization of Trypanosoma cruzi using cryopreparation methods and electron tomography. *Histochem. Cell Biol.* **138**, 821-831. doi:10.1007/s00418-012-1002-8

Gorovsky, M. A., Yao, M. C., Keevert, J. B. and Pleger, G. L. (1975). Isolation of micro- and macronuclei of Tetrahymena pyriformis. *Methods Cell Biol.* **9**, 311-327. doi:10.1016/S0091-679X(08)60080-1

Gronlien, H. K., Stock, C., Aihara, M. S., Allen, R. D. and Naitoh, Y. (2002). Relationship between the membrane potential of the contractile vacuole complex

and its osmoregulatory activity in Paramecium multimicronucleatum. *J. Exp. Biol.* **205**, 3261-3270. doi:10.1242/jeb.205.20.3261

Hankins, H. M., Baldridge, R. D., Xu, P. and Graham, T. R. (2015). Role of flippases, scramblases and transfer proteins in phosphatidylserine subcellular distribution. *Traffic* **16**, 35-47. doi:10.1111/tra.12233

Harris, E., Yoshida, K., Cardelli, J. and Bush, J. (2001). Rab11-like GTPase associates with and regulates the structure and function of the contractile vacuole system in dictyostelium. *J. Cell Sci.* **114**, 3035-3045. doi:10.1242/jcs.114.16.3035

Heuser, J. (2006). Evidence for recycling of contractile vacuole membrane during osmoregulation in Dictyostelium amoebae–a tribute to Gunther Gerisch. *Eur. J. Cell Biol.* **85**, 859-871. doi:10.1016/j.ejcb.2006.05.011

Heuser, J., Zhu, Q. and Clarke, M. (1993). Proton pumps populate the contractile vacuoles of Dictyostelium amoebae. *J. Cell Biol.* **121**, 1311-1327. doi:10.1083/jcb.121.6.1311

Ishida, M., Fok, A. K., Aihara, M. S. and Allen, R. D. (1996). Hyperosmotic stress leads to reversible dissociation of the proton pump-bearing tubules from the contractile vacuole complex in Paramecium. *J. Cell Sci.* **109**, 229-237. doi:10.1242/jcs.109.1.229

Ishida, M., Hori, M., Ooba, Y., Kinoshita, M., Matsutani, T., Naito, M., Hagimoto, T., Miyazaki, K., Ueda, S., Miura, K. et al. (2021). A functional Aqp1 gene product localizes on the contractile vacuole complex in paramecium multimicronucleatum. *J. Eukaryot. Microbiol.* **68**, e12843. doi:10.1111/jeu.12843

Iwamoto, M., Mori, C., Hiraoka, Y. and Haraguchi, T. (2014). Puromycin resistance gene as an effective selection marker for ciliate Tetrahymena. *Gene* **534**, 249-255. doi:10.1016/j.gene.2013.10.049

Jiang, Y. Y., Maier, W., Baumeister, R., Minevich, G., Joachimiak, E., Ruan, Z., Kannan, N., Clarke, D., Frankel, J. and Gaertig, J. (2017). The Hippo pathway maintains the equatorial division plane in the ciliate tetrahymena. *Genetics* **206**, 873-888. doi:10.1534/genetics.117.200766

Jiang, Y. Y., Maier, W., Baumeister, R., Joachimiak, E., Ruan, Z., Kannan, N., Clarke, D., Louka, P., Guha, M., Frankel, J. et al. (2019a). Two antagonistic hippo signaling circuits set the division plane at the medial position in the ciliate tetrahymena. *Genetics* **211**, 651-663. doi:10.1534/genetics.118.301889

Jiang, Y. Y., Maier, W., Baumeister, R., Minevich, G., Joachimiak, E., Wloga, D., Ruan, Z., Kannan, N., Bocarro, S., Bahraini, A. et al. (2019b). LF4/MOK and a CDK-related kinase regulate the number and length of cilia in Tetrahymena. *PLoS Genet.* **15**, e1008099. doi:10.1371/journal.pgen.1008099

Jiang, Y. Y., Maier, W., Chukka, U. N., Choromanski, M., Lee, C., Joachimiak, E., Wloga, D., Yeung, W., Kannan, N., Frankel, J. et al. (2020). Mutual antagonism between Hippo signaling and cyclin E drives intracellular pattern formation. *J. Cell Biol.* **219**, e202002077. doi:10.1083/jcb.202002077

Jimenez, V. and Docampo, R. (2015). TcPho91 is a contractile vacuole phosphate sodium symporter that regulates phosphate and polyphosphate metabolism in Trypanosoma cruzi. *Mol. Microbiol.* **97**, 911-925. doi:10.1111/mmi.13075

Jimenez, V., Miranda, K. and Augusto, I. (2022). The old and the new about the contractile vacuole of Trypanosoma cruzi. *J. Eukaryot. Microbiol.* **69**, e12939. doi:10.1111/jeu.12939

Kitching, J. (1939). The physiology of contractile vacuoles: IV. A note on the sources of the water evacuated, and on the function of contractile vacuoles in marine protozoa. *J. Exp. Biol.* **16**, 34-37. doi:10.1242/jeb.16.1.34

Linder, J. C. and Staehelin, L. A. (1979). A novel model for fluid secretion by the trypanosomatid contractile vacuole apparatus. *J. Cell Biol.* **83**, 371-382. doi:10.1083/jcb.83.2.371

Mahajan, D., Tie, H. C., Chen, B. and Lu, L. (2019). Dopey1-Mon2 complex binds to dual-lipids and recruits kinesin-1 for membrane trafficking. *Nat. Commun.* **10**, 3218. doi:10.1038/s41467-019-11056-5

Manna, P. T., Barlow, L. D., Ramirez-Macias, I., Herman, E. K. and Dacks, J. B. (2023). Endosomal vesicle fusion machinery is involved with the contractile vacuole in Dictyostelium discoideum. *J. Cell Sci.* **136**, jcs260477. doi:10.1242/jcs.260477

Marchesini, N., Ruiz, F. A., Vieira, M. and Docampo, R. (2002). Acidocalcisomes are functionally linked to the contractile vacuole of Dictyostelium discoideum. *J. Biol. Chem.* **277**, 8146-8153. doi:10.1074/jbc.M111130200

Marshansky, V. and Futai, M. (2008). The V-type H+-ATPase in vesicular trafficking: targeting, regulation and function. *Curr. Opin. Cell Biol.* **20**, 415-426. doi:10.1016/j.ceb.2008.03.015

Mckanna, J. A. (1976). Fine structure of fluid segregation organelles of Paramecium contractile vacuoles. *J. Ultrastruct. Res.* **54**, 1-10. doi:10.1016/S0022-5320(76)80002-0

Mochizuki, K. (2008). High efficiency transformation of Tetrahymena using a codon-optimized neomycin resistance gene. *Gene* **425**, 79-83. doi:10.1016/j.gene.2008.08.007

Moliere, A., Beer, K. B. and Wehman, A. M. (2022). Dopey proteins are essential but overlooked regulators of membrane trafficking. *J. Cell Sci.* **135**, jcs259628. doi:10.1242/jcs.259628

Montalvetti, A., Rohloff, P. and Docampo, R. (2004). A functional aquaporin co-localizes with the vacuolar proton pyrophosphatase to acidocalcisomes and the contractile vacuole complex of Trypanosoma cruzi. *J. Biol. Chem.* **279**, 38673-38682. doi:10.1074/jbc.M406304200

Naitoh, Y., Tominaga, T., Ishida, M., Fok, A., Aihara, M. and Allen, R. (1997). How does the contractile vacuole of Paramecium multimicronucleatum expel fluid? Modelling the expulsion mechanism. *J. Exp. Biol.* **200**, 713-721. doi:10.1242/jeb.200.4.713

Ng, S. F. (1977). Analysis of contractile vacuole pore morphogenesis in Tetrahymena pyriformis by 180 degree rotation of ciliary meridians. *J. Cell Sci.* **25**, 233-246. doi:10.1242/jcs.25.1.233

Ng, S. F. and Frankel, J. (1977). 180 degrees rotation of ciliary rows and its morphogenetic implications in Tetrahymena pyriformis. *Proc. Natl. Acad. Sci. USA* **74**, 1115-1119. doi:10.1073/pnas.74.3.1115

Nishihara, E., Shimmen, T. and Sonobe, S. (2007). New aspects of membrane dynamics of Amoeba proteus contractile vacuole revealed by vital staining with FM 4-64. *Protoplasma* **231**, 25-30. doi:10.1007/s00709-007-0247-x

Nolta, K. V., Padh, H. and Steck, T. L. (1993). An immunocytochemical analysis of the vacuolar proton pump in Dictyostelium discoideum. *J. Cell Sci.* **105**, 849-859. doi:10.1242/jcs.105.3.849

Obado, S. O., Field, M. C., Chait, B. T. and Rout, M. P. (2016). High-efficiency isolation of nuclear envelope protein complexes from trypanosomes. *Methods Mol. Biol.* **1411**, 67-80. doi:10.1007/978-1-4939-3530-7_3

Patterson, D. J. (1980). Contractile vacuoles and associated structures: their organization and function. *Biol. Rev.* **55**, 1-46. doi:10.1111/j.1469-185X.1980.tb00686.x

Perez-Riverol, Y., Csordas, A., Bai, J., Bernal-Llinares, M., Hewapathirana, S., Kundu, D. J., Inuganti, A., Griss, J., Mayer, G., Eisenacher, M. et al. (2019). The PRIDE database and related tools and resources in 2019: improving support for quantification data. *Nucleic Acids Res.* **47**, D442-D450. doi:10.1093/nar/gky1106

Plattner, H. (2010). Membrane trafficking in protozoa SNARE proteins, H+-ATPase, actin, and other key players in ciliates. *Int. Rev. Cell Mol. Biol.* **280**, 79-184. doi:10.1016/S1937-6448(10)80003-6

Plattner, H. (2013). Contractile vacuole complex–its expanding protein inventory. *Int. Rev. Cell Mol. Biol.* **306**, 371-416. doi:10.1016/B978-0-12-407694-5.00009-2

Plattner, H. (2015). The contractile vacuole complex of protists–new cues to function and biogenesis. *Crit. Rev. Microbiol.* **41**, 218-227. doi:10.3109/1040841X.2013.821650

Ritter, M., Bresgen, N. and Kerschbaum, H. H. (2021). From pinocytosis to methuosis-fluid consumption as a risk factor for cell death. *Front. Cell Dev. Biol.* **9**, 651982. doi:10.3389/fcell.2021.651982

Rohloff, P., Montalvetti, A. and Docampo, R. (2004). Acidocalcisomes and the contractile vacuole complex are involved in osmoregulation in Trypanosoma cruzi. *J. Biol. Chem.* **279**, 52270-52281. doi:10.1074/jbc.M410372200

Ruehle, M. D., Orias, E. and Pearson, C. G. (2016). Tetrahymena as a unicellular model eukaryote: genetic and genomic tools. *Genetics* **203**, 649-665. doi:10.1534/genetics.114.169748

Schindelin, J., Arganda-Carreras, I., Frise, E., Kaynig, V., Longair, M., Pietzsch, T., Preibisch, S., Rueden, C., Saalfeld, S., Schmid, B. et al. (2012). Fiji: an open-source platform for biological-image analysis. *Nat. Methods* **9**, 676-682. doi:10.1038/nmeth.2019

Schonemann, B., Bledowski, A., Sehring, I. M. and Plattner, H. (2013). A set of SNARE proteins in the contractile vacuole complex of Paramecium regulates cellular calcium tolerance and also contributes to organelle biogenesis. *Cell Calcium* **53**, 204-216. doi:10.1016/j.ceca.2012.11.016

Spallanzani, L. (1776). *Opuscoli di fisica animale e vegetabile*. Modena: Societa Tipografica.

Sparvoli, D., Richardson, E., Osakada, H., Lan, X., Iwamoto, M., Bowman, G. R., Kontur, C., Bourland, W. A., Lynn, D. H., Pritchard, J. K. et al. (2018). Remodeling the specificity of an endosomal CORVET tether underlies formation of regulated secretory vesicles in the ciliate Tetrahymena thermophila. *Curr. Biol.* **28**, 697-710.e13. doi:10.1016/j.cub.2018.01.047

Sparvoli, D., Zoltner, M., Cheng, C. Y., Field, M. C. and Turkewitz, A. P. (2020). Diversification of CORVET tethers facilitates transport complexity in Tetrahymena thermophila. *J. Cell Sci.* **133**, jcs238659. doi:10.1242/jcs.238659

Spector, D. L., Goldman, R. D. and Leinwand, L. A. (1998). *Cells: A Laboratory Manual, Volume 1, Chapter 18, Culture and Manipulation of Tetrahymena*. Cold Spring Harbor Laboratory Press.

Stock, C., Allen, R. D. and Naitoh, Y. (2001). How external osmolarity affects the activity of the contractile vacuole complex, the cytosolic osmolarity and the water permeability of the plasma membrane in Paramecium multimicronucleatum. *J. Exp. Biol.* **204**, 291-304. doi:10.1242/jeb.204.2.291

Stock, C., Gronlien, H. K. and Allen, R. D. (2002a). The ionic composition of the contractile vacuole fluid of Paramecium mirrors ion transport across the plasma membrane. *Eur. J. Cell Biol.* **81**, 505-515. doi:10.1078/0171-9335-00272

Stock, C., Gronlien, H. K., Allen, R. D. and Naitoh, Y. (2002b). Osmoregulation in Paramecium: in situ ion gradients permit water to cascade through the cytosol to the contractile vacuole. *J. Cell Sci.* **115**, 2339-2348. doi:10.1242/jcs.115.11.2339

Stover, N. A., Krieger, C. J., Binkley, G., Dong, Q., Fisk, D. G., Nash, R., Sethuraman, A., Weng, S. and Cherry, J. M. (2006). Tetrahymena Genome Database (TGD): a new genomic resource for Tetrahymena thermophila research. *Nucleic Acids Res.* **34**, D500-D503. doi:10.1093/nar/gkj054

Tani, T., Allen, R. D. and Naitoh, Y. (2000). Periodic tension development in the membrane of the in vitro contractile vacuole of Paramecium multimicronucleatum: modification by bisection, fusion and suction. *J. Exp. Biol.* **203**, 239-251. doi:10.1242/jeb.203.2.239

Tani, T., Allen, R. D. and Naitoh, Y. (2001). Cellular membranes that undergo cyclic changes in tension: direct measurement of force generation by an in vitro contractile vacuole of Paramecium multimicronucleatum. *J. Cell Sci.* **114**, 785-795. doi:10.1242/jcs.114.4.785

Tani, T., Tominaga, T., Allen, R. D. and Naitoh, Y. (2002). Development of periodic tension in the contractile vacuole complex membrane of paramecium governs its membrane dynamics. *Cell Biol. Int.* **26**, 853-860. doi:10.1006/cbir.2002.0937

Temesvari, L. A., Rodriguez-Paris, J. M., Bush, J. M., Zhang, L. and Cardelli, J. A. (1996). Involvement of the vacuolar proton-translocating ATPase in multiple steps of the endo-lysosomal system and in the contractile vacuole system of Dictyostelium discoideum. *J. Cell Sci.* **109**, 1479-1495. doi:10.1242/jcs.109.6.1479

Tominaga, T., Allen, R. D. and Naitoh, Y. (1998a). Cyclic changes in the tension of the contractile vacuole complex membrane control its exocytotic cycle. *J. Exp. Biol.* **201**, 2647-2658. doi:10.1242/jeb.201.18.2647

Tominaga, T., Allen, R. D. and Naitoh, Y. (1998b). Electrophysiology of the in situ contractile vacuole complex of Paramecium reveals its membrane dynamics and electrogenic site during osmoregulatory activity. *J. Exp. Biol.* **201**, 451-460. doi:10.1242/jeb.201.3.451

Tominaga, T., Naitoh, Y. and Allen, R. D. (1999). A key function of non-planar membranes and their associated microtubular ribbons in contractile vacuole membrane dynamics is revealed by electrophysiologically controlled fixation of Paramecium. *J. Cell Sci.* **112**, 3733-3745. doi:10.1242/jcs.112.21.3733

Turkewitz, A. P. and Bright, L. J. (2011). A Rab-based view of membrane traffic in the ciliate Tetrahymena thermophila. *Small GTPases* **2**, 222-226. doi:10.4161/sgtp.2.4.16706

Ulrich, P. N., Jimenez, V., Park, M., Martins, V. P., Atwood, J., 3rd, Moles, K., Collins, D., Rohloff, P., Tarleton, R., Moreno, S. N. et al. (2011). Identification of contractile vacuole proteins in Trypanosoma cruzi. *PLoS One* **6**, e18013. doi:10.1371/journal.pone.0018013

Van Der Beek, J., Jonker, C., Van Der Welle, R., Liv, N. and Klumperman, J. (2019). CORVET, CHEVI and HOPS - multisubunit tethers of the endo-lysosomal system in health and disease. *J. Cell Sci.* **132**, jcs189134. doi:10.1242/jcs.189134

Velle, K. B., Garner, R. M., Beckford, T. K., Weeda, M., Liu, C., Kennard, A. S., Edwards, M. and Fritz-Laylin, L. K. (2023). A conserved pressure-driven mechanism for regulating cytosolic osmolarity. *Curr. Biol.* **33**, 3325-3337.e5. doi:10.1016/j.cub.2023.06.061

Wang, J., Chitsaz, F., Derbyshire, M. K., Gonzales, N. R., Gwadz, M., Lu, S., Marchler, G. H., Song, J. S., Thanki, N., Yamashita, R. A. et al. (2023). The conserved domain database in 2023. *Nucleic Acids Res.* **51**, D384-D388. doi:10.1093/nar/gkac1096

Warren, A., Patterson, D. J., Dunthorn, M., Clamp, J. C., Achilles-Day, U. E. M., Aescht, E., Al-Farraj, S. A., Al-Quraishy, S., Al-Rasheid, K., Carr, M. et al. (2017). Beyond the "code": a guide to the description and documentation of biodiversity in ciliated protists (Alveolata, Ciliophora). *J. Eukaryot. Microbiol.* **64**, 539-554. doi:10.1111/jeu.12391

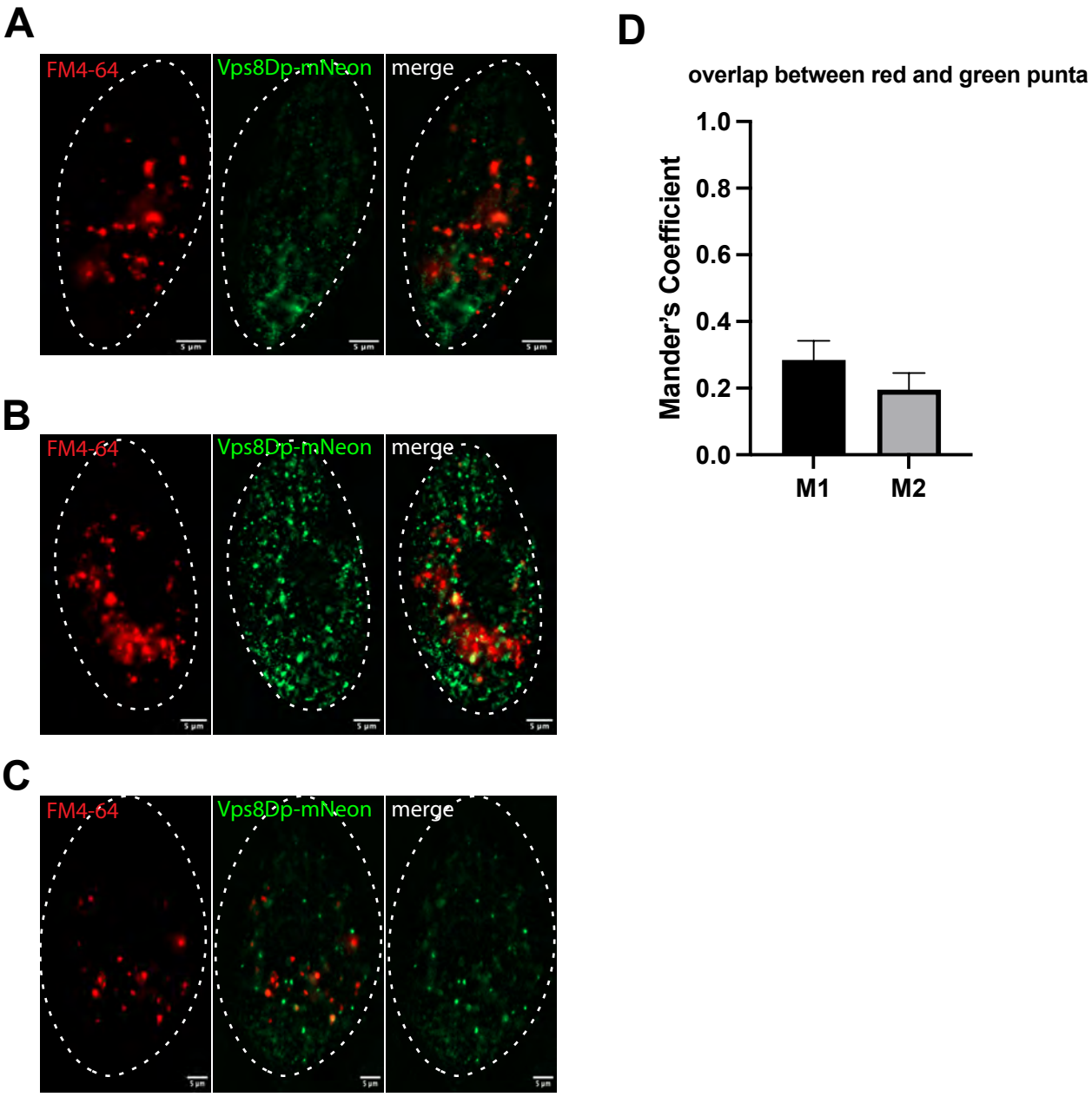

Fig. S1. Live imaging of Vps8Dp-mNeon-expressing cells after pulse-labeling by 5 μM FM4-64 for 5 min, and observed after an additional 30 min. A, B and C show images from different cells. Left panel: FM4-64 (red); middle panel, Vps8Dp-mNeon (green); right panel, merge. D: Overlap between FM4-64 and Vps8Dp-mNeon was analyzed by using Fiji-JACoP plugin to show Mander's Coefficient M1 and M2. M1 represents the percentage of the red signal overlapping with the green; M2 represents the reciprocal. Error bars represent SDs.

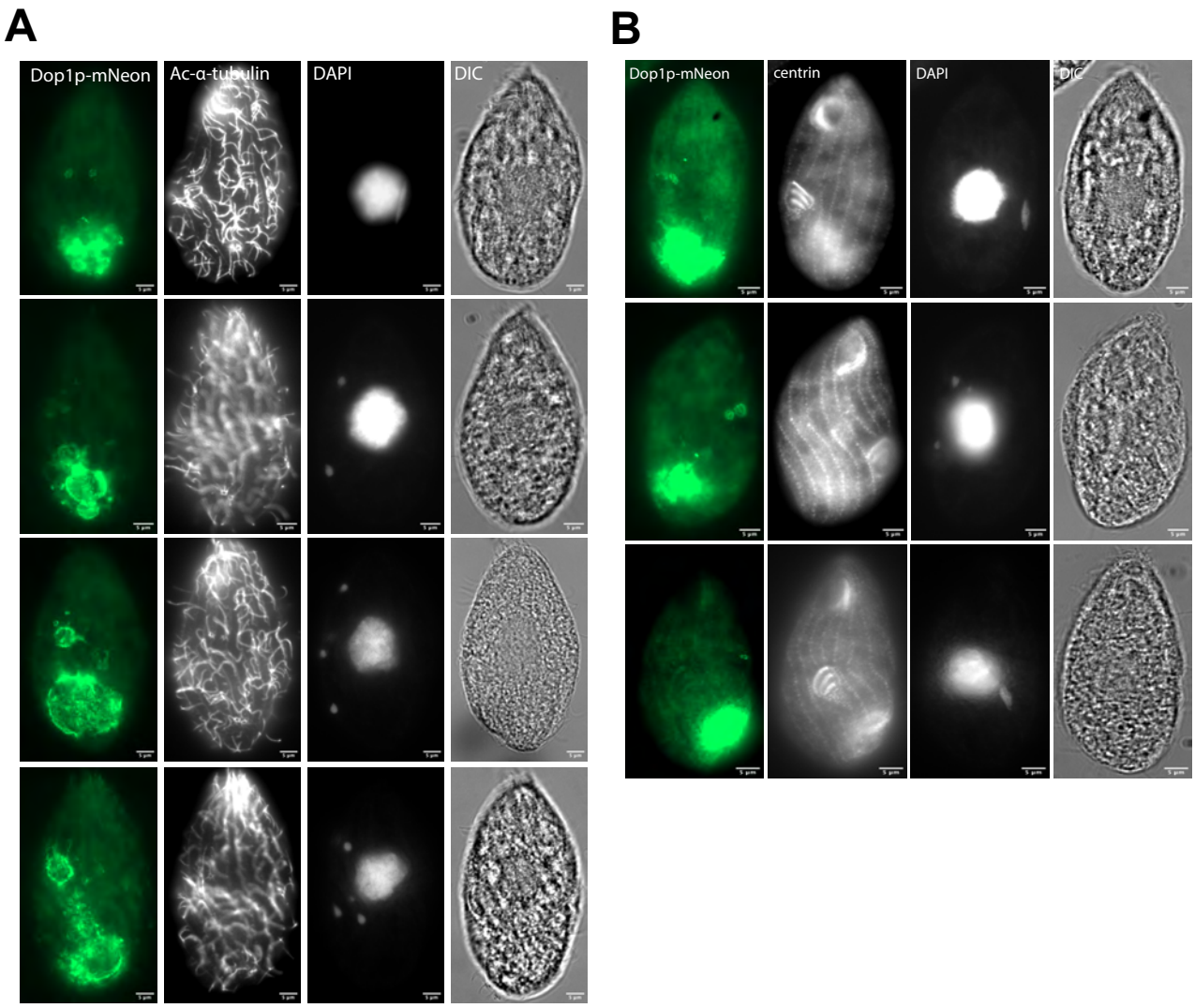

Fig. S2. Immunofluorescent staining of Acetyl-K40-α-tubulin and centrin in Dop1p-mNeon-expressing dividing cells.

A: Four Images of the new CVC in Dop1p-mNeon-expressing dividing cells with immunofluorescent staining of Acetyl-K40-α-tubulin, in a focal plane very near the cell surface to show the two new CV pores. Growing cells were fixed and stained as described in Materials and Methods. Images were taken with a Zeiss Axio Observer 7. B: Three images of the new CVC in Dop1p-mNeon-expressing dividing cells with immunofluorescent staining of centrin, in a focal plane near the cell surface to show the cortical rows of basal body position and the new oral apparatus. Growing cells were fixed and stained as described in Materials and Methods. Images were taken with a Zeiss Axio Observer 7.

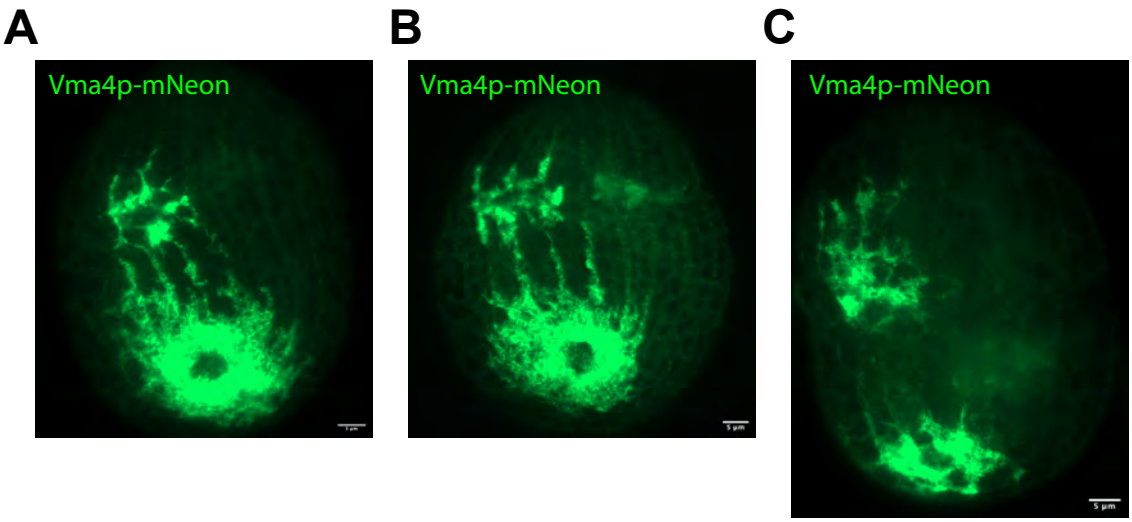

Fig. S3. Three additional images of the CVC in Vma4p-mNeon-expressing dividing cells. A and B: The newly forming CVC in the daughter cell becomes discernible as a Vma4p-labeled reticulum initiation, which seems to be interconnected with the parental CVC through a subset of cytoskeletal meridians. C: In the later stage of cell division (MAC amitosis), the developing Vma4p-labeled reticulum in the daughter cell becomes fully formed and exhibits a resemblance to the reticulum observed in the parental CVC. Growing cells were fixed as described in Materials and Methods. Images were taken with a Zeiss Axio Observer 7.

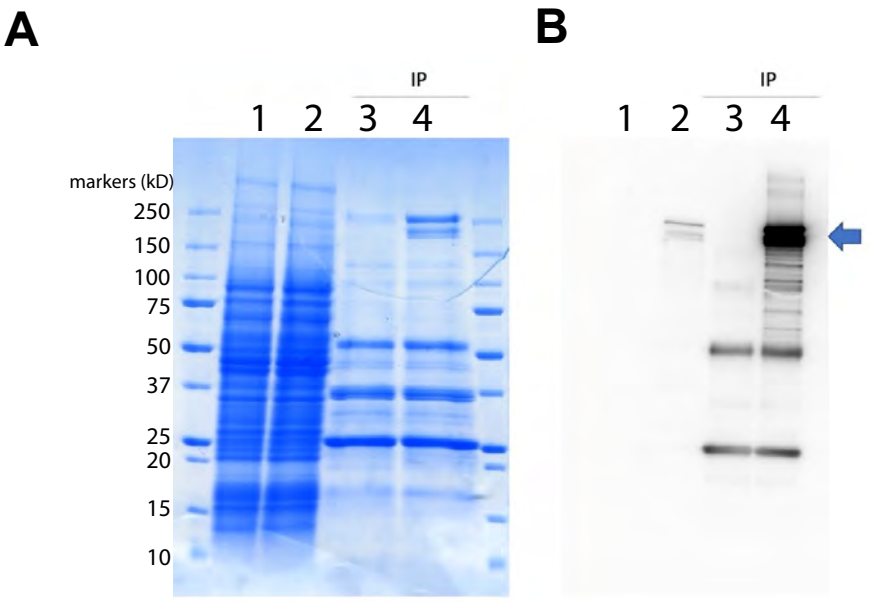

C

Protein ID	Enrichment	Intensity	Sequence coverage	Product Description
high confidence				
TTHERM_00758980	∞	6.7E+11	82%	Dop1p
TTHERM_00637570	∞	8.1E+10	100%	Bis(5-adenosyl)-triphosphatase, HIT domain
TTHERM_00378790	∞	5.5E+10	38%	scavenger mRNA decapping enzyme carboxy-term-binding protein, N-terminal HIT domain
low confidence				
TTHERM_00637780	∞	2.0E+09	2%	transmembrane protein, putative ion channel

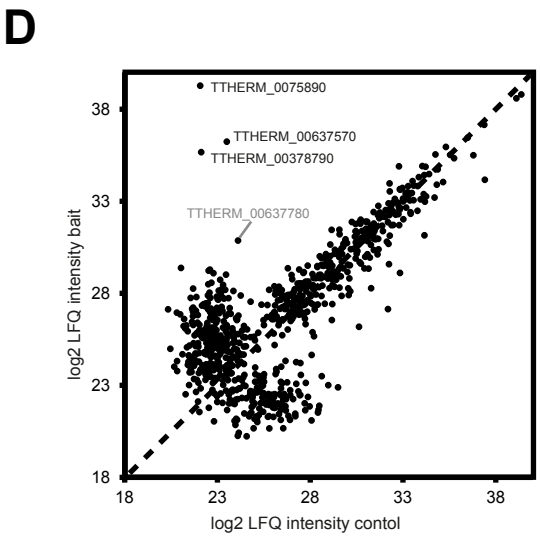

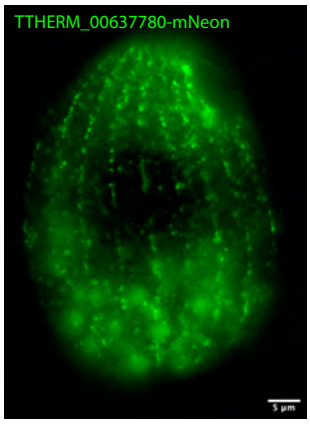

Fig. S4. Immunoprecipitation of Dop1p-interacting proteins and identification of candidate Dop1p-interacting proteins.

A: A Coomassie blue-stained SDS-PAGE gel of the total cellular and anti-FLAG immunoprecipitated proteins from WT cells and Dop1p-FLAG-expressing cells. Lane 1 and 3: WT cells; lane 2 and 4: Dop1p-FLAG-expressing c Lanes 1 and 2: SDS whole cell extracts; Lane 3 and 4: pulldown eluates from anti-FLAG beads. IP=immunoprecipitates. Protein cryopowders were prepared from WT cells and Dop1p-FLAG-expressing cells in 20 mM HEPES PH7.4, 250 mM NaCitrate. The pulldown eluate is enriched in bands near the 250 kDa marker (Dop1p~256 kDa with FLAG ~1kDa).

B: Western blotting of anti-FLAG pulldown. Samples identical to those in the SDS-PAGE gel from Panel A, with the equivalent lane loading, were used for Western blotting using the anti-FLAG antibody. The arrow indicates species in the expected weight range for Dop1p-FLAG.

C: Table shows the top four most enriched proteins (including the Dop1p bait as the first one) identified by LC-MS/MS.

D: Multi scatter plot of the imputed logarithmic LFQ-intensity correlation comparing proteins detected in the FLAG-tagged Dop1p pulldown and the respective WT control. Protein cryopowders were prepared from WT and Dop1p-FLAG- expressing cells and suspended for incubation with anti-FLAG beads, as described in Materials and Methods. Bound proteins were eluted with 2X SDS sample buffer, electrophoresed a short distance into SDS-PAGE gels, and subjected to tryptic digests and LC-MS/MS analysis.

E: Live cell imaging of tran TTHERM_00637780, identified in the Dop1p pulldown. TTHERM_00637780 was tagged with mNeon at the endogenous locus. The semi-regular array of cortical puncta exhibited by known Golgi markers in these cells; in addition, other mobile puncta are visible deeper in the cytoplasm. Immobilized cells were imaged using a Zeiss Axio Observer 7 system. This image shows one frame from a time-lapse video (Movie 17).

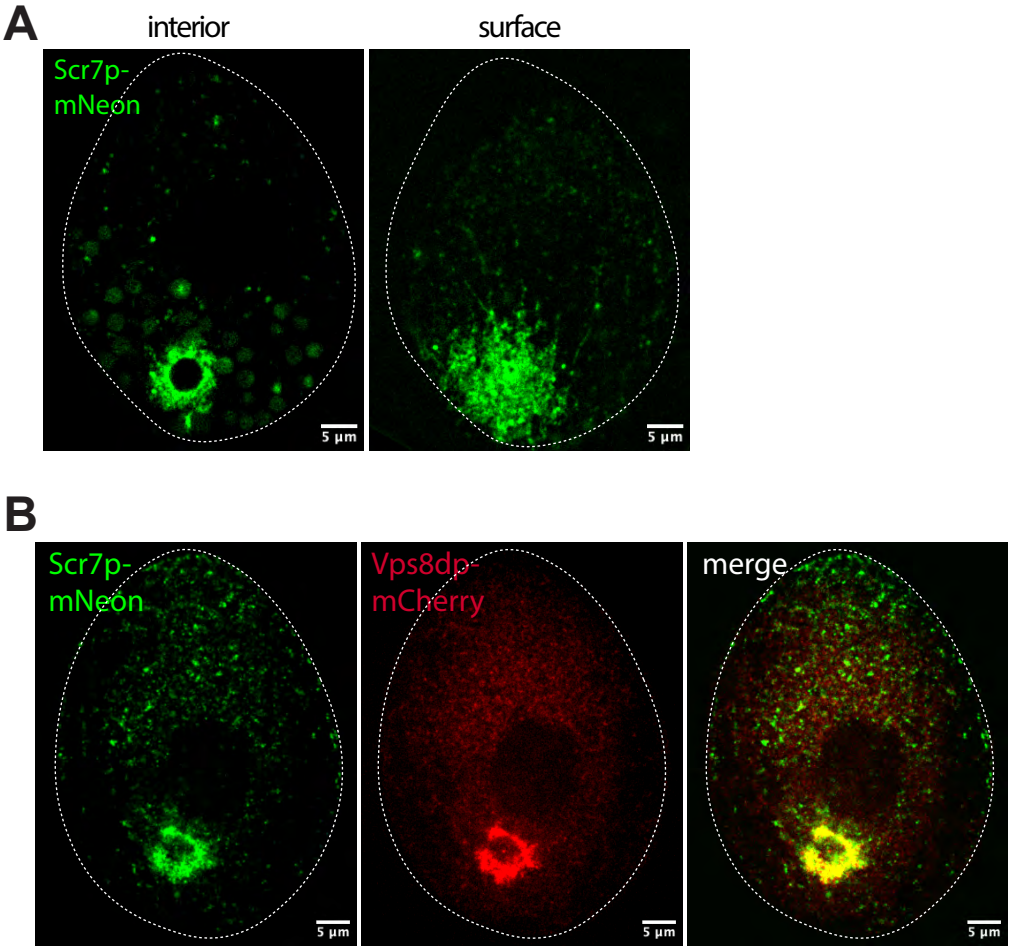

Fig. S5. Live and fixed cell imaging of Scr7p (Scramblase 7).

A: SCR7 (TTHERM_00999060) was tagged with mNeon at the endogenous locus. Live images show that Scr7p localizes to the CV bladder (left panel) and the reticulum (right panel), in addition to dispersed puncta at the cortex and in the cytoplasm, particularly at the cell anterior, a localization shared by *T. thermophila* Scr1p (Chen et al., 2014). Images were taken with a Marianas spinning disc confocal microscope. These images show the selected frames from a time-lapse video (Movie 19)

B: Cells co-expressing Scr7p-mNeon and Vps8Dp-mCherry were fixed and imaged with a Marianas spinning disc confocal microscope. Shown are the separate channels and the merge, in which Scr7p and Vps8Dp tightly co-localize.

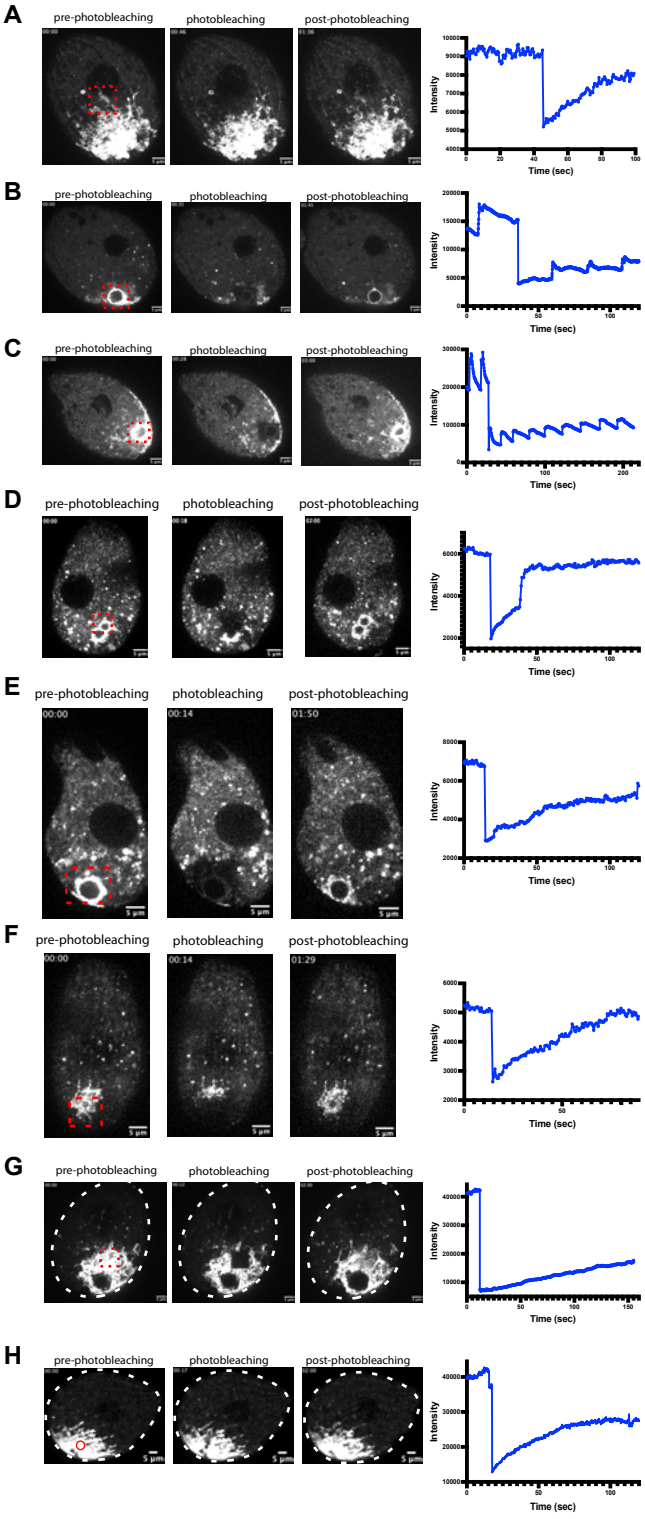

Fig. S6. FRAP analysis.

A-C: FRAP analysis of cells expressing Dop1p-mNeon. For each of three cells, the images show the cells before and after the photobleaching event, whose target in each cell is indicated with a dotted red line. The fluorescence intensities in the photobleached areas are shown in the right-hand chart. A: photobleaching focused on an area within the CV reticulum. B and C: photobleaching focused on the CV bladder. Live Imaging was using a Marianas spinning disc confocal microscope.

D-F: FRAP analysis of cells expressing Vps8Dp-mNeon. For each of three cells, the images show the cells before and after the photobleaching event, whose target in each cell is indicated with a dotted red line. The fluorescence intensities in the photobleached areas are shown in the right-hand chart. D: photobleaching of a part of the CV bladder. E: photobleaching of the whole CV bladder. F: photobleaching of the CVC in a focal plane where the reticulum is in focus. Live Imaging was using a Marianas spinning disc confocal microscope.

G and H: FRAP analysis of cells expressing Vma4p-mNeon. The images show the cells before and after the photobleaching event, whose target in each cell is indicated with a dotted red line. The fluorescence intensities in the photobleached areas are shown in the accompanying charts. Live imaging was using a Marianas spinning disc confocal microscope.

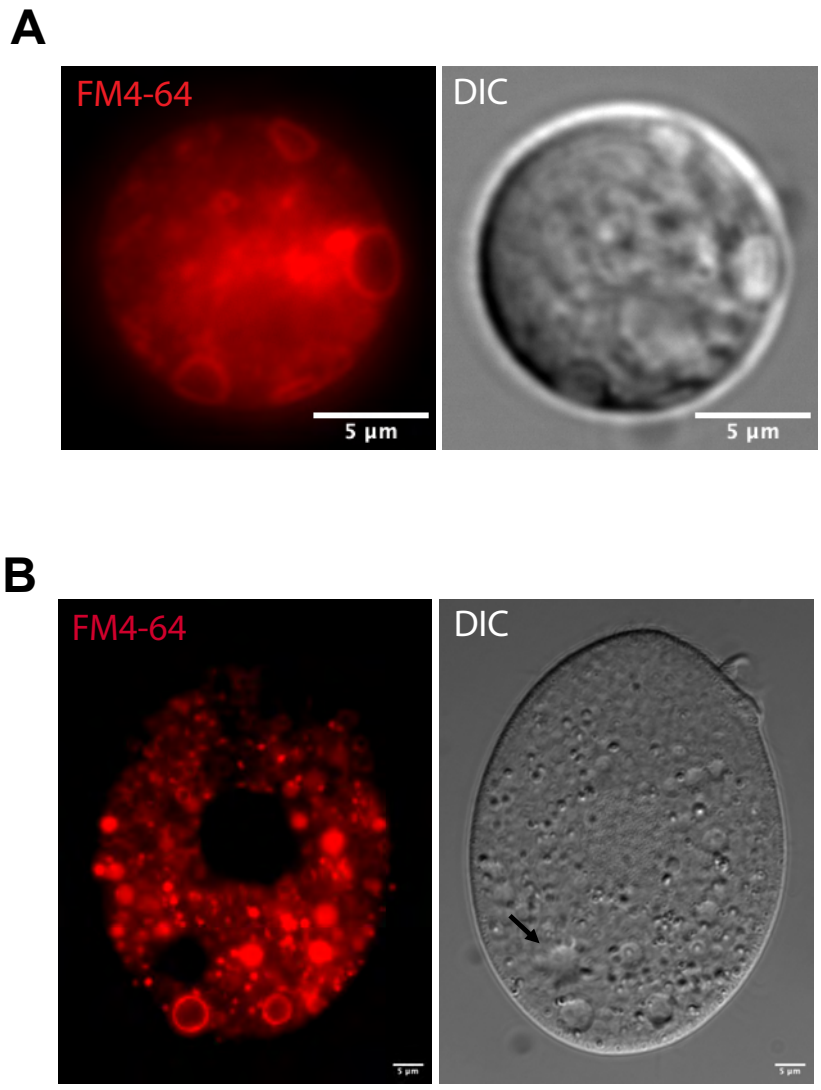

Fig. S7. A: Live imaging of Dictyostelium cell with FM4-64. Vegetative growing cells were stained with FM4-64 for 5 minutes. Images were taken with a Zeiss Axio Observer 7. B: Intracellular labelling of Tetrahymena cell following long-term incubation with FM4-64. Cells were incubated overnight with FM4-64, and imaged with a Zeiss Axio Observer 7 system. Left panel: FM4-64 labels a wide range of intracellular structures but not the CV, whose position is indicated in the right-hand panel DIC image. The CV could be identified unambiguously based on its characteristic contractile activity, as can be seen in the time-lapse video from which these images were taken (Movie 18A and 18B).

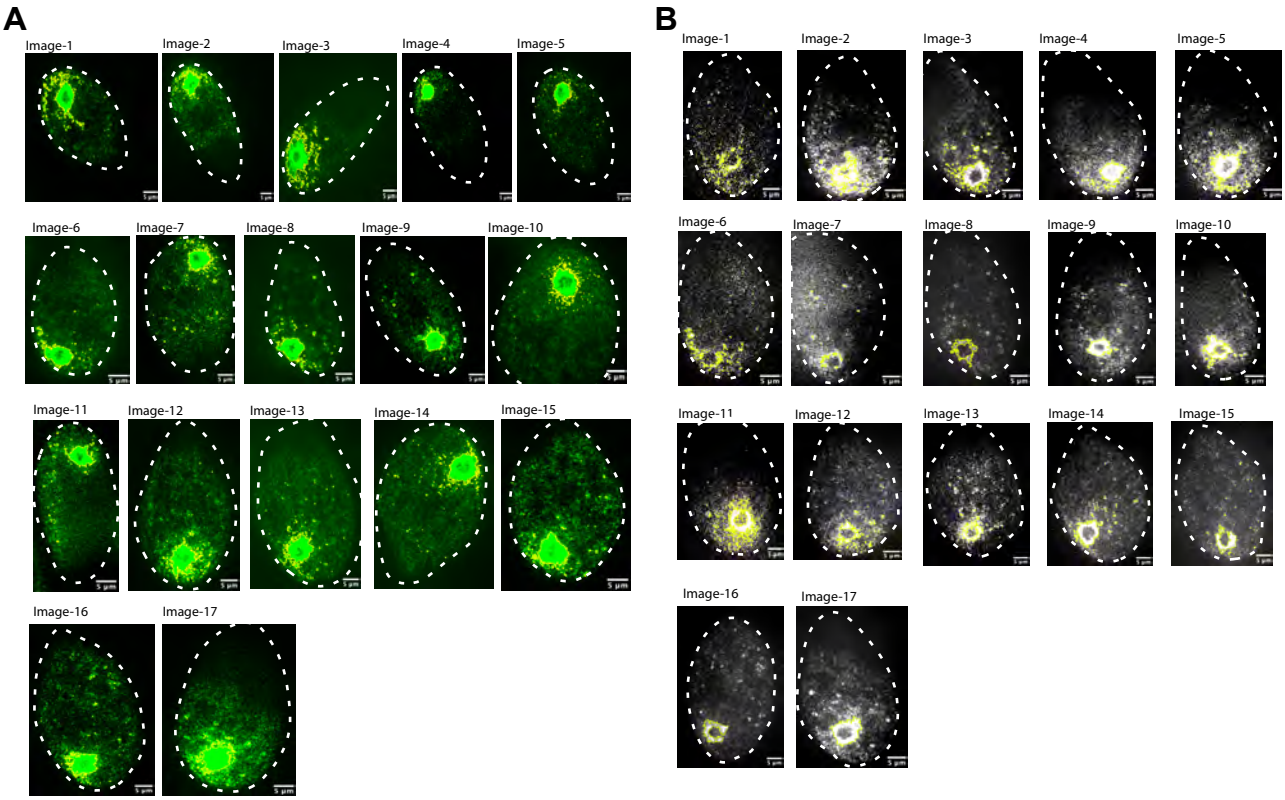

Fig. S8. A: Images used to quantify Dop1p in the CV versus cytosol. The 17 images shown were analyzed by FIJI image process software to measure the signal sum intensity for the whole cell and for the CVC, indicated in yellow. Images were taken with a Marianas spinning disc confocal microscope. B: images used to quantify Vps8Dp in the CV versus cytosol. The 17 images shown were analyzed by FIJI image process software to measure the signal sum intensity for the whole cell and for the CVC, indicated in yellow. Images were taken with a Marianas spinning disc confocal microscope.

CHEN, B. C., LEGANT, W. R., WANG, K., SHAO, L., MILKIE, D. E., DAVIDSON, M. W., JANETOPOULOS, C., WU, X. S., HAMMER, J. A., 3RD, LIU, Z., ENGLISH, B. P., MIMORI-KIYOSUE, Y., ROMERO, D. P., RITTER, A. T., LIPPINCOTT-SCHWARTZ, J., FRITZ-LAYLIN, L., MULLINS, R. D., MITCHELL, D. M., BEMBENEK, J. N., REYMANN, A. C., BOHME, R., GRILL, S. W., WANG, J. T., SEYDOUX, G., TULU, U. S., KIEHART, D. P. & BETZIG, E. 2014. Lattice light-sheet microscopy: imaging molecules to embryos at high spatiotemporal resolution. *Science,* 346**,** 1257998.

Table S1. Cell strains used in this study.

Available for download at
https://journals.biologists.com/jcs/article-lookup/doi/10.1242/jcs.261511#supplementary-data

Table S2. PCR primers used in this study.

Available for download at
https://journals.biologists.com/jcs/article-lookup/doi/10.1242/jcs.261511#supplementary-data

Table S3. Quantification data for Dop1p and Vps8Dp.

Available for download at
https://journals.biologists.com/jcs/article-lookup/doi/10.1242/jcs.261511#supplementary-data

Table S4. Top candidates from mass spectrometry of Dop1p pulldown.

Protein ID	Enrichment	Intensity	Sequence coverage	Product Description	TMHMM	SignalP
high confidence						
TTHERM_00758980	∞	6.7E+11	82%	Dopey	0	0
TTHERM_00637570	∞	8.1E+10	100%	Bis(5-adenosyl)-triphosphatase, HIT domain	0	0
TTHERM_00378790	∞	5.5E+10	38%	scavenger mRNA decapping enzyme carboxy-term-binding protein, N-terminal HIT domain	0	
low confidence						
TTHERM_00637780	∞	1.95E+09	2%	transmembrane protein, putative ion channel	10	0
TTHERM_00194540	∞	6.98E+08	17%	TATA-binding protein interacting (TIP20) protein	0	

>TTHERM_00637570 Bis(5'-adenosyl)-triphosphatase

MINTALKLGSIEIPQQMIFWTKSNICAIIPCVQLVPGHVLIIPKRNVSYFNDLELQEVFD

IGLLTRFLTKGLEKFYTATSSTVYIHNYNPNDSESLQQVYVHIIPRKPADFQNNDDIYKK

LEEYDAEFTKKFKWGFTQANSSLNGVLEIEANECKKYATFLETFQREEAEKS

>TTHERM_00378790 scavenger mRNA decapping enzyme carboxy-term-binding protein

MSASVVANLTVQFGKSQLPLSQIFILRKNVFATTNLKPACPGHVLVASRRPVKRLHELTE

VETLDLWTTVQQVSRVMEQIHKFPCQIGVQDGTDAGQTIDHVHIHIIPFPKEYSQDVIMD

SEGRIKCNLNEENQIQKYYQIQKDLLEQQMIWPKKLTNIELTLNKGQTSSIDQIQIDQSI

QLNSFINVNNIFLDDICSYVFRQCNQFILKYYALQKYDSANQYIDKQIDILCLKYMISKI

SIVDKHLHIIFYIKISLKLQQEGQLKVDRLFVCLFD

>TTHERM_00758980 dopey, amine-terminal domain protein

MDKTKQIEKSSQLNKQLNTLLSGFEKNKAWSDIGTWLYKVEQAMKENPSPYISEKLSLAK

RLAQCLNPVLPQAINLQTLKIYELIFENIKIASQGNVEEYKKMFCEDIGIYSVGLFPFFQ

NAHQKNKHQFLEIIRNYYIPVGRDLIPCLPGLVLSILPGLEEQSEILIKDVTKTLEAIMT

SCGRRYFLGSVWMGIKRTQRGREHAIKFLTKLLPKVKYEEDEEENQDASDNSSNFSEDNY

EEFDETKFKEQQKKEQTQTVEQTPVKQNQSPKFQEQQAEQADQVDHDQQNNQVEIQDEEK

IAQDLIQQAQAEAEKHFQSMLEGNEENQDQQEQHQEEQQPQQPVEEQEVEDDQQQKQLNR

QQADEEIQKSLVASLQQQQQLQQQQQQLQQQQQQQQQQQQQQQQQQQQAATSTSTAPVSAAK

SLTDQKLNILESTSEQKKGGKSALEIAFQHEIAPKIAKKQDFTNTFFVRDNLKYIEESIN

ENDDNNNFPNKSSLIINTILSCFEDENQIVRRNILDLMYHHLRINHRILSRDDQLILVEG

VLYLLIRKDVSVTRRVNVWLFGKPDMDNKYTITKSREFVVDLLIDAFKRIFSVEPQDKVA

ALQPIKIMQQFYMEHENLVEITLSKLAISFVKYVYTHTQNMQFSADVLKSGIRFMENIQG

QLNSLLKSISEEAVQLLREKKDDQCLEIINLIEFTYENLLASEDSFDPMQQRDCIKETLS

RLFISLSYLDEKNIQEFHSLEPTLKVIYKLMLKLESAEAKIKAIEKKEKKQLEITNEQKE

IAQYLDECSEKYFNFYGKLSNELENFKSNNIYKLASQSLVKLQKFLFDKKKMTQLPQWFK

CISQSIKITNPNLSLIAIESMIEIMISEKIDPIYEQLKVLIIDEAKLKYSKKNELVAGND

YTKLTLEKLWSLLDFQHFYDRIIDLIIYFSKYFPQYFKEVVVNSFQAVSITEKEASIRRF

AVFWRLTAHHKSKLLLSELNKVGLFIMLDFLDHDNPLIRHASKNWLMESVPQFYRIIDPL

FEVLLQANSSWYVTDSYQVFYTKIYETTRANETFRKLKSILIIASDVFLKYISSYQLSPL

LQDMKSHFTDKNQAVLLRKLGATMSYFSTINPNLNSLDMTSSQSTAVNDKKVTDLKMTYL

DLLIIVCLRYIQGQALESLSLKFQVENAAVNASACEYMELLITHLEDAPLCLALCEYLME

PLLTILGHCITNRDYVMQVQLLNVFRIIFFHSSYIKKNNTEEIKFKLVQTLSNKLFIPNI

LKGLMTSIPYVRSQFISFISACIPLLSTYLASNQLTSIIKSIMFTYFSLIKHLATTPAQD

NDESMVTISKTQIIKQPSLIKQNKTVILIQTQEVVKEDSNIYEIHTVLEGVRTILQFFLK

IRTLEEIESSKKDQSGGFANLMKTVLTLGLAGSGNANDKDKDGKAFFEKYPDTCKSLLYD

IKQVVELFINSWQTTPEFITEFTSYGIRPYEQKKFNSFNNLLMDMIKNAENDKQRVKILI

ISIIKPLVYEFPNDMMNSFLLLWNRSCMTDPPNAHKDFNQNEFLKKMIEMITILNIPNEL

FLESFYQSFISEIIQKFYQQKNTKEKKNVYFLNYEIAQHESKLLYFLYIYLSYTYIDSNI

LKKENLLLFWNIILKILKIFQPSKNPNTVMWMLDLLYMLSEKYSPKEILSDSKFKKELHD

LINEKLSYLSGWIANVYQVKFNEPSAQTQQSLNNAVDQHMKEMIVQSLQQYRIISPYSPT

FYEISLSFYSQIHILEHAPKSIANQMKELQMNQLDQFIFDRIDTVDENAVYDKYRLICLE

TLKTLSLELLQNTYSPERQDRVVVRVKEFVDPLYAVIENKGSTNSYFLESTSELICSLIE

KAPSLLIKDFRKSILEMFNKDNFFSCNKGTLRYWGKIIDYVLTQDKSNDLFNEYLEKVSL

SAGFFAREQNENKKKIKAFKRTCFIIFSGAKDKYANRLRKLLDSIAEVIKTTDSSQSSLL

ILILFCIRILILRLSQSNLNELFRQIWPILLTLLIQIYSKPLPGQPPRNPNLMLAGLKLI

EILSVAQLDEFFLHQWMFIFDYFGLKLQPLSQQERENQIRLRGQMNEAQLRQYAKISPFY

FQPFVSTCLNEQDLGVKYVNQPIDESEQSEQITYQKKQRKLIMTQCKVDDENELKSHALS

LCQYLISNNENRTEIDFNSIEALIEDDFINLDEHILKV

>TTHERM_00637780 transmembrane protein, putative

MSQQKVIAQQMSLRKQVMAKSKTLFQAEKAILDQEKVSDQLASWEEAVAYRNKFSVMKNN
GGSYEEYSLNCDLSELAQYGPGLRLFFELLKYSAIVFLLMSLISIPALIGNIQGQSLNSI
EMSTNSLPKLSISNQPKLKLLSPGANASDADYQADQVENQQRIVDFVSNSDSRLIQVAVP
DIVYSVIFLLFIFWFHYHSHQIAKETDLKNSLPSNYSIEVSGFPHTITDEKILSNHFRDN
FSVDVFECKFARNYYNTLFLHKEEAQLIDLIKQEKSRQQFLGKDEKKSETLQKLGKKLAD
IQADINQQVQTKMNGSVLSHNEYPSVKAFIILNSIEDKQKIQQEYKKTKGFFGQKRVKEF
MLQNKHLLKLNFKPDEPSNILWENLEVSSFNRFLRTLAVIILVIIVMIITFAVIIIANIA
TPQNTEDCPKQSISFSQASKSSLYTQCYCTNVSFSQMTSNSALQNLCWDVWVKYATTYAL
TIVTGLVVLIVNFLLRLTIQALGKFNRYKTITKYTTSMTSKLFLAFFVNTALITLFLQAN
IYGFVPAITFSKPIPPISNLQDNNKSQFSTDFDRSWYLQVGSKITVTVFFFVVTLFLFQF
LYSMISKCRRESKVKQLEGKDVQRVANKTILGPEFPISFYYASTFNIIFTTLFYSSGIPI
MLFAGFIILTSQYWVYKYLLLRVCRRPPTYDTGLSNRMLLILPWSLLLHLAVGLYMYGQP
LIFPSSQSQLVLNMNQTTGEVKVKINDSAPIENRAFHILYLFIFLLIVLGLYILNISYSG
FLQRFVNMCCKRSHQVVPQHQLVPYNEEYFNIEKRMLPSYNIKVNQDYRYIIEAIDLEKK
FDSENSPRANSSSPQYKETDSINKNIDSIIENI

>TTHERM_00194540 TATA-binding protein interacting (TIP20) protein

MQSAQQQQQQLLDQKRFDELVQDAKDFDPDKKFMAANDLSNALSNGQLKDTDYDTVVKIL

LNQLNDDSNEVQGNSIRCLSKIINKLQETQVENVSKTMIVKVIEDKGEYRDVYATCLKTL

INGVPSNYAKAVQPILLHAIQGMEQKLNNKEFDVQEELCDILNNLFKKWGQSLSTTNANV

KNLTNILMSNISKGERNSLKKKSCSCLGSLGLILHKDDIGRVVKELLQNIKKPDNQKQIQ

QHLREKQIYVVYALSAISKTVAKKLGSNLKDLINIILKDINQYVEEVDDYDLIITISEMF

ESYLSILESLIKGCPDEIKEYFPQIVDLSSQLINYDPNGQARISNGGEMEIEDGGEEDEY

DYLSDDQDGDDSSWRVRRAALNIIETLVKSDSEMIRPIFEKCVSSQSEQSTIVYRLGERN

ENIRFATFSCLQTIIRAIVISDVSHDKGDDDFDQELNSGPQLVRVKSAVKEFNISEIISE

IFNTLTFILEKEKKVTQAILTGAYKLIESISRNLSRQVVSDPSIWRLAFDLIKRTIENKA

SPNELKVTAFSSLRKLLKNYHESSEIAHLQNDIPNIFKLASVGLVQDYFKIVAESFRCLN

SLFNMINKQFNSAIPTFSASIQQIFPQISVKLNSSDIDQEIKQSVLSCTTSLLVSLPQTI

QAQQIKDIINAISEKIKSETKKIPVLKLLKKIPLSVHPHITADSIKLLNSSAESICDLLA

KQDRSLRVASLEALDKTLVLLSEKKSPLSAKARDNFIALAYDFLNDKDTWVAQLYLSVLK

KSIENAPQSPQYYTKIIESITKFSNSSIVSSAHFSSLYEVFATLSKLNLSNRSQMIQNLI

ATGSKDSINSVSRAISSIIIELPAGEQQTFINQIFSTASSDKEVVLKRQICLVTLGEIGR

HVNLCSGNILQEVQKILNNKQNNEEIRTAASISLGGIAIGNLNMVLPQVIQTINSGSEGQ

YLMLNSLKQIIEHSQQLSQSIIQIIPNLFKATENGDESLCNIISYIIGKVTHLNLKEMKP

LILQNLSSKNQNTKYTTASSFKYFCLKTLKIDNDLRELVYALMNNINEKDIRTRTAILKS

LNMISYNLPNAIIQHINKNEFFLPVREALRFTQIREIDFGPFKQKNDDGEPVRNAAFTLL

DTAIDHLHYRGVENFEREILEEVLYEFANESSEDIKILRFQICTKFAHKVPLKVTPFLDQ

ISEVFLNVLKPYASKADGDRAADMVRTGLICCLTLKSIAEDESNTKYLNFWELVMKTEKY

RNIINSMTN

Table S5. Mass spectrometry data-2.

Available for download at
https://journals.biologists.com/jcs/article-lookup/doi/10.1242/jcs.261511#supplementary-data

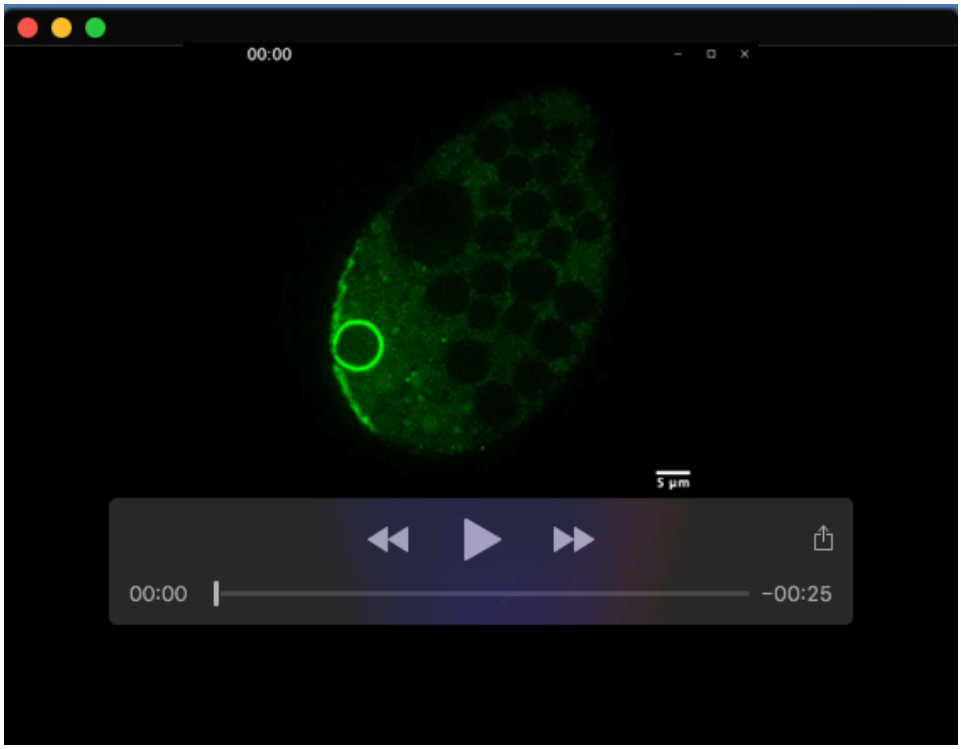

Movie 1. Live cell expressing Dop1p-mNeon with cross-sectional view of the CV. Linked with Figure 1C. Live imaging with a Marianas spinning disc confocal microscope.

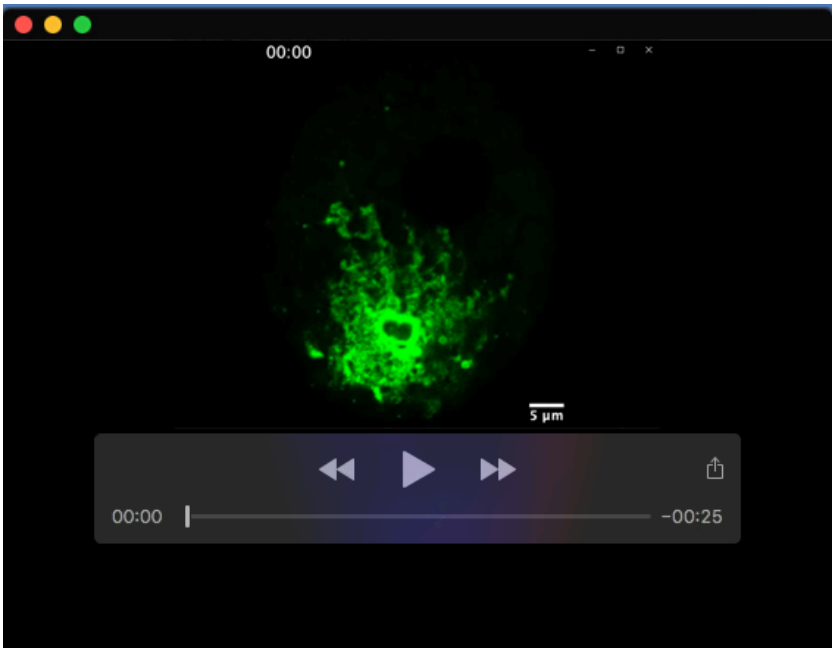

Movie 2. Live cell expressing Dop1p-mNeon, with focal plane near the top surface of the cell. Linked with Figure 1D. Live imaging with a Marianas spinning disc confocal microscope.

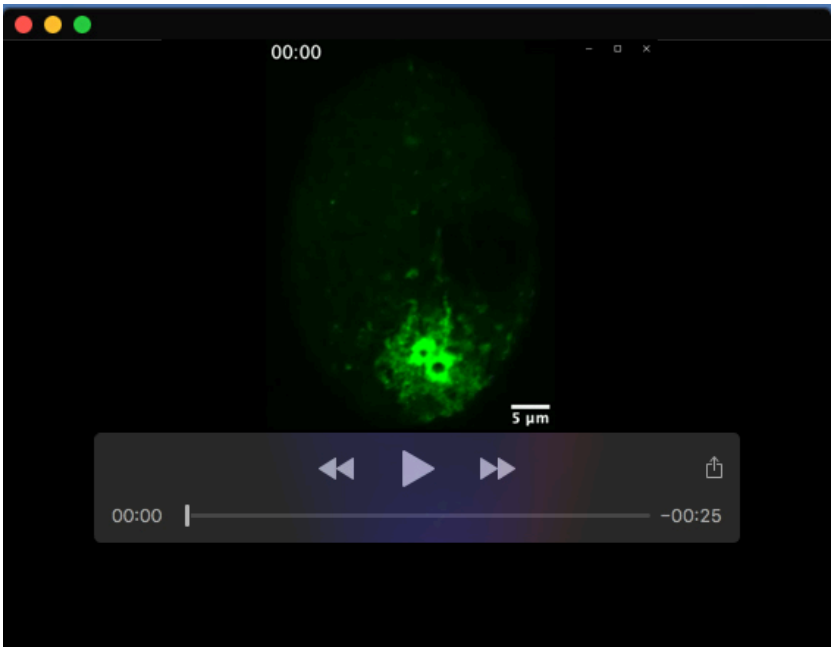

Movie 3. Live cell expressing Dop1p-mNeon, at focal plane very near the plasma membrane. Linked with Figure 1E. Live imaging with a Marianas spinning disc confocal microscope.

Journal of Cell Science • Supplementary information

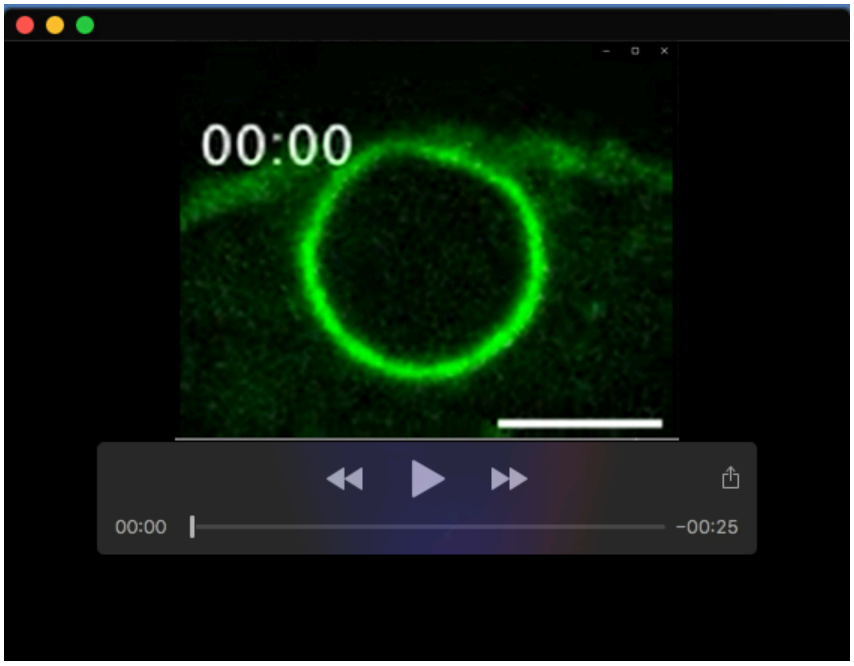

Movie 4. Live cell expressing Dop1p-mNeon, at focal plane corresponding to the CV cross-section. Linked with Figure 2A. Live imaging with a Marianas spinning disc confocal microscope.

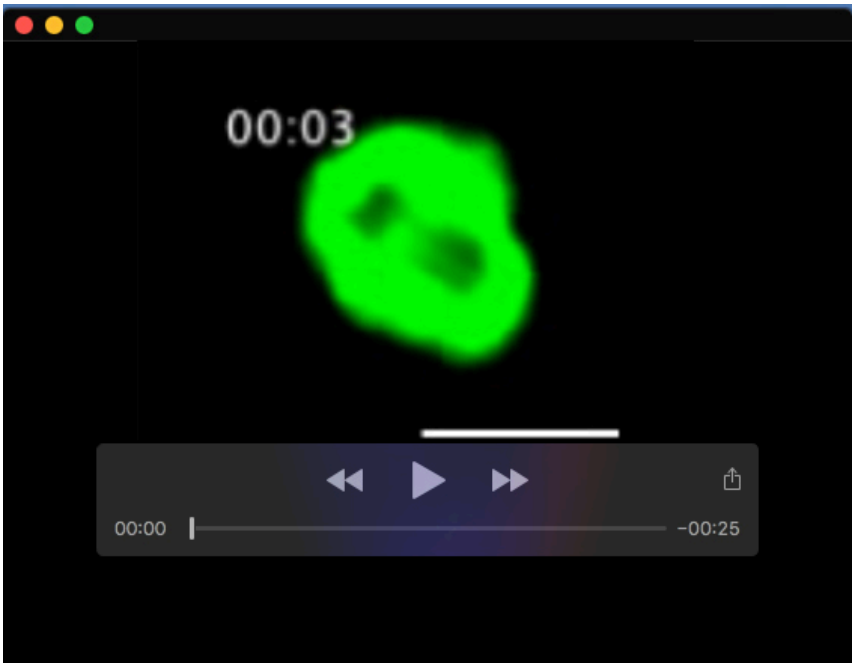

Movie 5. Live cell expressing Dop1p-mNeon, at focal plane tangential to the CV. Linked with Figure 2B. Live imaging with a Zeiss Axio Observer 7 system.

Movie 6A. Live cell expressing Vps8Dp-mNeon, in the DIC channel. Linked with Figure 4A. Live imaging with a Zeiss Axio Observer 7 system.

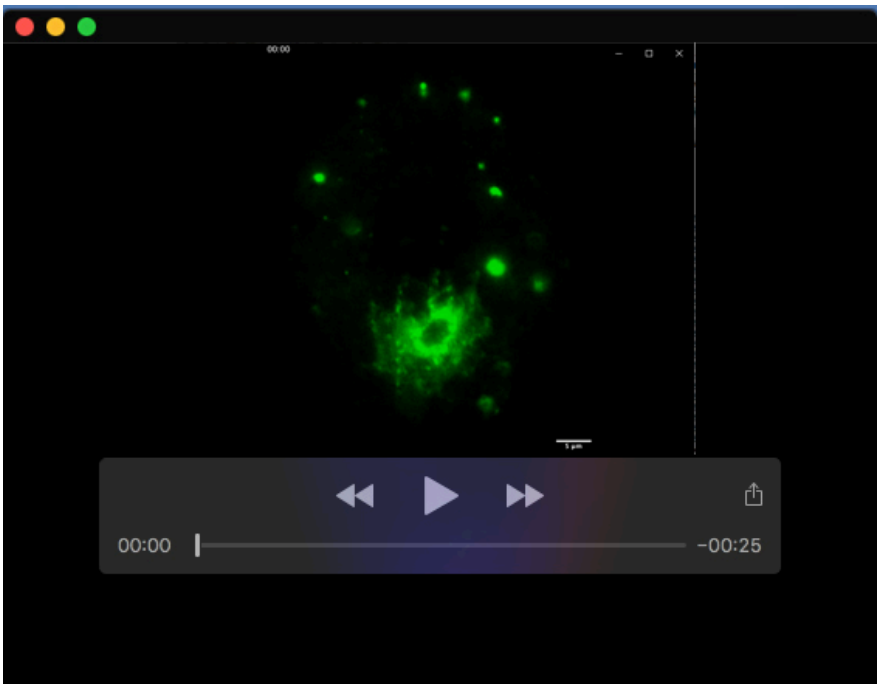

Movie 6B. Live cell expressing Vps8Dp-mNeon, in the fluorescence channel. Linked with Figure 4B. Live imaging with a Zeiss Axio Observer 7 system.

Journal of Cell Science • Supplementary information

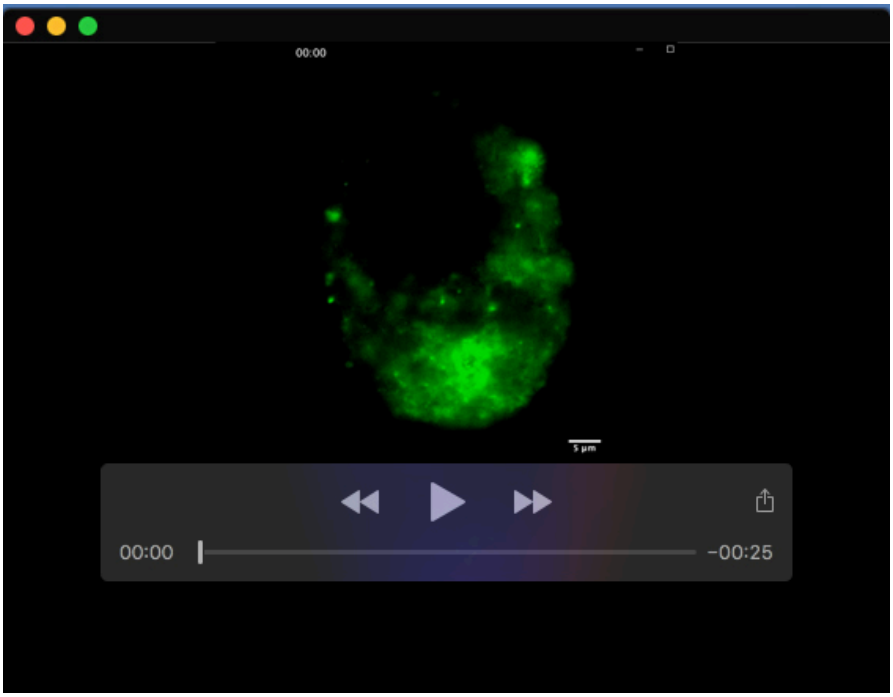

Movie 7. Live cell expressing Vps8Dp-mNeon, showing Z-sections from the cell surface to the interior. Live imaging with a Zeiss Axio Observer 7 system.

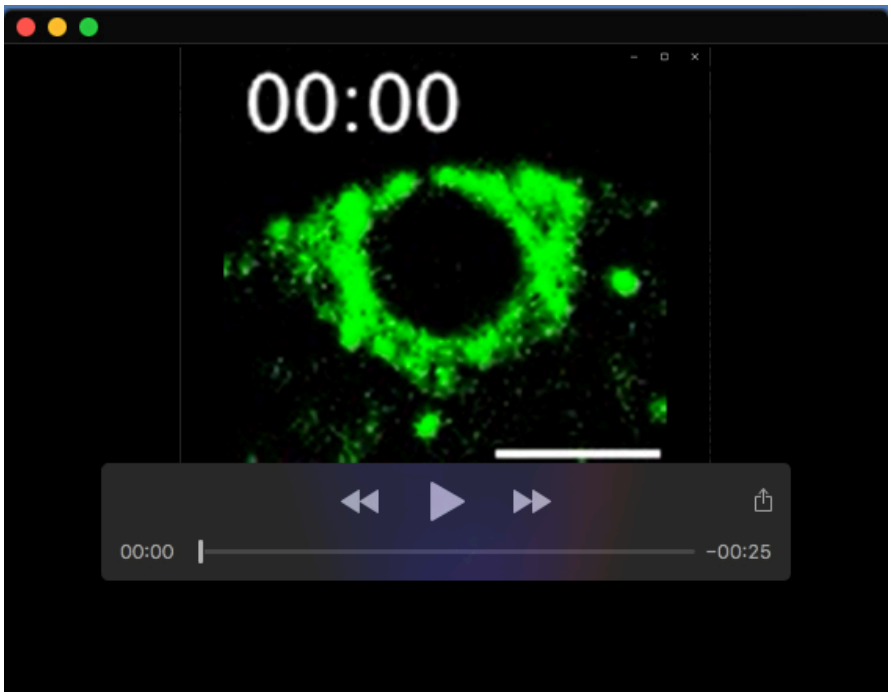

Movie 8. Live cell expressing Vps8Dp-mNeon, at focal plane corresponding to the CV cross-section. Linked with Figure 4C. Live imaging with a Marianas spinning disc confocal microscope.

Journal of Cell Science • Supplementary information

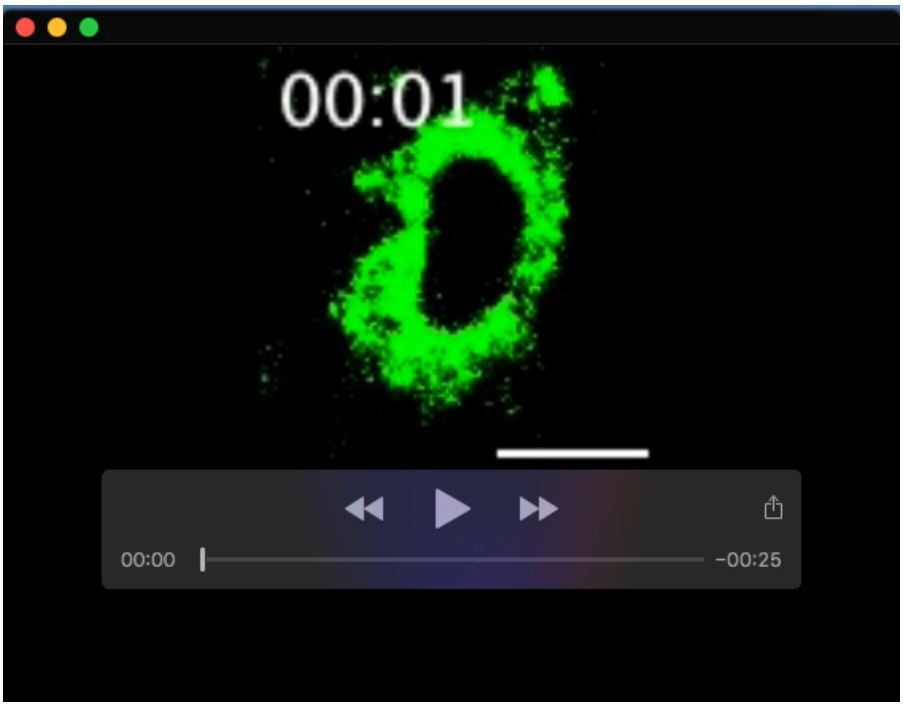

Movie 9. Live cell expressing Vps8Dp-mNeon, at focal plane tangential to the CV. Linked with Figure 4D. Live imaging with a Marianas spinning disc confocal microscope.

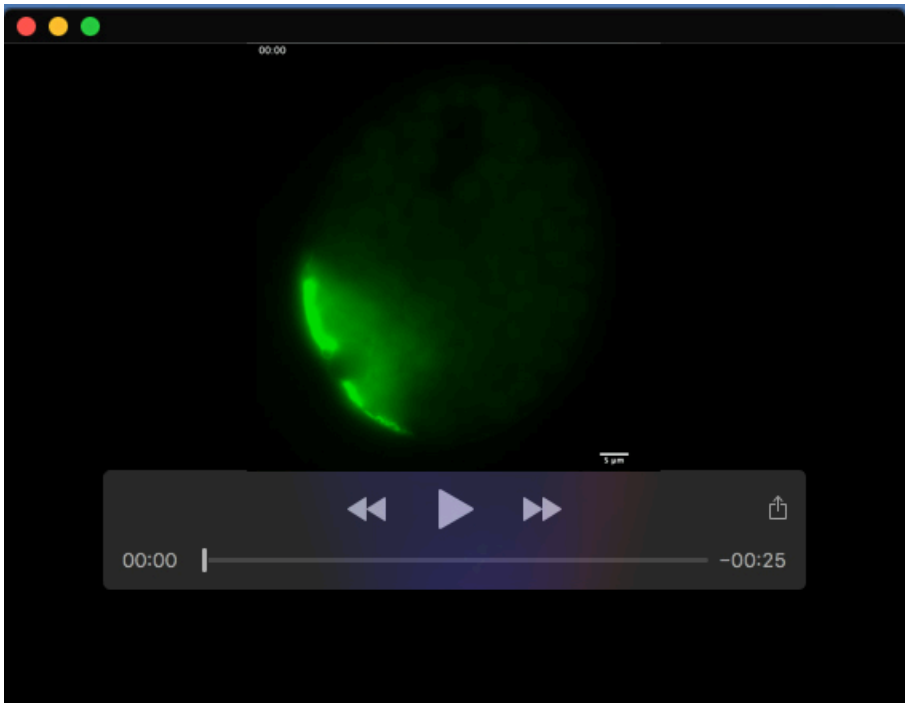

Movie 10. Live cell expressing Vma4p-mNeon in the side view of the CVC near the plasma membrane and proceeding with different Z-stacks between cell interior and cell surface. Linked with Figure 5C. Live imaging with a Zeiss Axio Observer 7 system.

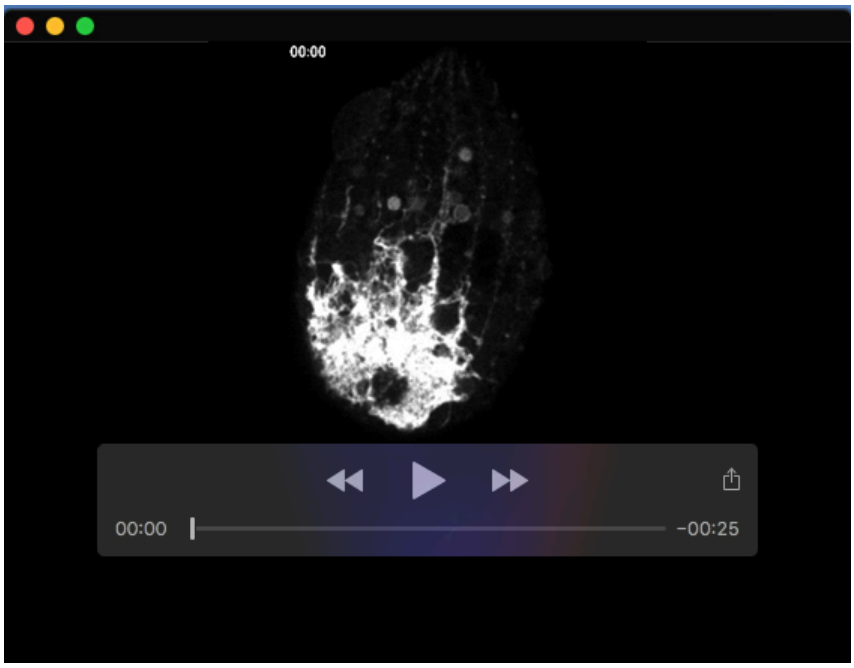

Movie 11. Live cell expressing Vma4p-mNeon, at focal plane tangential to the CV. Linked with Figure 5D. Live imaging with a Marianas spinning disc confocal microscope.

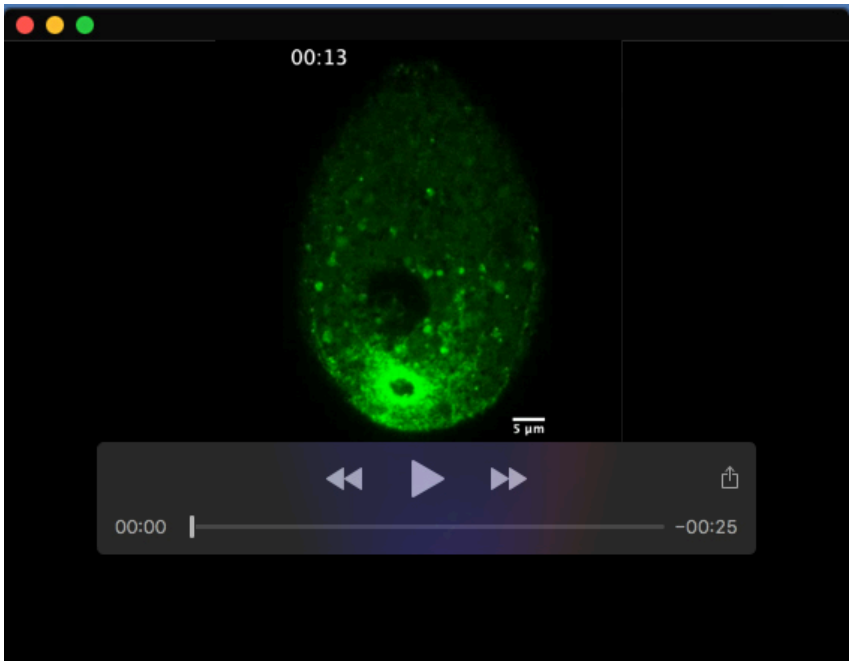

Movie 12. FRAP analysis of cell expressing Dop1p-mNeon. Linked with Figure 8A. Live imaging with a Marianas spinning disc confocal microscope.

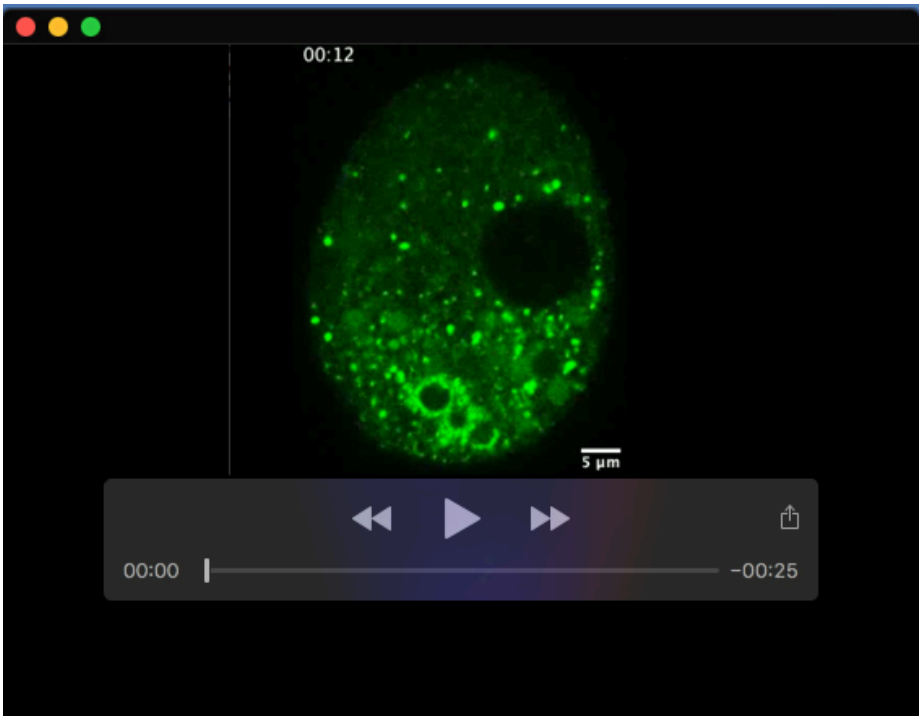

Movie 13. FRAP analysis of cell expressing Vps8Dp-mNeon. Linked with Figure 8D. Live imaging with a Marianas spinning disc confocal microscope.

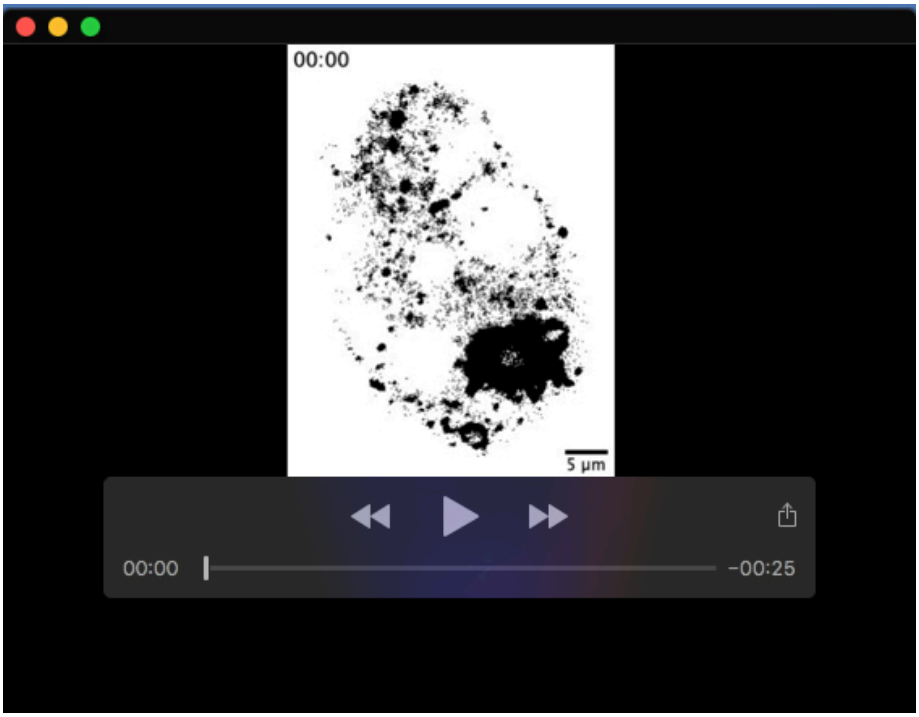

Movie 14. FLIP analysis of cell expressing Vps8Dp-mNeon. Linked with Figure 8G. Live imaging with a Marianas spinning disc confocal microscope.

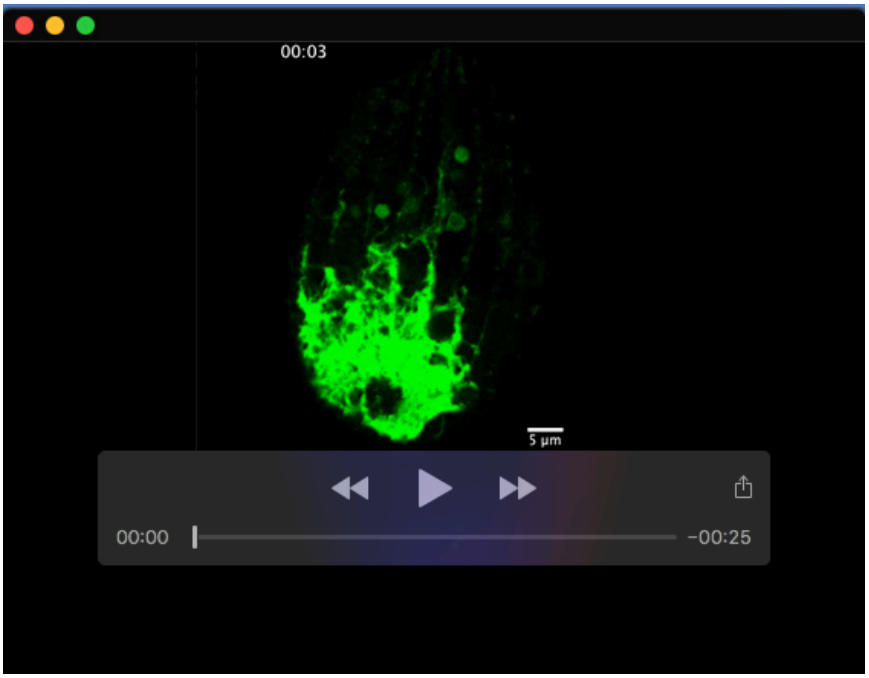

Movie 15. FRAP analysis of cell expressing Vma4p-mNeon. Linked with Figures 9A and 9C. Live imaging with a Marianas spinning disc confocal microscope.

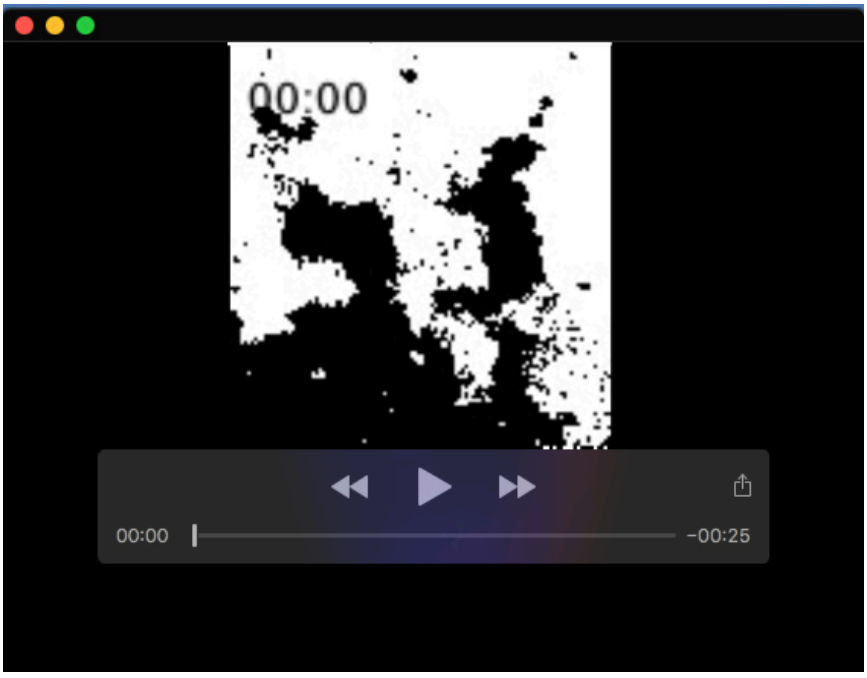

Movie 16. FRAP analysis of cell expressing Dop1p-mNeon, focusing on CVC reticulum. Linked with Figure 9D. Live imaging with a Marianas spinning disc confocal microscope.

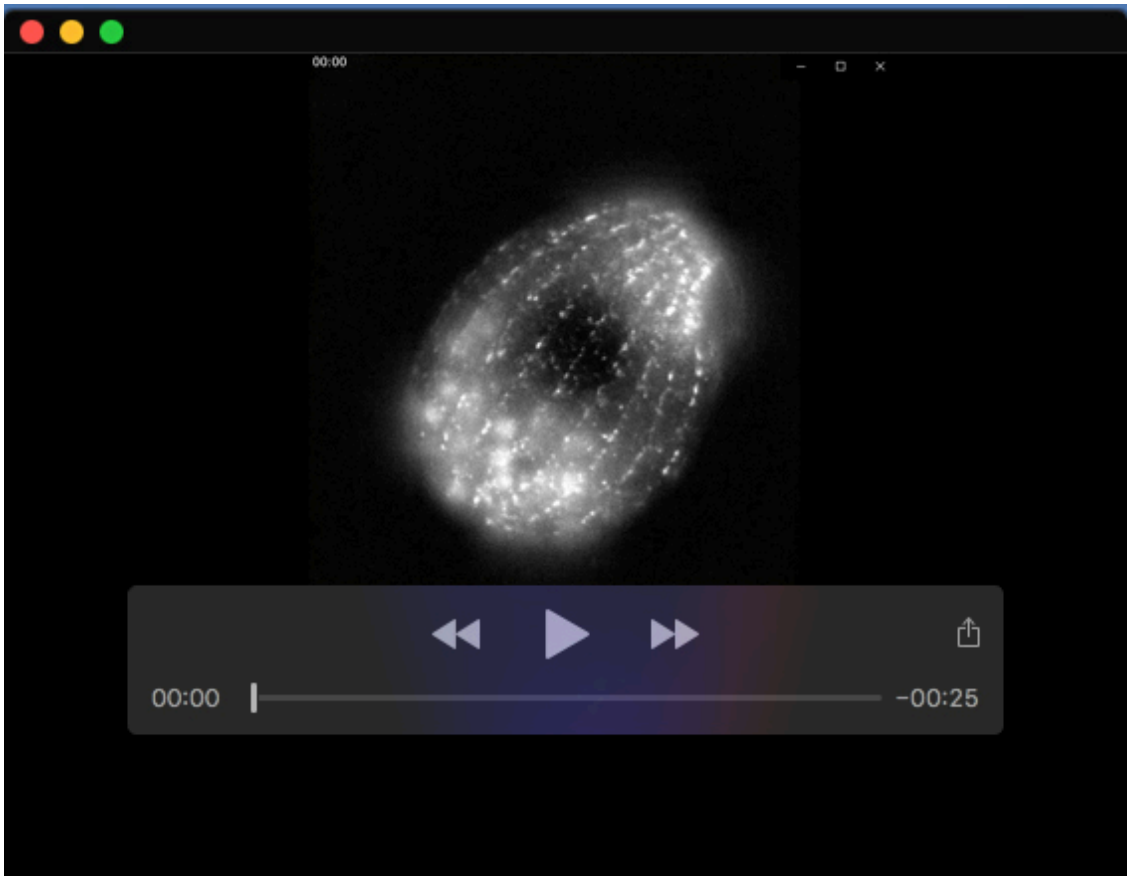

Movie 17. Live cell expressing TTHERM_00637780-mNeon. Linked with Figure S3. Live imaging with a Zeiss Axio Observer 7 system.

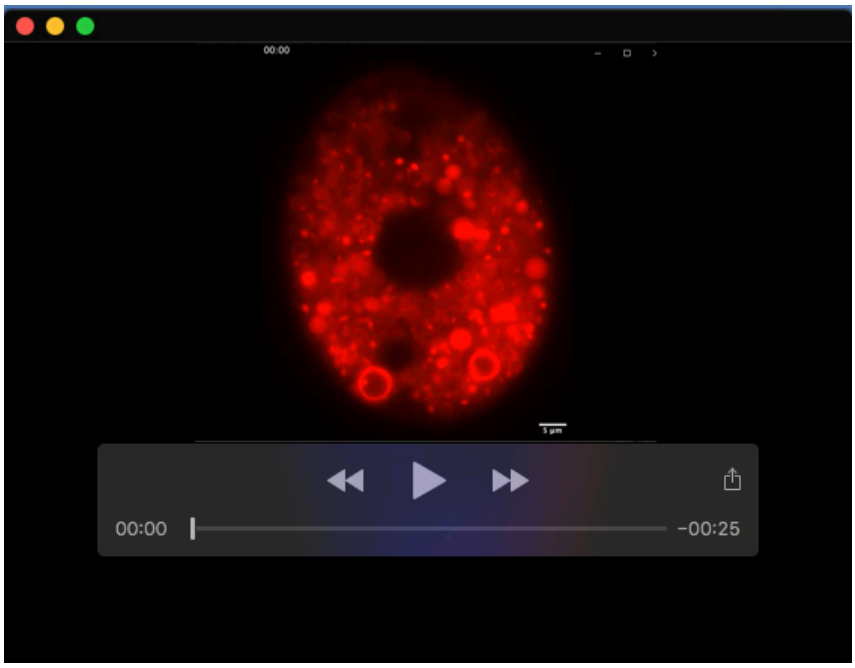

Movie 18A. Cell incubated overnight with FM4-64, viewed in the red fluorescence channel. Live imaging with a Zeiss Axio Observer 7 system.

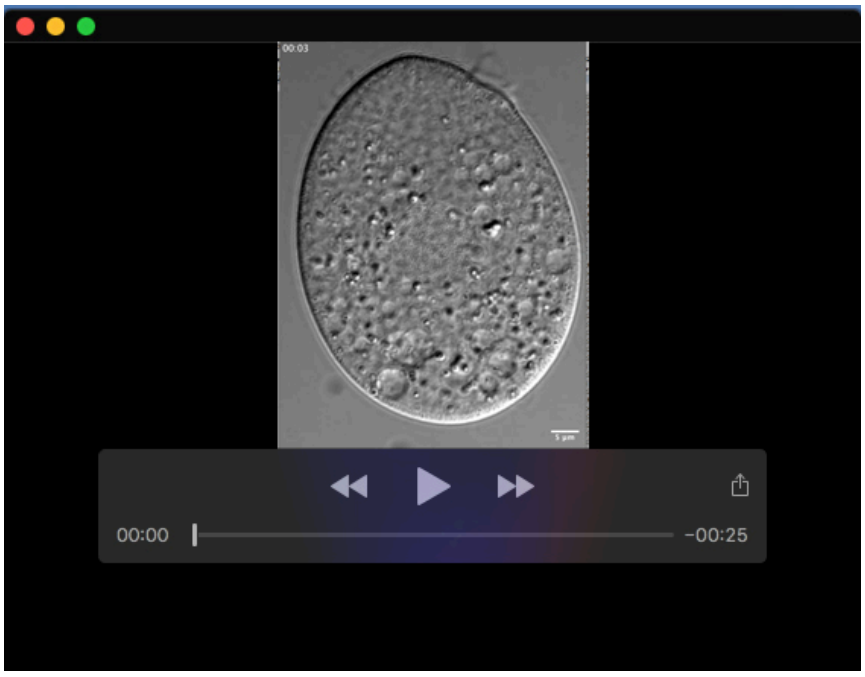

Movie 18B. Cell from Movie 18A, viewed in the DIC channel. Live imaging with a Zeiss Axio Observer 7 system.

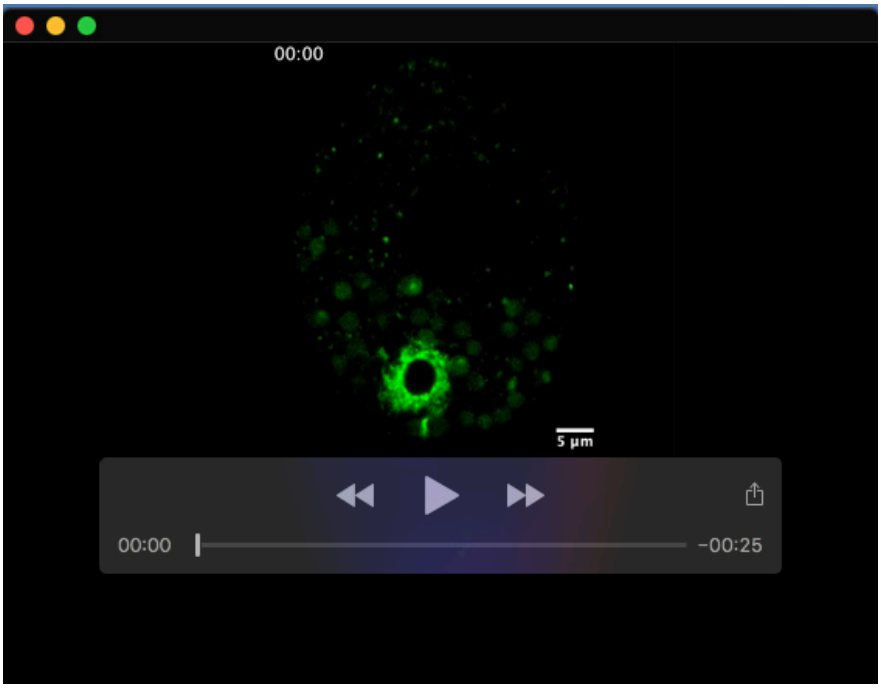

Movie 19. Live cell expressing Scr7p-mNeon. Linked with Figure S4. Live imaging with a Marianas spinning disc confocal microscope.

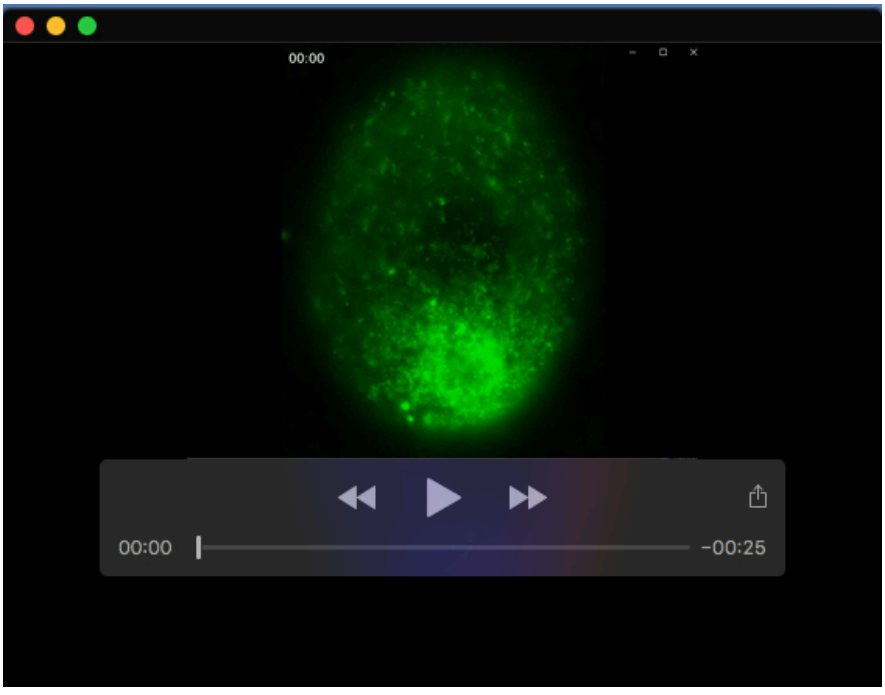

Movie 20. Cells expressing Scr7p-mNeon. Live imaging with a Zeiss Axio Observer 7 system.